九州大学学術情報リポジトリ
Kyushu University Institutional Repository

Shock-Shock Interaction and Associated Particle Acceleration in a Collisionless Space Plasma

中野谷, 賢

https://hdl.handle.net/2324/1959157

出版情報：Kyushu University, 2018, 博士（理学）, 課程博士
バージョン：
権利関係：

KYUSHU UNIVERSITY

SHOCK-SHOCK INTERACTION AND ASSOCIATED PARTICLE ACCELERATION IN A COLLISIONLESS SPACE PLASMA

A Dissertation
Presented to
the Department of Earth System Science and Technology

By

Masaru NAKANOTANI

In Partial Fulfillment
of the Requirements for the Degree
Doctor of Philosophy in the
School of Kyushu University

The department of Earth System Science and Technology
Interdisciplinary Graduate School of Engineering Sciences
Kyushu University
Fukuoka, Japan

September 2018

Copyright © Masaru NAKANOTANI 2018

SHOCK-SHOCK INTERACTION AND ASSOCIATED PARTICLE ACCELERATION IN A COLLISIONLESS SPACE PLASMA

Approved by:

Dr. One, Advisor
Depertment of Earth System Science and Technology
Kyushu University

Dr. Two
Depertment of Earth System Science and Technology
Kyushu University

Dr. Three
Depertment of Earth System Science and Technology
Kyushu University

Dr. Four
Department of Advanced Energy Engineering Science
Kyushu University

Date Approved: September 31, 2018

As long as you ask a good question, Nature tells you whatever you want.

Jean-Henri Casimir Fabre

To my family,

ACKNOWLEDGEMENTS

I would firstly like to thank my supervisors Prof. Shuichi Matsukiyo and Prof. Tohru Hada for their guidance, patience, and unwavering support throughout my candidature, without whom this thesis would not be possible. I would also like to thank Prof. Christian X. Mazelle for his support on my research and my life in France while I stayed for one year. That is a great and irreplaceable experience in my life.

I am especially grateful to my family for their support and taking care of me.

TABLE OF CONTENTS

Acknowledgments v

List of Tables ix

List of Figures x

Summary i

Publications i

Chapter 1: General Introduction 1

1.1 A Brief Overview of Space Plasma Physics 1

1.2 Collisionless Shock Waves 4

1.2.1 MHD shocks 5

1.2.2 Shock waves in Vlasov-Maxwell system 8

1.3 Cosmic Rays 10

1.4 Particle Acceleration 12

1.5 Shock-Shock Interaction 15

1.6 Purpose of This Thesis 20

Chapter 2: Test Particle simulation 34

2.1 Introduction 34

2.2 Test Particle Simulation 35
2.3 Theoretical Analysis 38
2.4 Discussion 41
2.5 Summary 43

Chapter 3: 1D full PIC simulation 46
3.1 Methodology 46
3.2 Run A: Perpendicular Shock Waves 47
3.2.1 Single Shock 48
3.2.2 Shock-Shock Interaction 49
3.3 Run B: Quasi-perpendicular Shock Waves 57
3.3.1 Single Shock 57
3.3.2 Shock-Shock Interaction 58
3.4 Run C: Quasi-Parallel Shock Waves 76
3.4.1 Single Shock 76
3.4.2 Shock-shock interaction 77

Chapter 4: In-situ Observation 87
4.1 introduction 87
4.2 Overview of the Event 89
4.3 Electron acceleration 90
4.4 How are electrons accelerated? 90
4.5 Comparison with the simulation results 93

Chapter 5: Conclusions and Outlook 100

Appendix A: Full Particle-in-Cell simulation 105

References 120

Vita 121

LIST OF TABLES

3.1 Simulation parameters 47

LIST OF FIGURES

1.1 A shock configuration. The left (right) side divided by the shock front (black line) is the upstream (downstream) 20

1.2 An example of the Rankine-Hugoniot relation whose parameters are $\beta = 1$ and $\theta_{Bn} = 60°$. 21

1.3 Geometry of an ideally perpendicular supercritical shock wave. Adapted from Balogh and Treumann [2013] 22

1.4 Schematic one-dimensional profile of a quasi-parallel supercritical shock wave. Adapted from Balogh and Treumann [2013]. 23

1.5 Illustration of the DSA originally sketched by M. Scholer. 24

1.6 The energy spectram of CRs corrected by several instruments. 25

1.7 The energy spectram of CRs corrected by several instruments. The energy range is from 10^17 to 10^21. 26

1.8 Top panel: Gamma-ray spectra of IC 443. Bottom panel: Gamma-ray spectra of W44. Both are measured with the *Fermi*-LAT. Adapted from Ackermann et al. [2013]. 27

1.9 Chandra X-ray images of the western shell of SNR RX J1713.7-3946. Adapted from Uchiyama et al. [2007]. 28

1.10 Shock-turbulence interaction: 2D plot of the magnitude of the magnetic fields. Adapted from Giacalone and Jokipii [2007]. 29

1.11 Shock-current sheets interaction: Two-dimensional color-coded representation of the number density of energetic particles whose energy is 10 times larger than the plasma ram energy. Adapted from Giacalone and Burgess [2010]. 30

1.12 Shock-current sheets interaction: 2D full PIC simulation. Adapted from Sironi and Spitkovsky [2011]. 31

1.13 Shock-shock interaction: 1D hybrid simulation. Phase-space plot. Adapted from Cargill et al. [1986]. 32

1.14 Shock-shock interaction: 1D hybrid simulation. The profile of the magnetic field B_z and the potential ϕ. Adapted from Cargill et al. [1986]. 33

2.1 Schematic showing shock positions, regions, and flow speeds. 44

2.2 Large panel: Comparison of density distribution obtained from the test particle simulation for two shocks (thick solid line), theoretical model based on the diffusion convection equation with constant diffusion coefficient (dotted line), and the same model that takes into account the dependence of the diffusion coefficient on the cosmic ray energy (thin solid line). The two blue lines with indices -4 and -2 are indicated for reference. Test particles are injected at both "Shock1" and "Shock2". Small panel: density distribution obtained by the test particle simulation for one single shock. . . 44

2.3 The breaking point p_b as a function of L (crosses) and u_2 (circles), numerically evaluated using the first derivative of $\log n(p)$ with respect to $\log p$. Solid lines are the equation (2.15). 45

3.1 Left panels: electron phase space density of v_x, v_y, and v_z from the top to the bottom. Right panels: ion phase space density of v_x, v_y, and v_z from the top to the bottom. 52

3.2 The plasma density, plasma beta, electric field E_y, E_z, magnetic field B_y, and B_z from the top to the bottom. 52

3.3 The time-space evolution of the magnetic field B_z. 53

3.4 Electron and ion phase space density of v_x and v_y for three times ($t\omega_{pe} = -2175, t\omega_{pe} = 0$ and $t\omega_{pe} = 2175$). 53

3.5 The profile of the magnetic field B_z fro three times ($t\omega_{pe} = -2175, t\omega_{pe} = 0$ and $t\omega_{pe} = 2175$). 53

3.6 The time-space evolution of the magnetic field B_z. 54

3.7 The profile of the plasma and pressure at $t\omega_{pe} = 2175$. 54

3.8 Top panels: ion energy spectrum for three times ($t\omega_{pe} = -2175, t\omega_{pe} = 0$ and $t\omega_{pe} = 2175$). Bottom panels: electron energy spectrum for three times ($t\omega_{pe} = -2175, t\omega_{pe} = 0$ and $t\omega_{pe} = 2175$). 55

3.9 Left panel: An ion trajectory on the time-space evolution of the magnetic field B_z. Right panel: Time evolution of the ion energy. 55

3.10 Schematic view of the ion acceleration. 56

3.11 Left panel: An electron trajectory on the time-space evolution of the magnetic field B_z. Right panel: Time evolution of the ion energy and B_z experienced 56

3.12 Left panels: electron phase space density of v_x, v_y, and v_z from the top to the bottom. Right panels: ion phase space density of v_x, v_y, and v_z from the top to the bottom. 67

3.13 The plasma density, plasma beta, electric field E_x, E_y and E_z, magnetic field B_y, and B_z from the top to the bottom. 68

3.14 The time-space evolution of the magnetic field B_z. 69

3.15 Space-time evolution of the $z-$ component of magnetic field. The black color shows out of the walls, and the white region is the upstream of the two shocks. An energetic electron trajectory is superimposed. The slope of red line corresponds to the velocity of 0.136c. The time evolution of the energy (middle panel) and the electrostatic (red line) and magnetic (gray line) force experienced by the electron (right panel). 70

3.16 The profile of potential and magnetic field strength (a-c), phase space density of electrons (d-f) and ions (g-i) before, at and after the collision from left to right. The black lines in the middle panels show the plasma density at the corresponding time. The black and red lines in the bottom panels show the ion and electron temperature, respectively, at the corresponding time. The blue line shows the sum of the electron and ion temperature. The orange lines correspond to 3.9. 71

3.17 An accelerated ion trajectory (a, d) and time evolution of the energy (b) and $E_y v_{iy}$ (c) as displayed in black. An energetic electron trajectory (a, d) and time evolution of the energy (e) and $-E_y v_{ey}$ (f) around the colliding as displayed in red. Here γ_e and γ_i are the Lorentz factors of the electron and the ion. The color map is the space-time evolution of B_z (a) and E_y (d). . . 71

3.18 The solid line shows upstream electron energy distribution function at $t\omega_{ci} = -15$. Blue line with the index $\mu = 1.4$ is indicated as a reference. The dashed line shows the Maxwell distribution with the initial upstream condition. 72

3.19 (a) Space-time evolution of the $y-$ component of the magnetic field and (b) the enlarged view with a different scale of By. White dashed line corresponding the speed of 0.02c is indicated as a reference. 73

3.20 Time evolution of the increment of the $y-$ (solid) and $z-$ (dashed) component of the magnetic field fluctuations (top panel), the parallel (solid) and perpendicular (dashed) electron plasma beta (middle panel) and the criteria of the fire hose instability (bottom panel). 74

3.21 Schematic condition of the SDA in $v_{||} - v_{\perp}$ space on the upstream rest frame. 74

3.22 (a) and (b) are phase space of parallel and perpendicular velocity from the test particle simulation. Red and black points indicate the initial and final position of the particles for $\kappa = 0.5$ (a) and $\kappa = 0.01$ (b). The dashed curve corresponds with the speed of $0.9c$ and $0.97c$. Electron phase space density for parallel and perpendicular velocities between the two shocks from the PIC simulation at $t\omega_{ci} = -35$ before the LAWs are excited (c) and $t\omega_{ci} = -15$ after the excitation (d). 75

3.23 The time-space evolution of the magnitude of the magnetic fields 81

3.24 Profiles of the density, pressure, electric fields, and magnetic fields. 82

3.25 Left panels: electron phase space density of v_x, v_y, and v_z from the top to the bottom. Right panels: ion phase space density of v_x, v_y, and v_z from the top to the bottom. 83

3.26 Top panels: the electron phase space density of v_x and the magnetic field B_y. Middle panels: the ion phase space density of v_x and the plasma density. Bottom panels: the ion phase density of ion energy and the ion pressure. 83

3.27 Ion trajectories on the space-time evolution of the plasma density and the time evolution of the ion energy. Orange box shows the enlarged view. . . . 84

3.28 Ion energy spectrum between the two shocks for three times ($t\omega_{ci} = 42, t\omega_{ci} = 63$ and $t\omega_{ci} = 80$). 84

3.29 Left panel: the time-space evolution of the ion density (left side) and the ion pressure (right side). Right panel: the profile of the ion and electron pressure at $t\omega_{ci} = 76$. 85

3.30 Cumulative spectra for the number of ions and the ion pressure. 85

3.31 Time-space evolution of the density in the case without energetic ions. The density is normalized by the upstream density before the collision. 86

3.32 Time-space evolution of the density (left-side) and the pressure (right-side) in the case with energetic ions. The density and pressure are normalized by ρ_L and P_L. 86

4.1 Time profile of magnitude of the magnetic field measured on Wind, ACE, and CLUSTER 1 from the top to the bottom. This plot is created by AMDA 94

4.2 Time profile of magnitude of the magnetic field, density, bulk velocity, and radial component of the temperature. This plot is created by AMDA 95

4.3 Electron flux measured on EPAM of ACE averaged in 5 minutes. This plot is created by CDAWeb. 96

4.4 Electron number flux 27 keV to 520 keV as a function of energy in 7 channels. Top panel: spectrogram. Second: as stacked plot. Third to ninth panels: time-varying energies in 7 channels. This plot is created by CDAWeb. 97

4.5 Top panel: the magnitude of the magnetic field. Middle panel: electron flux for six channels from $39 \sim 244$ keV. Bottom panel: ion flux for eight channels from $28 \sim 4007$ keV. This plot is created by CSA. 98

4.6 Pitch angle distribution of electrons. This plot is created by CSA. 98

4.7 Standoff distance calculated from the solar wind ram pressure. 99

4.8 Top panel: the time evolution of the number of electrons at the center of the simulation box. Bottom panel: the time evolution of the electron pitch angle distribution at the center of the simulation box. 99

SUMMARY

Collisionless shocks can produce high energy particles (cosmic rays in astrophysical context). Many works discussed dynamics of the collisionless shocks and their roles in particle acceleration mechanisms. However, almost all the works are about a single shock. Multiple shock waves can exist in a close region and they can collide with each other. Such a shock-shock interaction has been observed in the heliosphere by in-situ measurements. It is reported that the shock-shock interaction can accelerate particles to higher energies than acceleration by a single shock. However, it is not well-understood how the shock-shock interaction can efficiently accelerate particles. It is also thought that the shock-shock interaction plays an important role in producing ultra high energy cosmic rays in astrophysical environments.

In this dissertation, we use both numerical simulations (a test particle simulation and a full particle-in-cell simulation) and in-situ observational data obtained by several spacecraft to study particle acceleration and modification of shock structures in shock-shock interaction. The dissertation contains three topics and an introduction that describes the findings within the context of shock-shock interaction. Theoretical basis of collisionless shock waves is briefly reviewed and methods used in this thesis are presented. A short history of shock-shock interaction including theory and observations are discussed. The main aim of this thesis is to show that shock-shock interaction can produce energetic particles (both ions and electrons). We will discuss its detailed physical mechanisms by considering kinetic effects.

In the first topic, we discuss that stationary two shock waves can accelerate particles beyond the acceleration limit of a single shock. We use a test particle simulation in which particles undergo a random motion around the two shock waves. Solving the diffusion convection equation, we reproduce the double power-law spectrum obtained from the test particle simulation. An important point when considering a particle acceleration in multiple

shocks system is to take into account for the velocity dependence of the spatial diffusion coefficient. Although this is not related to the acceleration rate of a single shock, this plays an important role for multiple shocks acceleration.

The second topic addresses a full particle-in-cell simulation in which two shock waves collide head-on. For a perpendicular case, we confirm that ions are accelerated in the same way as discussed by Cargill et al. 1986. Shock structures after the collision are well-fitted with the MHD prediction. We do not find strong electron acceleration in this case because of the small gyro radius. It is expected, however, that the electrons are accelerated in turbulent electromagnetic fields created by the collision. This acceleration is called the second Fermi acceleration. For a quasi-perpendicular case, electrons are reflected at the shock front and escape upstream. Those reflected and accelerated electrons reach the other shock and are reflected there again. This process can be the same as the original idea of Fermi acceleration. These reflected electrons excite large amplitude waves due to the firehose instability. Since the large amplitude waves pitch-angle scatter these electrons in the phase space, pitch-angle scattered electrons are possibly carried the outside of the loss-cone of the shock waves. Therefore, electrons can be accelerated without limit. For a quasi-parallel case, ions escape upstream. Those ions reach the other shock and can gain energy by the scatter-free acceleration. Accelerated ions are trapped at the shock front. When the two shocks are closely located with its separation distance less than an ion gyro radius, these ions are rapidly accelerated during the gyro motion. Energetic ions between the two shocks have a pressure larger than the pressure downstream. It can decelerate the shock waves and change the shock structures. This means that kinetic effects can modify the MHD description of the shock, thus it is critical to take it into consideration for analysing the shock-shock interaction.

In the last topic we investigate an in-situ observation of shock-shock interaction where an interplanetary shock and the Earth's bow shock collide. We report for the first time a signature of the electron acceleration observed in shock-shock interaction. Nearly relativistic

electrons (over hundreds of keV), presumably accelerated by shock waves were observed at 1 AU. We perform a detailed analysis of a shock-shock interaction event with ACE, Wind, and CLUSTER. We discuss several scenarios for producing the observed energetic electrons and conclude that the acceleration due to the two shock waves is the most likely. The IP shock or the bow shock alone does not accelerate electrons. However, when the two shocks exist in a close region the pair can produce nearly relativistic electrons.

PUBLICATIONS

This thesis is based on two papers below. They have not been included in prior theses and are published in international peer-reviewed journals. The original abstracts and the contribution of the author of this thesis are summarized here.

Paper I. Electromagnetic Structure and Electron Acceleration in ShockShock Interaction

Masaru Nakanotani, Shuichi Matsukyo, Tohru Hada, and Christian X. Mazelle, *The Astrophysical Journal*, Volume 846, Number 2, September 2017, doi: 10.3847/1538-4357/aa8363

Abstract: A shock-shock interaction is investigated by using a one-dimensional full particle-in-cell simulation. The simulation reproduces the collision of two symmetrical high Mach number quasi-perpendicular shocks. The basic structure of the shocks and ion dynamics is similar to that obtained by previous hybrid simulations. The new aspects obtained here are as follows. Electrons are already strongly accelerated before the two shocks collide through multiple reflection. The reflected electrons self-generate waves upstream between the two shocks before they collide. The waves far upstream are generated through the right-hand resonant instability with the anomalous Doppler effect. The waves generated near the shock are due to firehose instability and have much larger amplitudes than those due to the resonant instability. The high-energy electrons are efficiently scattered by the waves so that some of them gain large pitch angles. Those electrons can be easily reflected at the shock of the other side. The accelerated electrons form a power-law energy spectrum. Due to the accelerated electrons, the pressure of upstream electrons increases with time. This appears to cause the deceleration of the approaching shock speed. The accelerated electrons having sufficiently large Larmor radii are further accelerated through the similar mechanism working for ions when the two shocks are colliding.

Contribution: The author took part in the preparation and performance of the simula-

tion presented and performed its analysis. The author wrote all parts of the paper directly with some help by co-authors.

Paper II. Diffusive shock acceleration of cosmic rays from two stationary shocks

Masaru Nakanotani, and Tohru Hada, Shuichi Matsukyo, *Earth, Planets and Space*, Volume 70, Number 1, February 2018, doi: 10.1186/s40623-018-0799-3

Abstract: Diffusive shock acceleration (Fermi acceleration) of cosmic rays in a system containing two shock waves is investigated using test particle simulations and analysis of the diffusion convection equation. We assume that the cosmic ray acceleration timescale is much less than the approaching timescale of the two shocks. Low-energy cosmic rays are primarily accelerated as they interact with one of the two shocks. However, as they are energized, and their mean free path becomes comparable to the separation distance of the two shocks, they start to accelerate as they interact with both shocks. As a result, a double power-law-type spectrum for the cosmic ray distribution is produced. The numerical result is well explained by a model based on the diffusion convection equation, which accounts for the dependence of the diffusion coefficient on the cosmic ray energy. The break point of the spectrum can be estimated by considering transport of cosmic rays from one shock to the other.

Contribution: The author was responsible for the test-particle simulation, solved the diffusion convection equation for the interpretation, and wrote the manuscript. Co-authors corrected the manuscript.

CHAPTER 1

GENERAL INTRODUCTION

1.1 A Brief Overview of Space Plasma Physics

Space is full-filled with plasma.

Plasma consists of an approximately equal number of positively and negatively charged particles. They make collective electromagnetic interactions. Especially, the space plasma considered in this thesis is in the state of "collisionless" meaning that the Coulomb collision between two particles is unimportant compared with effective collision via electromagnetic waves induced by the collective motion of plasma. For example, the mean free path of the Coulomb collision is about 1 AU in the solar wind plasma. The scale of significant behaviors in the solar wind are much less than the Coulomb-collision mean free path. Due to the enormously long relaxation time scale, the collisionless plasma allows distribution functions that are not in thermal equilibrium. Co-existence of non-thermal particles with nearly maxwellian core is an example of such a non-thermal equilibrium plasma. Similarly, the cosmic rays, an extremely low density and high energy particles, can co-exist with the main body of the plasma, that would quickly lose energy and be absorbed into the main body if the plasma is collisional. How can we theoretically treat a collisionless plasma? Several hierarchies exist depending on what we want to know. A rigorous formulation is the Vlasov-Maxwell system. Vlasov equation is written as,

$$\frac{\partial f_s}{\partial t} + \mathbf{v} \cdot \nabla f_s + \frac{q_s}{m_s}\left(\mathbf{E} + \frac{\mathbf{v}}{c} \times \mathbf{B}\right) \cdot \nabla_{\mathbf{v}} f_s = 0 \tag{1.1}$$

[Vlasov, 1945]. Here, $f_s(\mathbf{r}, \mathbf{v}, t)$ is the distribution function in the real and velocity space, $\mathbf{E}$ and $\mathbf{B}$ are the electromagnetic fields, e_s is the electric charge, m_s is the mass, and $\nabla_{\mathbf{v}}$ is the gradient operator in velocity space. The subscript s represents species. Maxwell

equations are

$$\nabla \cdot \mathbf{E} = 4\pi\rho_q, \tag{1.2}$$

$$\nabla \cdot \mathbf{B} = 0, \tag{1.3}$$

$$\nabla \times \mathbf{E} = -\frac{1}{c}\frac{\partial \mathbf{B}}{\partial t}, \tag{1.4}$$

$$\nabla \times \mathbf{B} = \frac{4\pi}{c}\mathbf{j} + \frac{1}{c}\frac{\partial \mathbf{E}}{\partial t}, \tag{1.5}$$

where ρ_q is the net charge density, $\mathbf{j}$ is the current density, and c is the speed of light. In this dissertation we use Gausian units. In this system, no assumption is made to describe a collisionless plasma. Therefore, any phenomena in the plasma, in principle, can be reproduced in the system. Although the easiest way to understand is to solve the Vlasov-Maxwell system by adapting an appropriate initial condition, the life is not so simple. Even in a simple situation in which there is no background magnetic field (an electrostatic case), it is difficult to obtain the solution. For example, Cédric Villani received the Fields Medal for his proofs of nonlinear Landau damping and convergence to equilibrium for the Vlasov equation [Mouhot and Villani, 2010].

Instead of dealing with time evolution of the distribution function, fluid formulation treats time evolution of macroscopic variables of the plasma (such as the density, bulk velocity, and pressure) defined by moments of the distribution function. In this case, we do not take into account for non-thermal particles. We can only address physical quantities averaged over the velocity space. Integrating (1.1) in the velocity space with multiplying it by v^0 and $\mathbf{v}$ we obtain,

$$\frac{\partial n_s}{\partial t} + \nabla \cdot (n_s \mathbf{U}_s) = 0, \tag{1.6}$$

$$m_s n_s \frac{\mathrm{d}\mathbf{U}_s}{\mathrm{d}t} = n_s e_s \left(\mathbf{E} + \frac{\mathbf{U}_s}{c} \times \mathbf{B} \right) - \nabla \cdot \overleftrightarrow{\mathbf{P}}_s, \tag{1.7}$$

where n_s is the average density, $\mathbf{U}_s$ is the average velocity, and $\overleftrightarrow{\mathbf{P}}_s$ is the pressure tensor.

Although we can do the same thing for higher moments, it is never closed. We need to compromise at same point to close the system. A simple approach is to employ the adiabatic equation of motion,

$$\overleftrightarrow{\mathbf{P}}_s = \overleftrightarrow{\mathbf{1}} P_s, \tag{1.8}$$

$$\frac{\mathrm{d}}{\mathrm{d}t}\left(\frac{P_s}{n_s^{\gamma}}\right) = 0, \tag{1.9}$$

where $\overleftrightarrow{\mathbf{1}}$ is the unit tensor and γ is the polytrope index [Fetter and Walecka, 1980]. Another approach, for example, is the Chew-Goldberger-Low equation of state,

$$\frac{\mathrm{d}}{\mathrm{d}t}\left(\frac{P_{s\perp}}{n_s B}\right) = 0 \quad \text{and} \quad \frac{\mathrm{d}}{\mathrm{d}t}\left(\frac{P_{s||} B^2}{n_s^3}\right) = 0, \tag{1.10}$$

where $P_{s||}$ and $P_{s\perp}$ are the pressure parallel and perpendicular to the magnetic field, respectively [Chew et al., 1956]. Instabilities originating from the shape of the velocity distribution function and particle acceleration to produce is no longer treated self-consistently in the system. That's it? Is there nothing further we can do?

When the time-scale of phenomena in a collisionless plasma we consider is much longer than the ion-cyclotron frequency, plasmas are electrically neutral and the net charge density almost equals to zero because electrons are so quickly to counteract. Also, the displacement current can be neglected compared with the order of the current with other terms. Summing up the conservation-law of the density for ion and electron, we obtain,

$$\frac{\partial \rho_m}{\partial t} + \nabla \cdot (\rho_m \mathbf{U}) = 0, \tag{1.11}$$

where $\rho_m = \Sigma_s m_s n_s$ and $\mathbf{U} = \frac{1}{\rho_m}\Sigma_s m_s n_s \mathbf{U}_s$. Summing the momentum equations of the two-fluid model, we get,

$$\rho_m \frac{\mathrm{d}\mathbf{U}_s}{\mathrm{d}t} = \frac{\mathbf{j}}{c} \times \mathbf{B} - \nabla \mathbf{P}, \tag{1.12}$$

where $\mathbf{P}$ is the total pressure for ions and electrons. Here, we assume that the pressure is isotropic. Subtracting the two momentum equations, the generalized Ohm's law is derived. Here, we use of the fact $m_e \ll m_i$. Writing a simple form of Ohm's law down,

$$\mathbf{E} + \frac{\mathbf{U}}{c} \times \mathbf{B} = \eta \mathbf{j}, \tag{1.13}$$

where η is the magnetic resistivity. To close the system, we use the equation of state. This system is often called the resistive magnetohydrodynamics (MHD) [Cowling, 1976]. Electrons at this scale only play a role to neutralize the plasma and follow ions. The motion of ion almost determines the motion of plasma.

As we have seen, from the Vlasov-Maxwell system to the MHD, the degree of freedom in a collisionless plasma is reduced by sacrificing micro-scale physics. Here, we add one more treatment in a plasma. When we do not need to consider feed-back effects on electromagnetic fields from plasma. We can treat particles as a test particle. In that case, we just solve the equation of motion for test particles according to the given electromagnetic fields.

Plasma physics is like golf. If you want to send your ball far away, you use a driver. This means that when you want to know macro-scale physics of plasma, you can apply MHD on the phenomena. On the other hand, if you want to send your ball into a cup in a green, you use a putter. This corresponds to that when you want to know micro-scale physics of plasma, you have to handle the Vlasov-Maxwell system. By utilizing these clubs depending on the situation, we are able to understand how a collisionless plasma works in space. In the next chapter, we get into one of the most prominent problem in space.

1.2 Collisionless Shock Waves

So far, many authors have studied many characteristics of collisionless shock waves theoretically, using observational measurements, and computer simulations. Historically, the

existence of a collisionless shock wave was first pointed out by Courant and Friedrichs [1948]. De Hoffmann and Teller [1950] developed the theory of a magnetized shock waves. Observationally, Sonett and Abrams [1963], Ness et al. [1964] reported the first in-situ measurement of a collisionless shock wave using spacecraft flying around the Earth. They found that the shock transition scale was much less than the mean Coulomb collision mean free path, i.e., 1 AU, indicating that there exists an effective collective plasma process that provides efficient dissipation to the shock. To understand the physics of a collisionless shock wave, we have to handle from the MHD to the Vlasov-Maxwell system.

1.2.1 MHD shocks

Next, we derive the Rankine-Hugoniot relation that states a balance between the upstream and the downstream fluxes. We assume a steady state ($\partial/\partial t \sim 0$), and take a cartesian coordinate with the shock at rest. The upstream and downstream values are assumed to be constant. The flux conservation relations are,

$$\rho_1 v_{x1} = \rho_2 v_{x2}, \tag{1.14}$$

$$\rho_1 v_{x1}^2 + P_1 + \frac{B_{y1}^2 + B_{z1}^2}{8\pi} = \rho_2 v_{x2}^2 + P_2 + \frac{B_{y2}^2 + B_{z2}^2}{8\pi}, \tag{1.15}$$

$$\rho_1 v_{x1} v_{y1} - \frac{B_{x1} B_{y1}}{4\pi} = \rho_2 v_{x2} v_{y2} - \frac{B_{x2} B_{y2}}{4\pi}, \tag{1.16}$$

$$\rho_1 v_{x1} v_{z1} - \frac{B_{x1} B_{z1}}{4\pi} = \rho_2 v_{x2} v_{z2} - \frac{B_{x2} B_{z2}}{4\pi}, \tag{1.17}$$

$$\left(\frac{\rho_1 v_1^2}{2}+\frac{\gamma_h}{\gamma_h-1}P_1\right)v_{x1}+\frac{B_{y1}^2+B_{z1}^2}{4\pi}v_{x1}-\frac{(B_{y1}v_{y1}+B_{z1}v_{z1})B_{x1}}{4\pi}=$$
$$\left(\frac{\rho_2 v_2^2}{2}+\frac{\gamma_h}{\gamma_h-1}P_2\right)v_{x2}+\frac{B_{y2}^2+B_{z2}^2}{4\pi}v_{x2}-\frac{(B_{y2}v_{y2}+B_{z2}v_{z2})B_{x2}}{4\pi}, \tag{1.18}$$

$$v_{x1}B_{y1}-v_{y1}B_{x1}=v_{x2}B_{y2}-v_{y2}B_{x2}, \tag{1.19}$$

$$v_{x1}B_{z1}-v_{z1}B_{x1}=v_{x2}B_{z2}-v_{z2}B_{x2}, \tag{1.20}$$

$$B_{x1}=B_{x2}, \tag{1.21}$$

where the values with the subscript 1 (2) mean the upstream values (downstream values). Here, $\mathbf{v}_1=(v_{x1},0,0)$ and $\mathbf{B}_1=B_0(\cos\theta_{Bn1},0,\sin\theta_{Bn1})$. The angle θ_{Bn1} is defined as an angle between the background magnetic field and the x axis (Fig. 1.1). Equations above represent conservation of the mass flux (1.14), momentum flux normal to the discontinuity (1.15), momentum flux tangential to the discontinuity (1.16)-(1.17), energy flux (1.18), tangential electric field (1.19)-(1.20), and the normal magnetic field (1.21). All of these equations can be derived by first writing the MHD set of equations in the conservation form, drop the time derivative terms, and finally by integrating the equations by x between two stationary points upstream and downstream. From these equations, we can derive the function of the compression ratio r ($r=v_{x1}/v_{x2}=\rho_2/\rho_1$),

$$(r-1)[\{\gamma_h\beta_1+M_I^2(\gamma_h-1)\}r^3-M_I^2\{2\gamma_h\beta_1+\gamma_h+1+(\gamma_h-2+\gamma_h\cos^2\theta_{Bn1})M_I^2\}r^2$$
$$+M_I^4\{\gamma_h\beta_1+\gamma_h+(\gamma_h+2)\cos^2\theta_{Bn1}+(\gamma_h-1)M_A^2\}r-(\gamma_h+1)M_A^2M_I^4]=0. \tag{1.22}$$

Here, $M_A = v_{x1}/v_{A1}$, $M_I = M_A/\cos\theta_{Bn1}$, and $\beta_1 = P_1/(B_0^2/8\pi)$. Obtaining the value of r from (1.22), the downstream values are automatically determined,

$$v_{z2} = \frac{r-1}{M_I^2 - r}\frac{B_{z1}}{B_{x1}}v_{x1} \tag{1.23}$$

$$P_2 = P_1 + \rho_1 v_{x1}^2\left(1 - \frac{1}{r}\right) + \frac{B_{z1}^2}{8\pi}\left[1 - \left\{\frac{r(M_I^2-1)}{M_I^2 - r}\right\}^2\right] \tag{1.24}$$

$$B_{z2} = \frac{M_I^2 - 1}{M_I^2 - r} r B_{z1}. \tag{1.25}$$

When $\theta_{Bn1} = 90^\circ$, (1.22) becomes

$$(r-1)\left[-(\gamma_h - 2)r^2 + \left\{\gamma_h\beta_1 + \gamma_h + (\gamma_h - 1)M_A^2\right\}r - (\gamma_h + 1)M_A^2\right] = 0, \tag{1.26}$$

and the values downstream are

$$v_{z2} = 0, \tag{1.27}$$

$$P_2 = P_1 + \rho_1 v_{x1}^2\left(1 - \frac{1}{r}\right) + \frac{B_{z1}^2}{8\pi}(1 - r^2), \tag{1.28}$$

$$B_{z2} = r B_{z1}. \tag{1.29}$$

Fig. 1.2 shows Mach number dependence for the compression ratio in the panel (a) and the entropy differential downstream in the panel (b) at the parameters $\beta = 1$ and $\theta_{Bn1} = 60^\circ$. According to the second law of thermodynamics (law of entropy increase), a shock wave can exist only when $(S_2 - S_1)/C_v > 0$ where C_v is the specific heat ratio at constant volume. We can confirm that there are three shock waves for the specific modes. If we choose $\gamma = 5/3$, the compression ratio r of the fast mode shock approaches 4 as the Mach number M_A increases. In this dissertation, we discuss the fast mode shock wave.

1.2.2 Shock waves in Vlasov-Maxwell system

Marshall [1955] and Tidman and Krall [1972] found that, if the upstram Mach number exceeds a "critical Mach number" ($M_c \sim 2.7$), resistive dissipation (or the Joule heating) alone cannot provide sufficient dissipation to sustain the shock. Additional dissipation must be supplied by a viscous process, i.e., the ion-ion interaction. When the Mach number is below the critical Mach number, $M < M_c$, he shock is called sub-critical, and when $M > M_c$ the shock is super-critical.

In a subcritical regime, when the incoming particles encounter the shock front, a cross-shock potential is produced due to the difference of the ion and electron inertia. Although this potential is not strong to reflect ions upstream, electrons drifting along the shock front give a contribution for the dissipation at the shock front. In a supercritical regime, shock waves reflect some of incoming ions upstream [Gosling and Thomsen, 1985]. These reflected ions play a role as a free-energy source in the transition region and several instabilities are excited. These instabilities dissipate the incoming particles to maintain the shock structure and act as effective viscosity [Burgess and Scholer, 2007].

Quasi-perpendicular shock waves

For a quasi-perpendicular supercritical shock ("perpendicular" means that the normal direction of the shock waves is perpendicular to the magnetic field), the foot region (depicted in Fig. 1.3) in front of the shock wave is created because reflected ions cannot escape upstream. The ion-ion instability generates waves in the foot region. These waves are in the whistler and lower hybrid frequency range [Papadopoulos, 1988, Wu et al., 1984]. Instabilities related to electrons are also excited in the foot region: Bunemann instability [Papadopoulos, 1988, Shimada and Hoshino, 2000, Schmitz et al., 2002]. During the relaxation, electrostatic holes are produced in the foot region and play an important role to produce energetic electrons [Hoshino and Shimada, 2002, Shimada and Hoshino, 2000] Another instability is the modified two-stream instability (MTSI) [Scholer and Matsukiyo,

2004, Matsukiyo and Scholer, 2003]. Because there has to be no current in the plasma flow, in the foot region, electrons are decelerated. The velocity difference between ions and electrons excite the MTSI. Generated waves are on the whistler mode branch.

Another prominent feature of a quasi-perpendicular shock is the shock reformation. The shock front is no longer time-stationary and fluctuates quasi-periodically. The shock reformation has been reported in a lot of computational works [Biskamp and Welter, 1972, Lembège and Dawson, 1987, Lembege and Savoini, 1992, Lembège and Savoini, 2002, Hellinger et al., 2002, Matsukiyo and Scholer, 2003, Scholer et al., 2003, Scholer and Matsukiyo, 2004]. Reflected ions are a main actor for the shock reformation. They gyrate in front of the shock front. The tip of the reflected ions stops when going back to the shock front. Hence, the density and the following magnetic field piled at the tip region and the new shock front appears. The time-scale of this cycle is about the ion-gyro period.

The last point which we mention about a quasi-perpendicular shock wave is the rippled shock front. It has been first pointed out by Winske and Quest [1988]. In this paper, they perform 2D hybrid simulations and mentioned that the shock front is rippled because of the Alfvén ion-cyclotron instability which is excited by the ion temperature anisotropy, $T_{i\perp}/T_{i||} > 1$. Here, $T_{i\perp}$ and $T_{i||}$ denote the ion temperature perpendicular and parallel to the magnetic field. The rippled shock front in a use of full PIC simulation has been also reported in these articles [Lembege and Savoini, 1992, Lembège and Savoini, 2002, Matsukiyo and Matsumoto, 2015].

Quasi-parallel shock waves

Now let us turn our attention to quasi-parallel supercritical shock. Here, "parallel" means that the normal direction of the shock waves is parallel to the magnetic field. In contrast to quasi-perpendicular shocks, reflected ions can travel to large distance upstream from the shock front. These reflected ions are observed as an ion beam and actually observed at the Earth's bow shock [Gosling et al., 1978, Paschmann et al., 1981]. The beam component

as a free energy source can excite waves which is usually observed as upstream waves with low-frequency ($\sim$ 50 mHz) and large amplitude ($> 0.2B$). CLUSTER observation reveals that observed waves are in cyclotron resonance with the ion beam and have right-hand polarization [Mazelle et al., 2000, 2003]. Possible excitation mechanisms are the firehose instability which produces long-wavelength negative-helicity Alfvén waves and the resonant left-hand ion-ion beam instability. These excited waves experience non-linear steeping and grow to the short-large amplitude waves (SLAMS) at the shock front.

The shock reformation of a quasi-parallel shock wave also arises [Burgess, 1989, Scholer et al., 2003, Tsubouchi and Lembège, 2004]. Large amplitude upstream waves make the local shock angle quasi-perpendicular. Behavior of plasma at the shock front acts like a quasi-perpendicular shock wave. The shock wave moves periodically. It is pointed out that the shock reformation is related to the rippled shock front [Hao et al., 2017].

1.3 Cosmic Rays

One of the most outstanding and long-lasting problems in space and astrophysics is "how are cosmic rays (CRs) produced?".

CRs are energetic particles (ions and electrons) accelerated in space. Historically, Hess took a balloon flight to confirm that energetic particles causing ionizing radiation in a ionization chamber came from the underground. However, he found that the rate of the ionizing radiation increased as he rose up. It is about 9 times larger at 5000 m hight. Fig. 1.6 and Fig. 1.7 show CR energy spectrum measured by several experiments [Hanlon, 2008]. One can see that the flux of CRs covers a tremendous range of energies. Both of the axes are plotted in a logarithmic scale. The energy of CRs can reach to energy several orders larger than particles made in the particle accelerator, LHC at CERN. The flux is roughly close to a power-law distribution which is written as

$$N(E)\,dE \propto E^{-\gamma} dE. \tag{1.30}$$

Here, γ is called the spectral index of the flux. The power-law distribution indicates non-thermal particles are produced in space. CRs are born somewhere in space and then propagate to the Earth.

The birth place of CRs can be everywhere in space. It is believed that CRs below $10^{15.5}$ eV are produced in the Galaxy such as supernova remnants [Drury, 2012, Blandford et al., 2014, Blasi, 2013]. A bulging point of the CR spectrum at the energy around $10^{15.5}$ eV is called "knee". Above $10^{15.5}$ eV, CRs come from the outside of the Galaxy [Drury, 2012, Blandford et al., 2014, Harari, 2014]. The flux right below the energy 10^{20} eV is cut-off because of "GZK cutoff" [Greisen, 1966] . The point where the CR spectrum is bent around ($\sim 10^{19}$ eV) is called "Ankle".

It is thought that collisionless shock waves can produce the universal spectral index of the CR flux. A standard theory of CR acceleration at shock waves is called the diffusive shock acceleration (DSA) [Krymskii, 1977, Axford et al., 1977, Bell, 1978, Blandford and Ostriker, 1978, Drury, 1983]. In the theory, particles are scattered around the shock front due to turbulence excited upstream and downstream. The particles can gain energy as they repeatedly travel the two regions. The resultant spectral index of the DSA theory follows as

$$\gamma = \frac{r+2}{r-1} \tag{1.31}$$

where r is the compression ratio of the shock wave dominantly controlled by Mach number [Kennel et al., 1989]. According to the magnetohydrodynamics (MHD), the largest compression ratio is 4 [Kennel et al., 1989]. Because astrophysical shocks are usually in high Mach number regime ($100 \sim 1000$), the spectral index becomes $\gamma \sim 2$. Considering propagation effects of CRs, it is expected that the observational spectral index is about $2 \sim 2.5$. Since the DSA theory can explain the observational spectral index well, collisionless shock waves are the first candidate of a CR produced site.

Observational evidences of ion and electron acceleration at collisionless shock waves have been obtained by monitoring supernova remnant shock waves. Ackermann et al.

[2013] shows that protons are accelerated greater than a few GeV at a collisionless shock waves. They observe supernova remnants IC 443 and W44 with the *Fermi* LAT. Proton-proton collisions create neutral pions π^0 and then they quickly decay into two gamma rays. They estimate accelerated proton energy from the observed Gamma-ray spectra (Fig. 1.8). Electrons can be also accelerated at collisionless shock waves to relativistic energy [Uchiyama et al., 2007]. They measured X-ray emission from RX J17 13.7-3946 with the imaging array of the Chandra Advanced CCD Imaging Spectrometer (Fig. 1.9). It shows that there is strong synchrotron emission from ultra relativistic electrons. They estimate that electrons are accelerated to $\sim$ TeV. They also points out that the magnitude of the magnetic field have to be amplified by a factor of more than 100 which is far beyond the limitation of the shock compression.

It is now well-documented that a collisionless shock are capable of producing high energy particles. However, we do not understand well how those energetic particles are accelerated. Next, we get into the detail of the physics of collisionless shock waves and a particle acceleration mechanism which has been established so far.

1.4 Particle Acceleration

As we mentioned earlier, we expect that a collisionless shock wave would be an efficient particle accelerator. We introduce what we understand about particle acceleration in a collisionless shock wave here.

We believe that the diffusive shock acceleration (DSA) is a main acceleration mechanism to accelerate the cosmic rays in space. There are two approximations normally used in discussion of the DSA. The first is that particles already have enough energy to cross the shock transition region. This assumption, i.e., the injection problem will be further discussed later. The second point is that there are MHD-scale turbulence both upstream and downstream. Based on these assumptions, particles can gain energy. Let us consider how particles are accelerated. Particles gain energy when they collide head-on with the upstream

MHD turbulence which is convected toward the shock with speed u_1. On the contrary, particles lose energy when they collide rear-end with the downstream MHD turbulence that is convecting away from the shock with speed u_2. Since the shock is compressional as definition, the upstream flow is always faster than the downstream flow ($u_1 > u_2$), after one cycle of the collisions particle gain energy. The average energy gain is expressed as

$$\left\langle \frac{\Delta E}{E} \right\rangle = \frac{4}{3}\left(\frac{v}{c}\right) = \frac{4}{3}\left(\frac{u_1 - u_2}{c}\right). \tag{1.32}$$

Assuming the velocity distribution of CRs is isotropic, the probability P for a particle to return upstream is

$$P = 1 - \frac{u_1}{c}. \tag{1.33}$$

After k cycles, the number of particles will be $N = N_0 P^k$ with energy above $E = E_0 \beta^k$, where $\beta = 1 + \frac{4}{3}\frac{v}{c}$. Combining these, we obtain the integral spectrum

$$\frac{N}{N_0} = \left(\frac{E}{E_0}\right)^{\frac{\log P}{\log \beta}}. \tag{1.34}$$

Transforming the integral spectrum into the differential spectrum,

$$\frac{\mathrm{d}N}{\mathrm{d}E} \propto E^{-1+\frac{\log P}{\log \beta}}. \tag{1.35}$$

The index of the energy spectrum Γ is calculated as

$$\Gamma \sim \frac{r+2}{r-1}, \tag{1.36}$$

where r is the compression ratio defined as u_1/u_2. This energy spectrum explains the observed cosmic ray spectrum well.

However, the DSA theory assumes pre-accelerated particles which are called "seed particles". Therefore, if there is no mechanism to produce seed particles, the DSA theory

collapses. This problem how seed particles are created is called the injection problem. Since both ion and electron must be accelerated and become cosmic rays, there are injection problems for ion and electron.

The ion shock surfing works for ions in a quasi-perpendicular shock wave [Sagdeev, 1966, Lee et al., 1996]. Some of ions are reflected at the shock front due to the shock electric potential and gain energy from the motional electric field during their gyration upstream. Although they go back to the shock front, if these ions do not still have enough energy to pass the shock potential, they surf along the shock surface. The estimated attainable maximum energy is

$$\mathscr{E}_{\max} \sim 2 m_i u_i^2 \frac{m_i}{m_e}, \tag{1.37}$$

where m_i and m_e are ion and electron mass, respectively.

The electron shock surfing acceleration has been conceived by Shimada and Hoshino [2000], Hoshino [2001], Hoshino and Shimada [2002]. In those reports, shock waves are perpendicular and in high Mach number regime (~ 30). Reflected ions excite waves through Bunemann instability and make a solitary wave in the foot region. Some electrons are trapped in an electron hole and are accelerated by the motional electric field. Even in 2D or 3D, it has been confirmed that the electron shock surfing still works for electron acceleration [Amano and Hoshino, 2009, Matsumoto et al., 2013, 2015, 2017].

Another electron acceleration mechanism is the shock drift acceleration [Sonnerup, 1969, Wu, 1984, Ball and Melrose, 2001]. Incoming electrons drift due to the gradient magnetic field of a shock wave at the shock front. Because the direction of the drift is anti-parallel against the motional electric field, they are accelerated. Some of the accelerated electrons are reflected and run away from the shock. It can be regarded as the mirror reflection in the de Hoffmann-Teller frame. Attainable energy is controlled by a factor $1/\cos\theta_{Bn}$. If we want to accelerate electrons, we can close the shock angle to 90° in which it is difficult for electrons to be reflected in the case. Recently, the DSA is applied to explain electron acceleration in galaxy clusters [Matsukiyo et al., 2011, Guo et al., 2014]. In that

case, the plasma temperature is so high that electron are reflected at shock front and highly accelerated even in a nearly perpendicular shock.

For a quasi-parallel shock wave, Sugiyama and Terasawa [1999], Sugiyama et al. [2001] suggested the scatter-free ion acceleration. The main idea is that ions trapped in a large amplitude upstream are accelerated when crossing the shock front. The waves are decelerated at the shock front because of the shock compression. There exists a difference between the waves in the border of the shock front. That leads the trapped ions to bounce back and forth across the shock transition and have a chance for acceleration. The acceleration has been confirmed in a full PIC simulation [Kato, 2015].

We have seen many works to understand the physics of a collisionless shock wave and particle acceleration. All of the works assume that the upstream flow does not change. In space, it is often that the upstream plasm of a shock wave possesses many structures (turbulence, discontinuities, and so on). Interaction between a shock wave and such structures could alter the shock structure and particle acceleration mechanism. We review some researches about those interactions in the next chapter.

1.5 Shock-Shock Interaction

Although many reports about collisionless shock waves are investigated intensively for decades, the upstream flow has been assumed to be uniform in many researches. It is rare that the upstream flow of a shock wave is static. Here, we show some examples of interactions between a shock wave and structures. Finally, we explain shock-shock interaction which is the main topic of this dissertation in more detail and mention what is our contribution in this thesis.

What happens when the upstream flow contains turbulence? It is observed by Voyager 1 that the solar wind is turbulent [Burlaga and Ness, 2009]. Giacalone and Jokipii [2007], Mizuno et al. [2010, 2014], Ji et al. [2016] investigate shock-turbulence interaction using MHD simulation. A prominent result is that the magnetic field would be amplified to

the value exceed the possible maximum amplification ratio of 4 expected from the jump condition. It is because, due to the presence of the large fluctuations, the shock front are rippled and then the rippled shock front introduces vorticity and swirling in the flow that then stretches and folds the magnetic field. It is expected that the interaction could be a solution for a large magnetic field amplification in a SNR shock wave. Since the magnetic field are highly tangled downstream, magnetic reconnections are supposed to take place and particles are accelerated downstream [Zank et al., 2015].

A favored particle acceleration occurs when a shock interacts with current sheets. Inclined current sheets would produce a hot flow anomaly when they encounter the shock wave [Giacalone and Burgess, 2010]. Because the direction of the magnetic field oppositely changes at the current sheet, particles drift along a current sheet taking a *S*-shaped trajectory and gain energy from the motional electric field upstream. At pulsar termination shocks, the pulsar wind consists of current sheets due to the rotation of the star. Lyubarsky [2003], Nagata et al. [2008], Sironi and Spitkovsky [2011] reported an efficient particle acceleration forming power-law spectrum for particle energy. Especially from the 2D full PIC simulation [Sironi and Spitkovsky, 2011], current sheets take place magnetic reconnections upstream and downstream and particles are accelerated in reconnected fields.

When the upstream flow contains a shock wave, two shock waves will eventually collide with each other. It is easy to imagine that a shock-shock interaction will significantly modify the shock structures. Particle acceleration would be not only quantitatively but also qualitatively different from the particle acceleration by a single shock wave. In this chapter, we review observational and theoretical results of a shock-shock interaction.

Let us start from the Sun. Sometimes, it is observed that two coronal mass ejections (CMEs) occur successively with a short separation time interval. These CMEs create a shock wave in front of each of them. If the one following travels faster than the preceding one, the following one can catches up the preceding one. Since the preceding shock can provide turbulence and energized particles downstream, the following shock further accel-

erate those seed particles in turbulent magnetic fields. As a result, protons with energy of $\sim$GeV/nucleon are observed in ground level enhancement events. This process is called "Twin CME scenario" [Li et al., 2012].

An interplanetary (IP) shock created by a CME can freely propagate in the Heliosphere and hit a planetary bow shock sometimes. Many solar system objects go with their planetary bow shock [Treumann and Jaroschek, 2008]. For instance, the collision of an IP shock to the Earth's bow shock has been observed with in-situ measurements [Hietala et al., 2011]. There were three spacecraft between the IP shock and the bow shock, ACE, WIND, and GEOTAIL. WIND observed gradual increasing and bursty ion flux in several channels ($0.043 - 2.8$ MeV) as the IP shock approached to the bow shock. The bursty ion flux increasing happened when the magnetic field was connected to both of the shocks. They conclude that ions can be accelerated through multiple reflection between an IP shock and the Earth's bow shock like Fermi acceleration.

IP shocks finally reach the Heliospheric termination shock (TS). MHD simulations shows that the collision emits transmitted magneto-sonic pulses and their associated reflected pulses [Washimi et al., 2011]. These pulses repeatedly reflect in the Heliosheath. This collision can cause to the change of the location of TS. Since IP shocks arrive at TS once in a year on average, the structure of the Heliosphere including TS can vary dynamically. A shock-shock interaction can play an important role to determine the structure.

Beyond the Heliosphere, there are many models proposed to explain ultra high energy cosmic rays (UHCRs) in astrophysical objects. For instance, an SN blast wave collides with the termination shock of a strong wind generated by the collective action of many massive stars in a compact cluster [Bykov et al., 2015]. This system can produce CRs well above PeV. Gamma-ray bursts (GRBs) are among the best candidate sources for UHECRs [Hillas, 1984]. In the internal shock model, the central engine emits the irregular wind by a succession of relativistic shells [Kobayashi et al., 1997]. When A rapid shell catches up a slower one, shock waves emerge. If multiple shells are emitted, multiple shock waves

provided by collisions could highly accelerate protons.

On the other hand, we can consider a shock-shock interaction from a theoretical point of view. In a macroscopic view, a shock-shock interaction in the ideal MHD system can be regarded as the Riemann problem. The Riemann problem is a kind of initial value problems for hyperbolic systems such as the system of equations of ideal hydrodynamics or ideal magnetohydrodynamics (MHD), in which the initial condition is given by two constant states separated by a discontinuity [Takahashi et al., 2013, 2014]. Because a shock wave is strictly a discontinuity in ideal MHD and information is not able to propagate upstream from the downstream, we see that at a collision two constant states are separated discontinuously. Considering this state as the initial condition, the evolution of this system can be described as the Riemann problem.

Because in an MHD approximation the shape of a distribution function of plasma is ignored by integrating over all of velocity space, dissipation at the shock front, turbulence upstream and downstream, and a particle acceleration are not described self-consistently.

Those kinetic effects are inevitable to understand shock structures in a shock-shock interaction. A shock-shock interaction would go through complex dissipation process at the shock front. A shock wave propagating turbulent plasma could be modified in the shock speed [Zank et al., 2002]. Particles accelerated through a shock-shock interaction have a possibility to vary the shock structure like a CR-modified shock [Drury and Falle, 1986].

In spite of the necessity of kinetic effects, there are few works on the shock-shock interaction including kinetic effects. Cargill et al. [1986], Cargill [1991b, 1990, 1991a] investigated a shock-shock interaction in which two shock waves collide head-on using a hybrid simulation . Fig. 1.13 shows phase-space plots for v_x and v_y. These panels are time series from the top to the bottom. After the collision, the shock waves propagate outward. In those papers, it is pointed out that ions are effectively accelerated. For a two quasi-perpendicular supercritical shocks case, ions are accelerated when the two shocks

encounter with in one ion-gyro radius. As a result, ions gain energy roughly 15 times lager than the shock bulk energy. At the collision, the magnetic field and the potential are piled up at the collision site (Fig. 1.14). For a two quasi-parallel supercritical shocks case, some ions can get off from the shock and swim against the upstream flow. They then encounter the other shock and would be reflected again. Repeating this process, ions gain energy and the maximum energy is about 50 times larger than the shock bulk energy [Cargill, 1991b]. This acceleration mechanism can be understood as Fermi acceleration.

However, electron kinetic effects are ignored in hybrid simulations. Although ions are treated as super-particles, electrons are treated as a massless and charge neutralizing fluid [Winske, 1985]. The electron momentum equation is rewritten as the generalized Ohm's law. Ignoring the electron inertia, whistler waves are not resolved correctly in a hybrid simulation.

To understand electron acceleration, we need to handle electron kinetic effects self-consistently in a simulation. Electron kinetic effects play a role for initial electron acceleration [Scholer and Matsukiyo, 2004]. In a hybrid simulation, non-thermal electrons are not resolved because electrons are treated as a fluid. When electrons are accelerated, they interact with electron scale waves through the wave-particle interaction [Riquelme and Spitkovsky, 2011, Amano and Hoshino, 2009, Matsumoto et al., 2015]. Those electron scale waves are usually produced by instabilities originating from plasma velocity distribution function [Matsukiyo and Scholer, 2006].

To understand shock structures and a particle acceleration in a shock-shock interaction system completely, we need to run a full particle-in-cell (PIC) simulation. In a full PIC simulation, ions and electrons are treated as super-particles. It is recognized as the first principle simulation and able to reproduce every plasma phenomena in principle. The simulation has been making significant contributions in our understanding of the physics of collisionless shocks [Treumann, 2009]. The simulation is able to provide an electron acceleration without any assumption.

1.6 Purpose of This Thesis

In this dissertation, we make the following points clear.

1. How efficient is particle acceleration in a multiple shock system?

2. Are kinetic effects are important?

3. Is there any difference between ion and electron acceleration?

This dissertation is organized as follows. In Chapter 2, we show using a theory and a Monte-Carlo simulation that two shock waves can highly accelerate particles above the limit of the strongest single shock. In Chapter 3, results from 1D full PIC simulations in which two shock waves collide with each other are introduced. We point out that a shock-shock interaction is an efficient particle accelerator more than a single shock wave. In Chapter 4, we bring an evidence from an in-situ observation that a shock-shock interaction actually accelerate particles in space. Conclusions and outlook is described in Chapter 5.

Figures

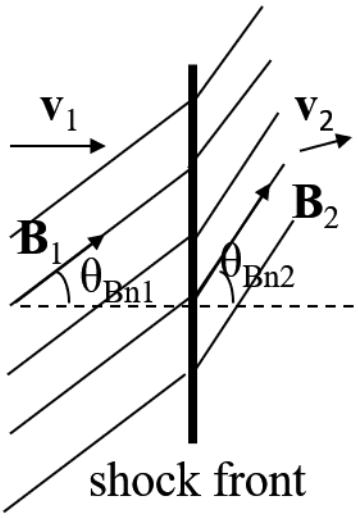


Figure 1.1: A shock configuration. The left (right) side divided by the shock front (black line) is the upstream (downstream)

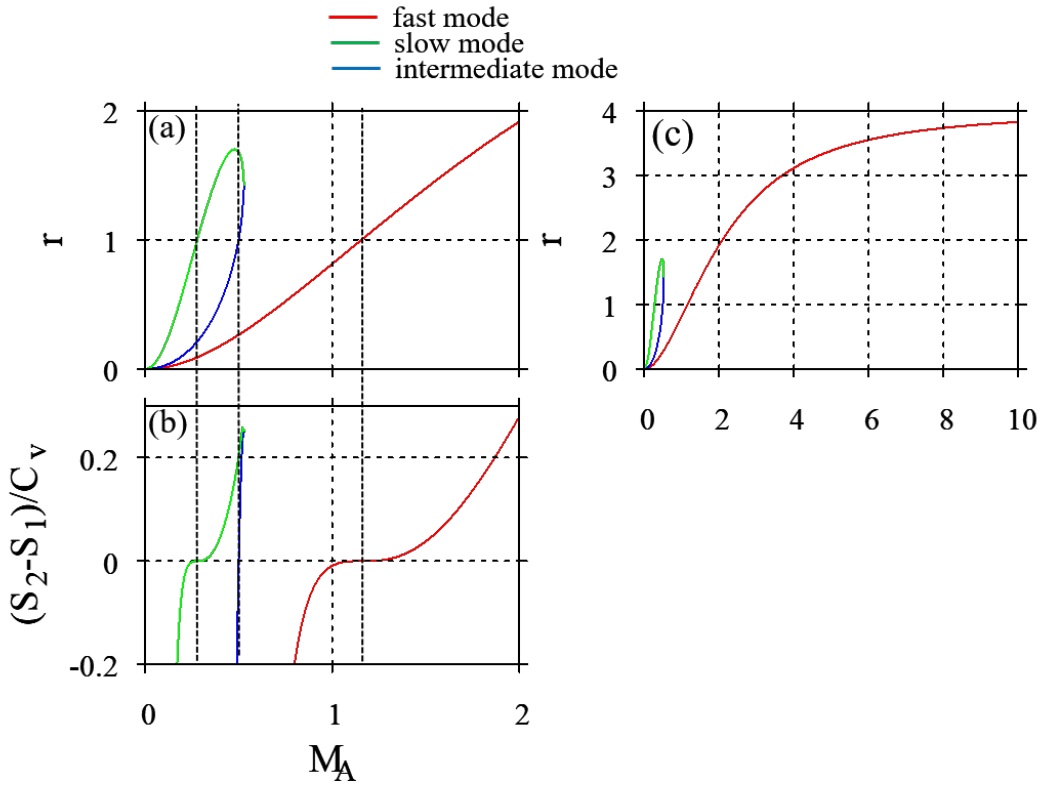


Figure 1.2: An example of the Rankine-Hugoniot relation whose parameters are $\beta = 1$ and $\theta_{Bn} = 60°$.

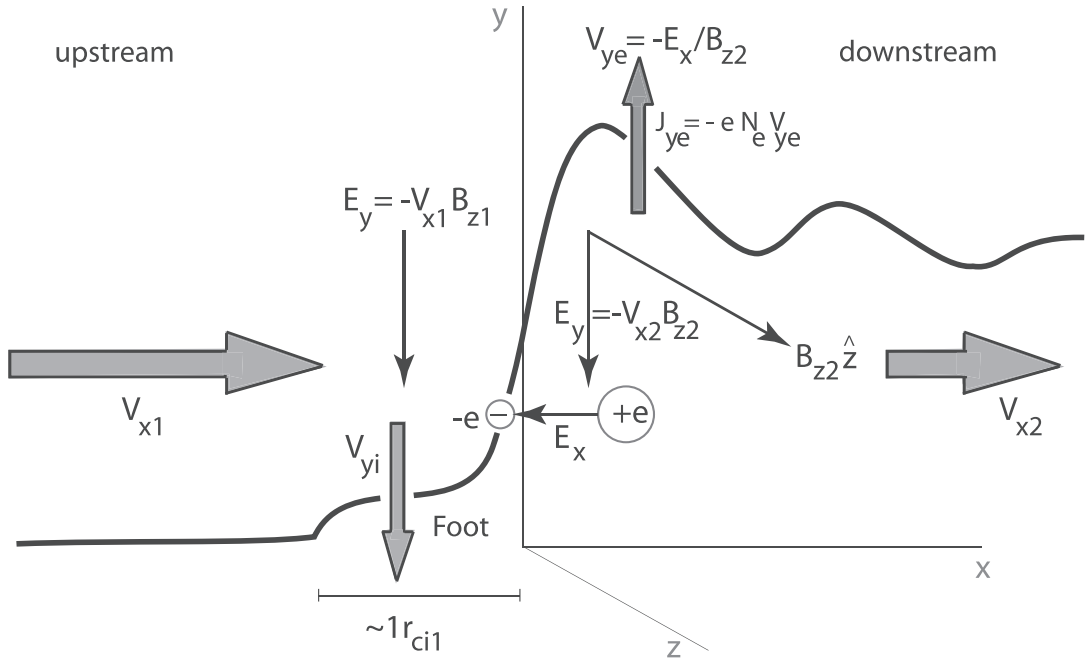


Figure 1.3: Geometry of an ideally perpendicular supercritical shock wave. Adapted from Balogh and Treumann [2013]

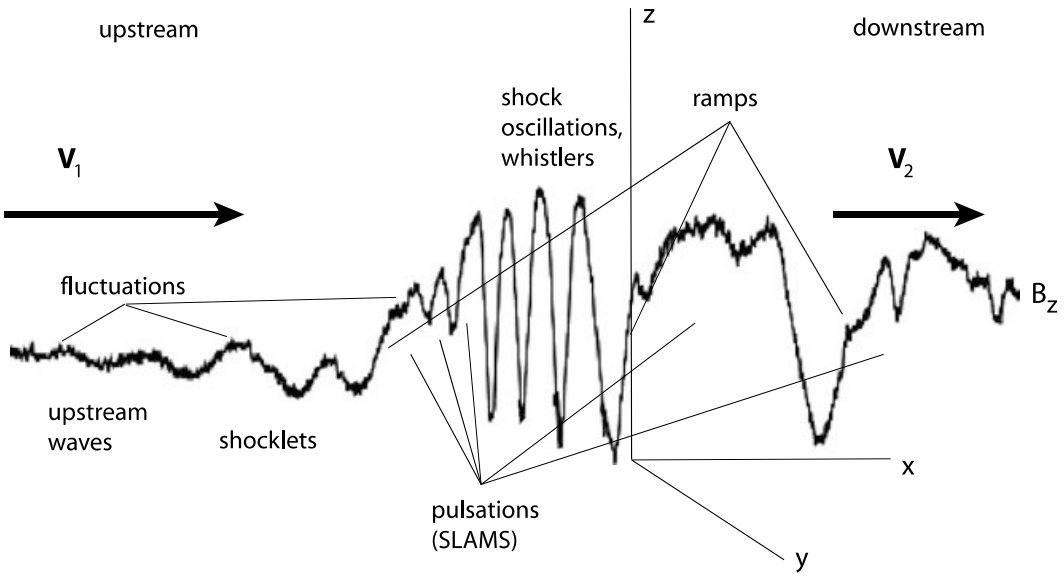


Figure 1.4: Schematic one-dimensional profile of a quasi-parallel supercritical shock wave. Adapted from Balogh and Treumann [2013].

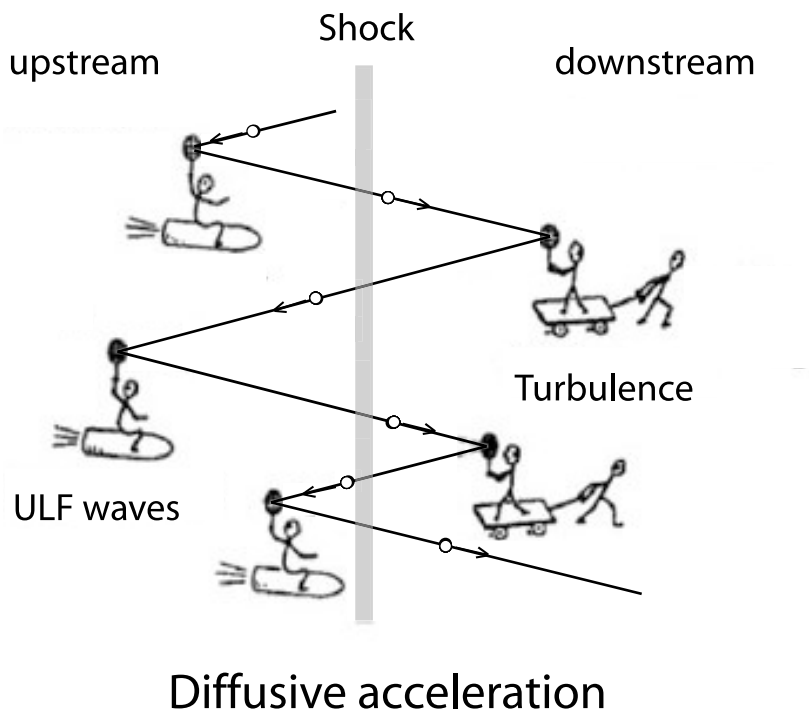


Figure 1.5: Illustration of the DSA originally sketched by M. Scholer.

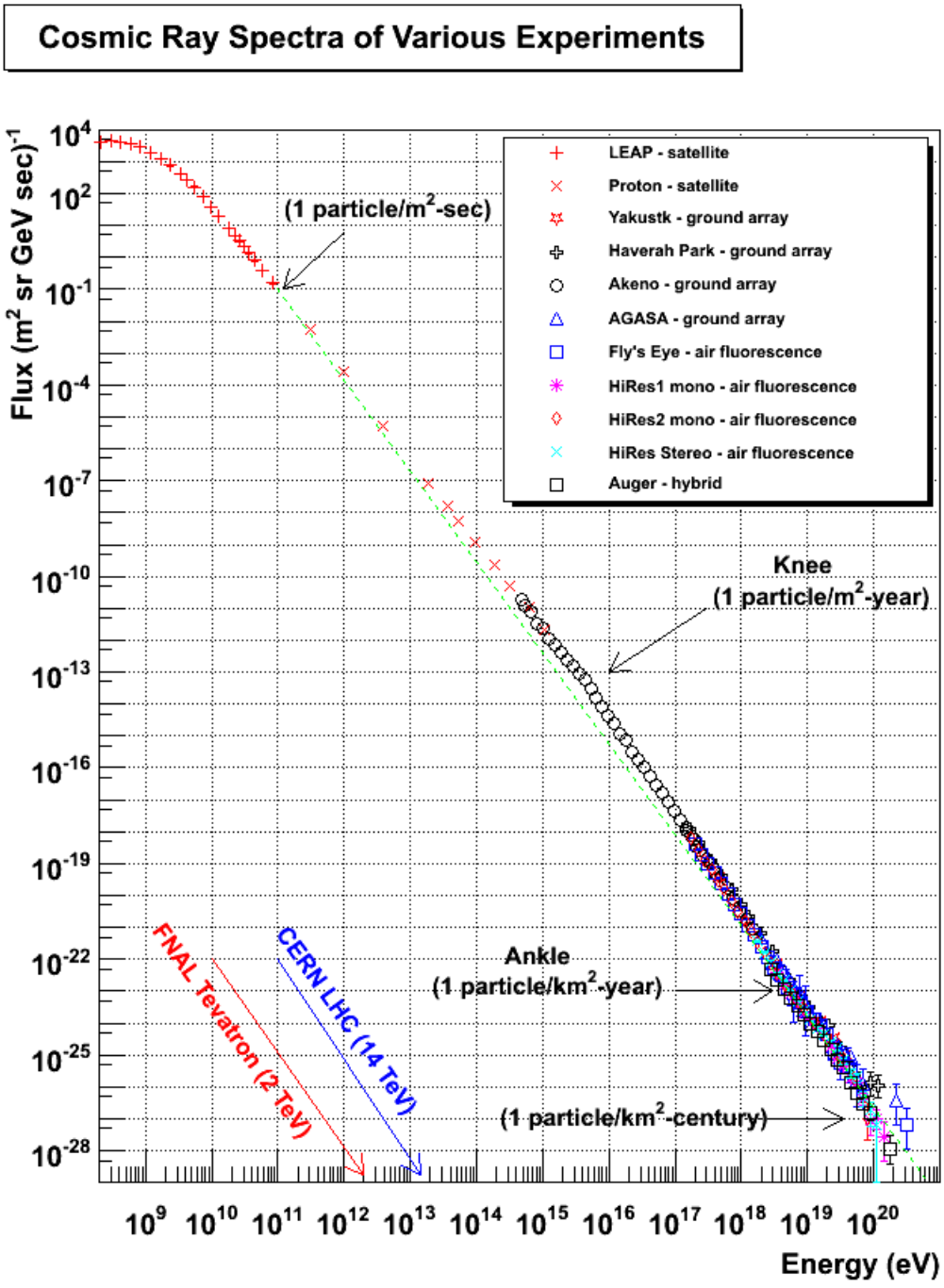


Figure 1.6: The energy spectram of CRs corrected by several instruments.

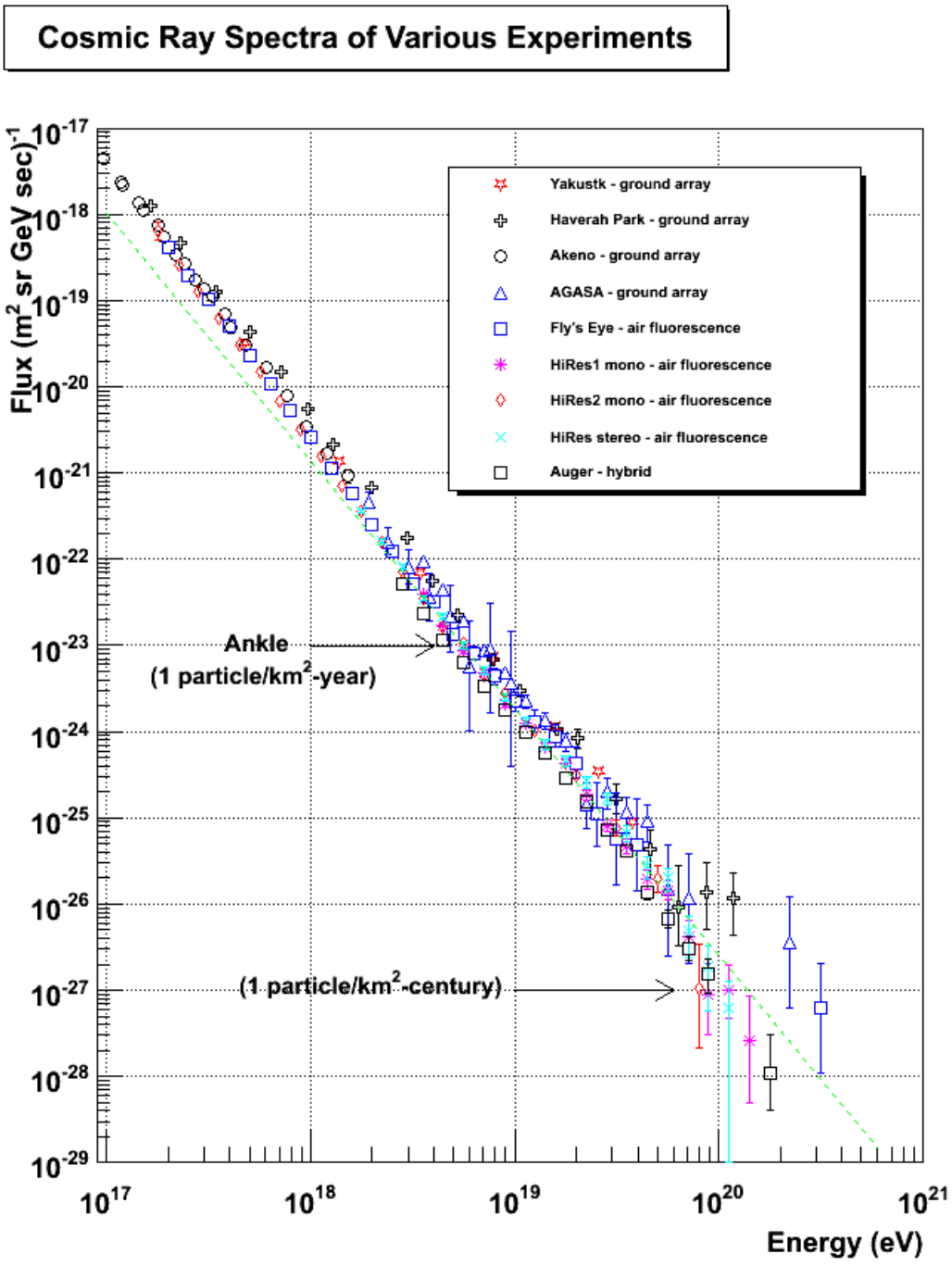


Figure 1.7: The energy spectram of CRs corrected by several instruments. The energy range is from 10^17 to 10^21.

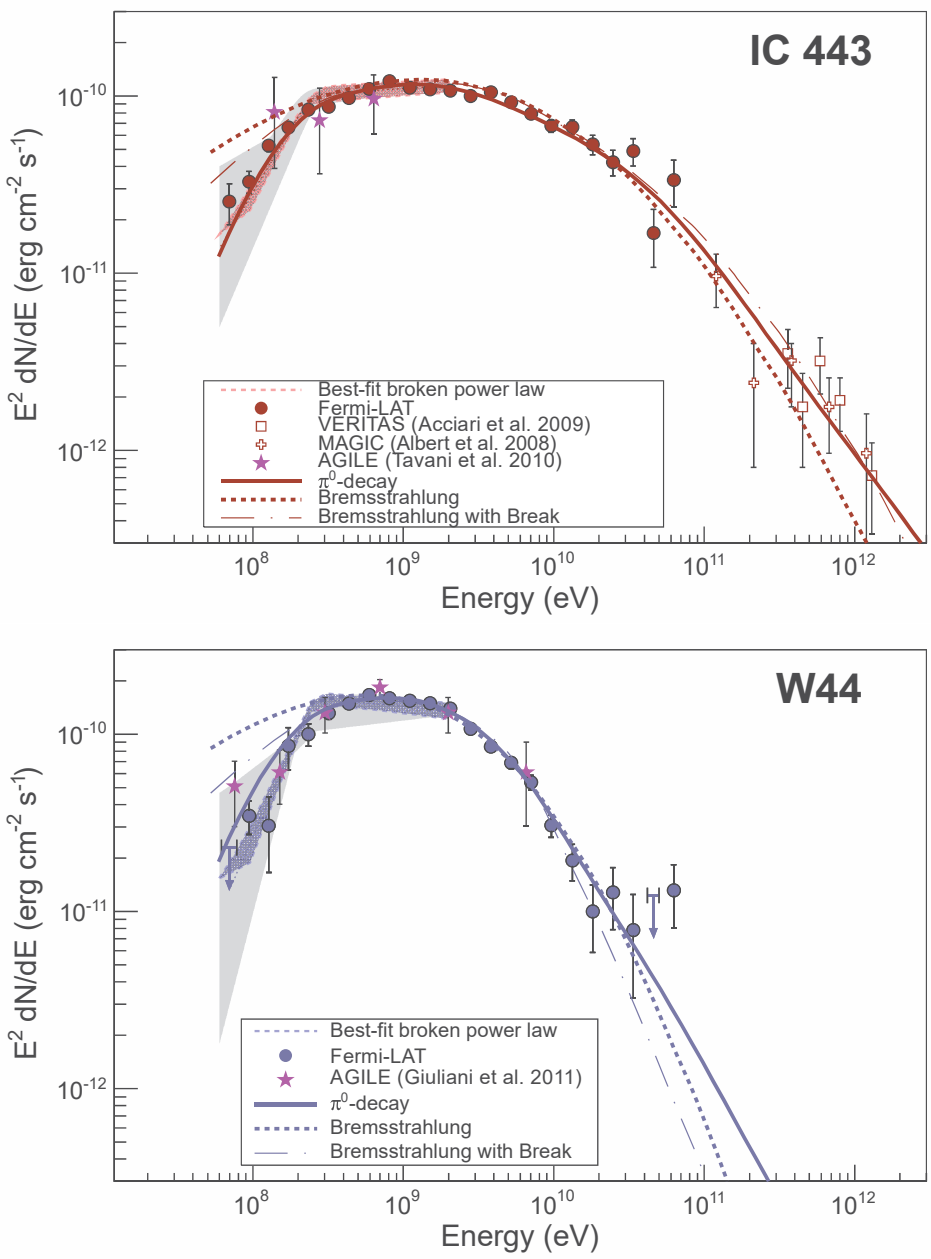


Figure 1.8: Top panel: Gamma-ray spectra of IC 443. Bottom panel: Gamma-ray spectra of W44. Both are measured with the *Fermi*-LAT. Adapted from Ackermann et al. [2013].

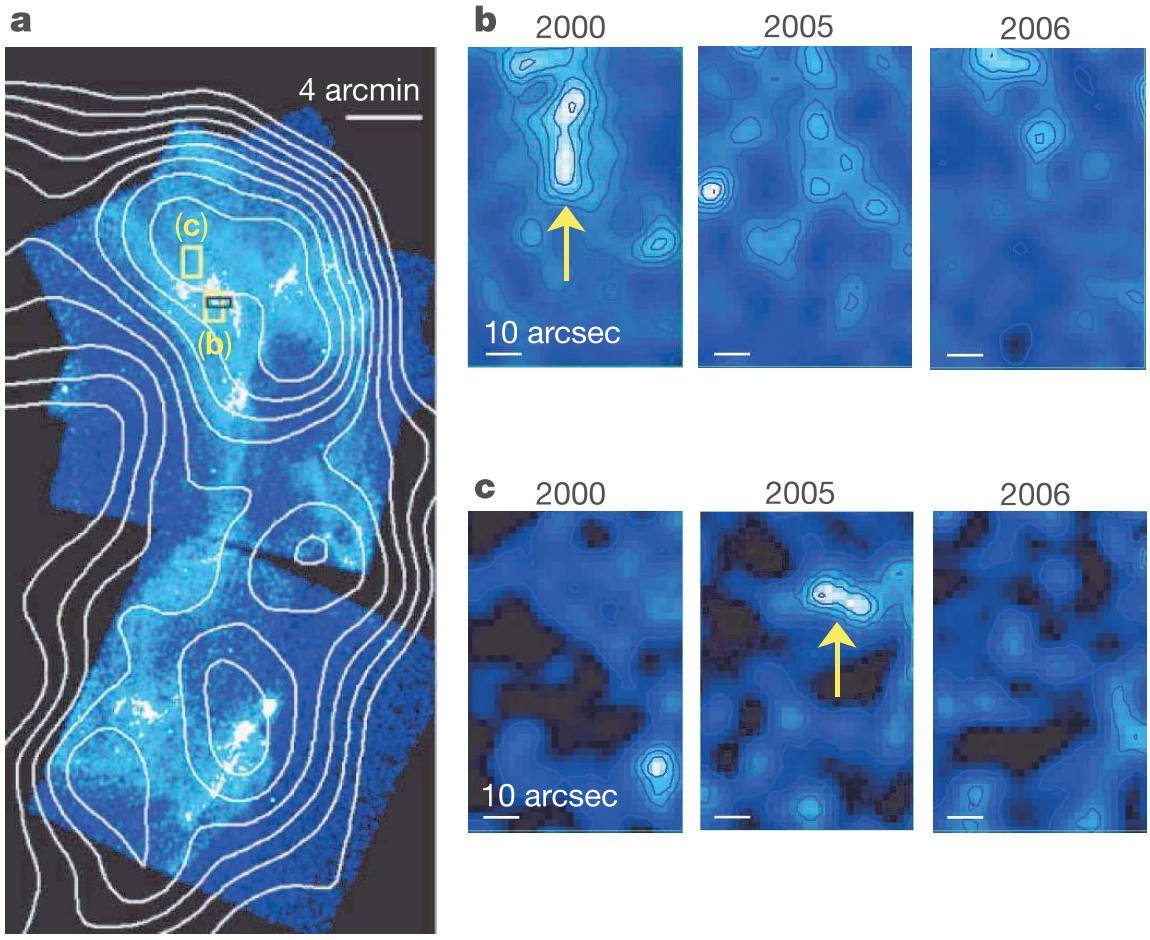


Figure 1.9: Chandra X-ray images of the western shell of SNR RX J1713.7-3946. Adapted from Uchiyama et al. [2007].

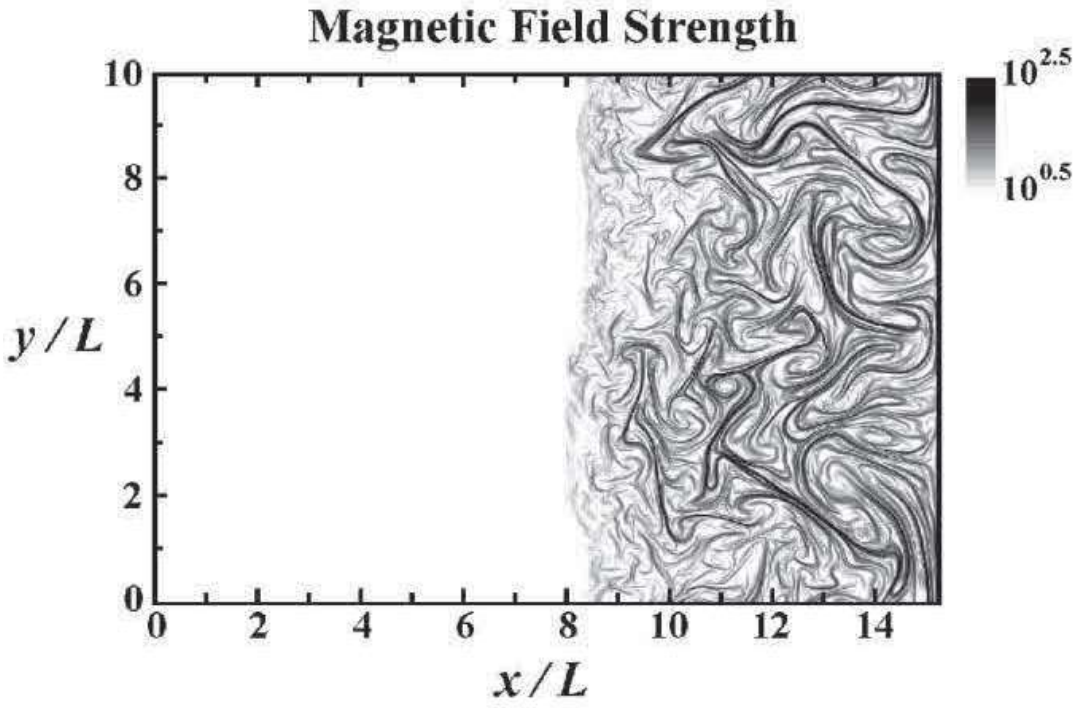


Figure 1.10: Shock-turbulence interaction: 2D plot of the magnitude of the magnetic fields. Adapted from Giacalone and Jokipii [2007].

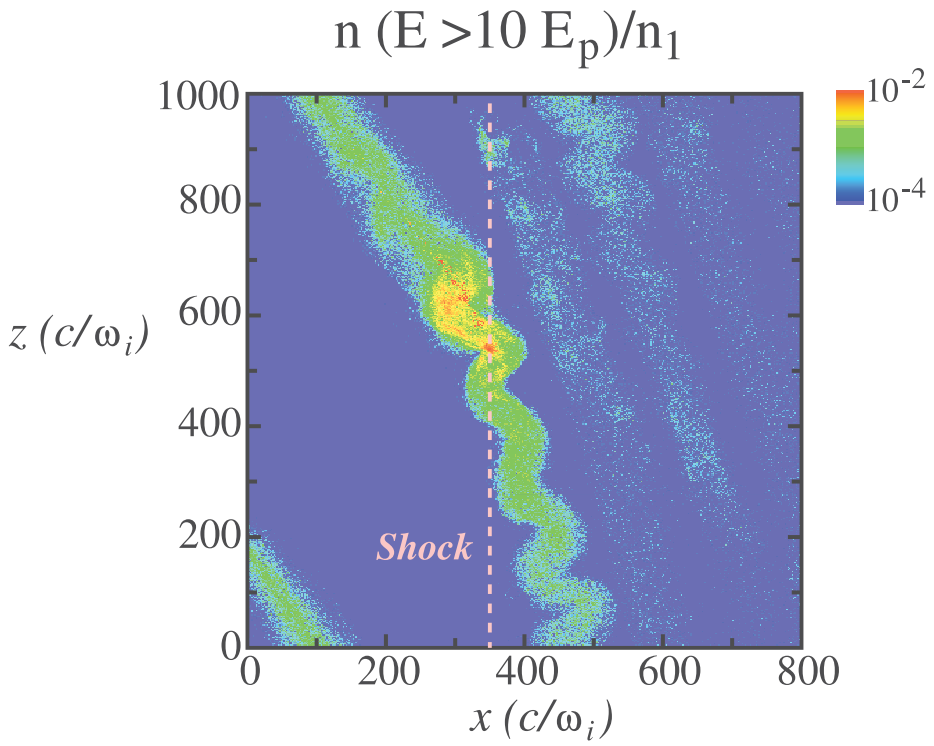


Figure 1.11: Shock-current sheets interaction: Two-dimensional color-coded representation of the number density of energetic particles whose energy is 10 times larger than the plasma ram energy. Adapted from Giacalone and Burgess [2010].

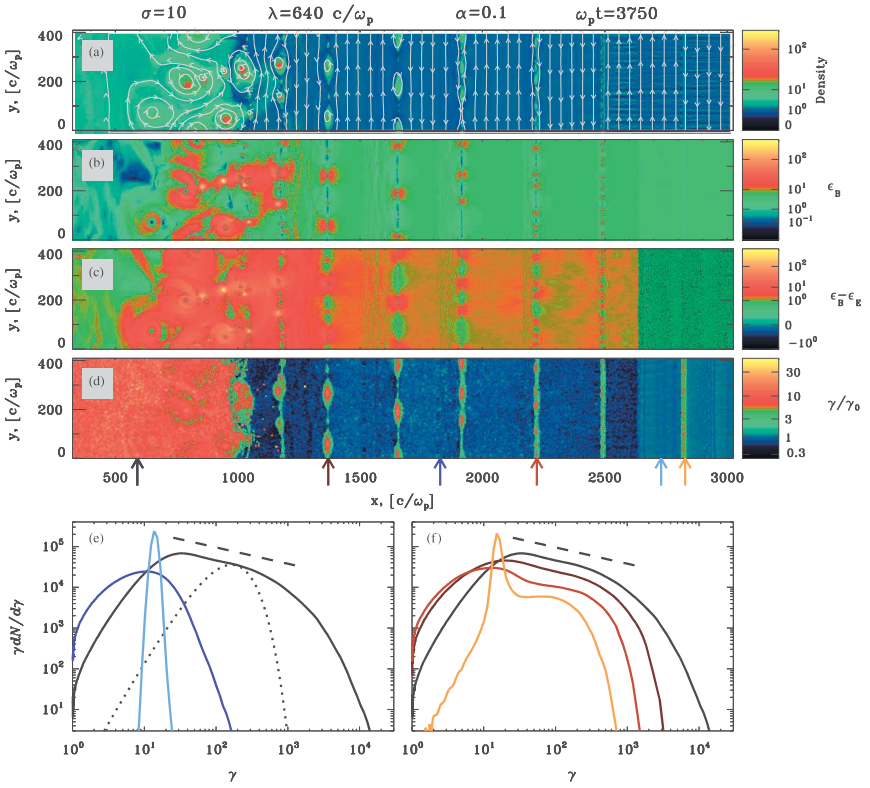


Figure 1.12: Shock-current sheets interaction: 2D full PIC simulation. Adapted from Sironi and Spitkovsky [2011].

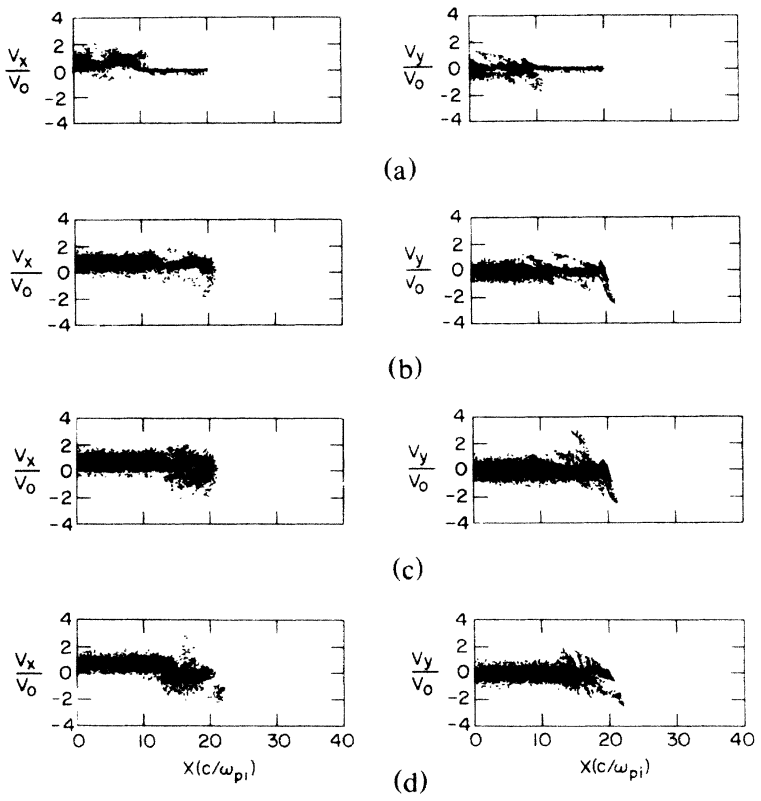


Figure 1.13: Shock-shock interaction: 1D hybrid simulation. Phase-space plot. Adapted from Cargill et al. [1986].

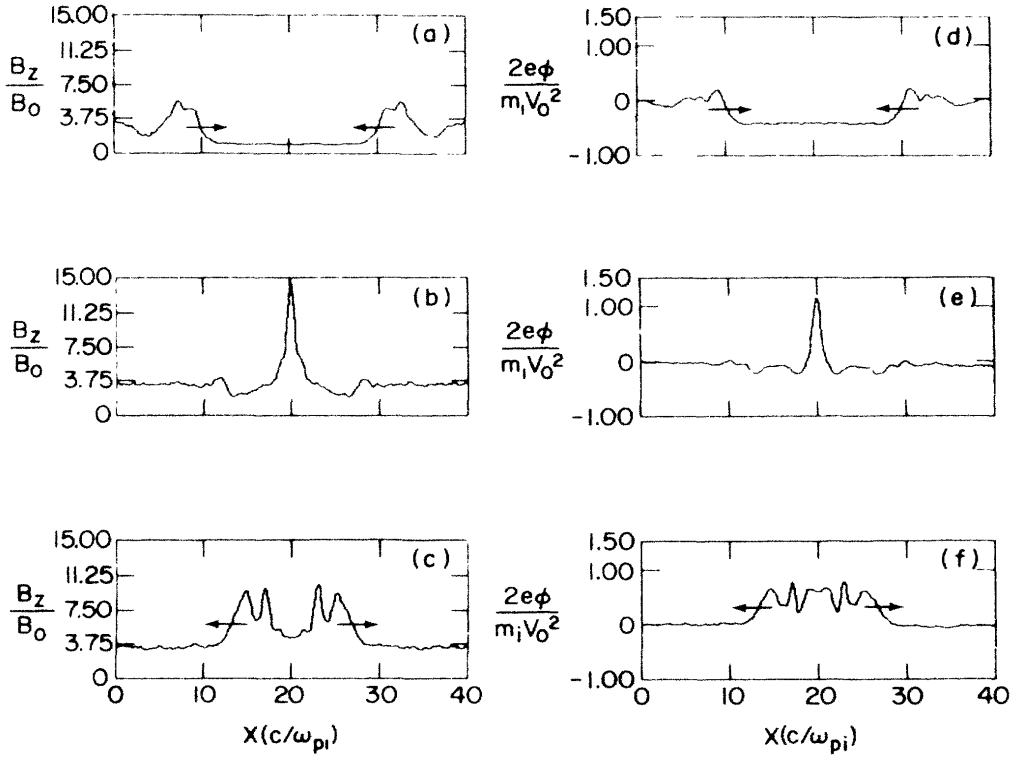


Figure 1.14: Shock-shock interaction: 1D hybrid simulation. The profile of the magnetic field B_z and the potential ϕ. Adapted from Cargill et al. [1986].

CHAPTER 2
TEST PARTICLE SIMULATION

Part of this chapter is published as: Diffusive shock acceleration of cosmic rays from two stationary shocks
Masaru Nakanotani, and Tohru Hada, Shuichi Matsukiyo, *Earth, Planets and Space*, Volume 70, Number 1, February 2018, doi: 10.1186/s40623-018-0799-3.

Here we discuss particle acceleration in two shock waves using Monte-Carlo simulation and the diffusion convection equation. Important points are that multiple shock waves can overcome the maximum acceleration rate of the strongest single shock and in this case we have to consider energy dependence for the diffusion coefficient.

2.1 Introduction

Particle acceleration in multiple shocks has been treated theoretically by Melrose and Pope [1993]. They considered a system where "seed" particles are initially given at the location of the shock waves are continuously accelerated by a sequence of identical shock waves. Furthermore, they concluded that the energy spectrum becomes $n(p) \propto p^{-1}$ for infinite number of shocks, where $n(p)$ is the density distribution function. The spectrum for dual shocks is harder than that of a single shock whose compression ratio is 4. Recently, Zhao and Li [2014] performed test particle simulations for a pair of parallel shocks approaching each other. They included magnetic turbulence and calculated the equation of motion and pitch angle diffusion of particles. Their calculations showed that the power-law spectrum index for a pair of shocks is harder than that of a single shock, and the maximum energy is greater than that of a single shock.

In this chapter, we account for accelerated particles from one shock traveling to the

other shock against a plasma flow; an effect that is not considered in Melrose and Pope [1993]. We discuss the particle acceleration in two shock waves by performing test particle simulations and evaluating the convection diffusion equation.

This chapter is organized as follows. In section 2, we describe our model and assumptions used in our test particle simulation and theoretical analysis. The results of the test particle simulations are presented in section 3. To explain the simulation results, we develop a theoretical analysis in section 4. In section 5, we discuss the breaking points of the double power-law type spectrum by examining the dependence of the break point energy on other parameters. Finally, a summary is provided in section 6.

2.2 Test Particle Simulation

Let us consider a system in which there are two hydrodynamic planar shocks, "Shock1" and "Shock2", located at $x = 0$ and $x = L$ in Cartesian coordinates, respectively (Fig.2.1). For simplicity, we ignore the background magnetic field. Because we consider this problem as one-dimensional, we do not have to include adiabatic decompression, which is treated in Melrose and Pope [1993]. The shocks are assumed to be infinitesimally thin, and both shock normals are pointing toward the x direction. The assumption of zero scale length of the shock transition layer is made due to its simplicity, but it may be violated when a shock precursor with a cosmic ray scattering length scale is generated in front of the shock [Drury and Voelk, 1981]. Here, we simply assume that the energy density of the cosmic rays is small enough.

We further assume that the cosmic ray speed is much faster than the shock speed, and that the time scale of particle acceleration is sufficiently shorter than the time scale for the two shocks to approach each other. Specifically, we assume that shocks are at rest and time stationary. The two shocks divide the entire space into three regions as in Fig.2.1: "Region 1" ($x < 0$), "Region 2" ($0 < x < L$) and "Region 3" ($L < x$), which correspond to upstream of the two shocks, downstream of Shock1 and upstream of Shock2, and downstream

of both shocks, respectively.

Next, $\mathbf{p}$ and $\mathbf{p}'$ are the cosmic ray momentum vectors defined in the shock rest and plasma rest frames, respectively. These are related through the Lorentz transformation using the local plasma flow velocity, $u(x)\mathbf{e}_x$, where $u(x) = u_i(= const.)$ for the three regions, $i = 1, 2, 3$, and $\mathbf{e}_x$ is the unit vector in the x direction. In the present model, the cosmic ray travels freely with a constant speed along a straight line for the time period, τ, until it collides with a scatterer, i.e., MHD turbulence, which is assumed to move with the local plasma flow.

Because cosmic ray energy is conserved in the plasma rest frame, the cosmic ray momentum after the collision can be written as, $\mathbf{p}'_a = p'\mathbf{e}_r$, where $p' = |\mathbf{p}'|$ is the magnitude of the momentum in the plasma rest frame, and $\mathbf{e}_r$ is a unit vector representing the momentum direction after the collision.

For simplicity, the scattering time, τ, is constant. One can specify τ according to some given probability distribution function, but within the context of the present study, the generalization for τ does not alter the results qualitatively, as long as the central limit theorem is satisfied for the convolution of the probability distribution function.

We also assume that cosmic ray scattering due to turbulence is isotropic in the plasma rest frame ($\mathbf{e}_r$ is chosen randomly in all the directions in three dimensions). This corresponds to the assumption of large-angle scattering, which may represent the scattering due to a strongly turbulent magnetic field, or an approximation of successive small-angle scattering, such as the pitch-angle scattering by small amplitude waves. The difference between the large-angle scattering and the pitch-angle scattering models are discussed in Naito and Takahara [1995]. We treat the motion of particles in electromagnetic fields as random.

First, we inject seed particles at Shock1 and Shock2. The initial particle momentums are all equal to p_0, but their directions are random. They then travel for τ and are scattered by turbulence, and a new momentum is computed after collision; they then travel again, and the cycle continues. After repeating this cycle for a certain length of time, we collect

particle data and compute the cosmic ray spectrum.

The thick solid line in the large panel shown in Fig.2.2 shows the result from the test particle simulation. Test particles are injected at both Shock1 and Shock2. Parameters used for this run are: $u_1 = 4$, $u_2 = 2$, $u_3 = 1$ (normalized to u_3), $L = 125$ (normalized to τu_3), $p_0 = |\mathbf{p}_0| = 7.5$ (normalized to $m_0 u_3$, where m_0 is the rest mass of the particle), and the number of particles used is 2×10^5.

The calculation time is $2 \times 10^4 \tau$ (normalized to tau). The horizontal axis is the logarithm of the cosmic ray momentum in the shock rest frame, p, and the vertical axis is the logarithm of the cosmic ray density distribution function, $n(p)$. Specifically, $n(x,p)\Delta p \Delta x$ corresponds to the number of particles with its position within the range $(x, x + \Delta x)$ and its momentum within the range $(p, p + \Delta p)$. In using these ranges, we ensure that the numerically obtained cosmic ray distribution is nearly isotropic. We collect all the particles in Region 3 to evaluate the distribution function. Because Region 3 corresponds to the downstream of Shock2 , $n(x,p)$ must be independent of x.

The thick solid line in the small panel in Fig.2.2 shows the result of the test particle simulation for one single shock. The conditions are same with the above simulation except for omitting Shock2 ($u_3 = 2$) and injecting particles only from Shock1. It is well known that the DSA process produces the power-law spectrum, $n(p) \sim p^{-\Gamma}$, with $\Gamma = (r + 2)/(r-1)$, where r is the shock compression ratio. For Shock1, $r = u_1/u_2 = 2$ and $\Gamma = 4$. We confirm that the spectrum obtained from the test particle simulation corresponds to the index from the theoretical analysis.

As shown in the large panel, the spectrum in the low energy regime ($0 < \log(p/p_0) < 0.78$) and the high energy regime ($0.78 < \log(p/p_0) < 2.5$) are approximated by power-law distributions with different indices. The low energy part is comprised of cosmic rays accelerated by one of the two shocks, and the high energy part is comprised of particles that travel long enough distances to interact with both shocks. For Shock1 and Shock2, $r = u_1/u_2 = u_2/u_3 = 2$ and $\Gamma = 4$; for the two shocks together the compression ratio is

$r = u_1/u_3 = 4$, which gives $\Gamma = 2$. These values explain the slope of the spectrum for the low and high energy regimes in Fig. 2.2.

2.3 Theoretical Analysis

In this section we describe a theoretical model based on the diffusion convection equation (e.g., Skilling [1975]). If we assume that the cosmic ray distribution is isotropic, its time evolution can be described by

$$\frac{\partial f}{\partial t} + u\frac{\partial f}{\partial x} - \frac{p}{3}\frac{du}{dx}\frac{\partial f}{\partial p} = \frac{\partial}{\partial x}(k\frac{\partial f}{\partial x}) + Q(x,p,t), \tag{2.1}$$

where $f(x,p,t)$ is the cosmic ray distribution function defined in the shock rest frame, $p = |\mathbf{p}|$, $u(x)$ is the plasma velocity, $k(x)$ is the spatial diffusion coefficient, and $Q(x,p,t)$ is a source term,

$$Q(x) = A_1\delta(x)\delta(p-p_0) + A_2\delta(x-L)\delta(p-p_0), \tag{2.2}$$

where A_1 and A_2 are constant. Within the three regions we defined before, we let $u(x) = u_i$ and $k(x) = k_i$ $(i = 1,2,3)$, with u_i and k_i constant. Then, the time stationary solution of (2.1) for each region can be written as

$$f_i(x,p) = \frac{C_i(p)}{u_i} + B_i(p)\exp(\frac{u_i x}{k_i}), \tag{2.3}$$

where $C_i(p)$ and $B_i(p)$ are arbitrary functions of p. From the boundary conditions at $x \to \pm\infty$ and continuity of $f_i(x,p)$ across the two shocks we find

$$C_1(p) = B_3(p) = 0 \ , \ \ B_1(p) = \frac{C_2(p)}{u_2} + B_2(p) \ , \ \ \frac{C_3(p)}{u_3} = \frac{C_2(p)}{u_2} + B_2(p)\exp(\frac{u_2 L}{k_2}). \tag{2.4}$$

Integration of (2.1) across the first shock at $x = 0$ yields

$$\left[-(k\frac{\partial f}{\partial x} + \frac{p}{3}\frac{\partial f}{\partial p}u)\right] = 0, \tag{2.5}$$

where the bracket denotes the difference across the shock. Substituting (2.3) into (2.5), we have

$$B_2 + \frac{p}{3}\frac{dB_2}{dp} + \frac{u_1}{u_1 - u_2}\frac{C_2}{u_2} + \frac{p}{3}\frac{d}{dp}(\frac{C_2}{u_2}) = \frac{A_1}{u_1 - u_2}\delta(p - p_0). \tag{2.6}$$

Similarly, across the second shock at $x = L$, we obtain

$$\left(\frac{u_2 B_2}{u_2 - u_3} + \frac{p}{3}\frac{dB_2}{dp} + \frac{pB_2}{3}\frac{d\xi}{dp}\right)e^{\xi} + \frac{p}{3}\frac{d}{dp}(\frac{C_2}{u_2}) = \frac{A_2}{u_2 - u_3}\delta(p - p_0), \tag{2.7}$$

where $\xi = u_2 L/k_2(p)$ is a dimensionless parameter representing the relative magnitude of the convection and diffusion for cosmic rays in Region 2. If $\xi >> 1$, convection is more dominant than diffusion, and cosmic rays starting from Shock2 cannot reach Shock1. Therefore, the two shocks are recognized as two well separated shocks for particles seeded from Shock2. On the other hand, if $\xi << 1$, diffusion is more dominant than convection, and the two shocks can essentially be viewed as a single shock with a velocity jump from u_1 to u_3.

The value of ξ depends on the momentum of the particle through the spatial diffusion coefficient,

$$k_2 =< \frac{(v_x\tau)^2}{2\tau} >= \frac{v^2\tau}{6} = \frac{\tau c^2 p^2}{6(m_0^2 c^2 + p^2)}, \tag{2.8}$$

where $<>$ denotes the ensemble average, and v_x is the x component of the velocity vector in three dimensions. Then (2.7) is re-written as

$$\left((\frac{u_2}{u_2 - u_3} - \frac{2\xi}{3\gamma^2})B_2 + \frac{p}{3}\frac{dB_2}{dp}\right)e^{\xi} + \frac{p}{3}\frac{d}{dp}(\frac{C_2}{u_2}) = \frac{A_2}{u_2 - u_3}\delta(p - p_0), \tag{2.9}$$

where $\gamma = \sqrt{1 + \frac{p^2}{m_0^2 c^2}}$.

Equations (2.6) and (2.9) are simultaneous differential equations for $B_2(p)$ and $C_2(p)$, and the solutions can be obtained numerically. Then, the distribution function is given as

$$n(p) = 4\pi p^2 f_3(p) = 4\pi p^2 \left\{ \frac{C_2(p)}{u_2} + B_2(p) \exp\left(\frac{u_2 L}{k_2}\right) \right\}. \tag{2.10}$$

For the DSA with a single shock, the cosmic ray spectrum does not depend on the diffusion coefficient, which is not the case for the present problem. The dotted line in Fig. 2.2 shows (2.10), in which k_2 is given by (2.8) with $p = p_0$ (p_0 is the initial momentum). In this case, k_2 is a constant. All other parameters are chosen according to the test particle simulation run.

The result does not agree with the simulation. In particular, the model does not have a double power-law distribution produced by the test particle simulation.

The thin solid line in Fig. 2.2 shows (2.9) with the p dependence correctly kept in the definition of k_2 in (2.8). Now, the result agrees well with the test particle simulation. In particular, the breaking of the power spectrum is included.

To seek an asymptotic solution for (2.6) and (2.9), let us write

$$C_2(p) = \alpha p^{-s} \quad ; B_2(p) = \beta p^{-s}. \tag{2.11}$$

After substituting the above into (2.6) and (2.9), and seeking a non-trivial solution for α and β, we find

$$s(s-3) = (s-s_1)(s-s_2)e^{\xi}, \tag{2.12}$$

where $s_1 = 3u_1/(u_1 - u_2)$ and $s_2 = 3u_2/(u_2 - u_3)$ are the power-law indices of the density distribution function due to the DSA by Shock1 and Shock2, respectively.

In this calculation, we have neglected the second term in (2.9) for simplicity. When ξ is very large, (2.12) gives two roots, $s = s_1$ and $s = s_2$, suggesting that the two shocks are independent. The DSA calculated with the two shocks separately produces distributions

specified by their compression ratios. In contrast, in the limit of $\xi \to 0$, (2.12) becomes a linear equation for s, and the solution is

$$s = \frac{s_1 s_2}{s_1 + s_2 - 3} = \frac{3u_1}{u_1 - u_3}. \tag{2.13}$$

As expected, the spectrum index from the DSA due to the two shocks combined is obtained. The equation (2.13) implies that the spectrum of the two shocks can be harder than the strongest single shock. If there are two strong shocks with compression ratios of 4, equation (2.13) becomes 3.2. When considering a series of multiple shocks, the maximum spectrum index can be obtained from equation (2.13), applying the upstream flow of the first shock as u_1 and the downstream flow of the last shock as u_3. It is easily seen that the maximum index approaches 3 as the number of shocks increases because the downstream flow of the last shock approaches 0, in agreement with Melrose and Pope [1993].

2.4 Discussion

We have seen that the diffusion convection equation well explains the test particle simulation results presented in the previous section. In this section, we discuss the dependence of spectrum breaking using equations (2.6) and (2.9).

Below we discuss determining the momentum at the breaking point, p_b, by examining its dependence on shock parameters, L, u_1, u_2 and u_3. Fig. 2.3(a) shows p_b as a function of L (the crosses), keeping other parameters unchanged at $u_1 = 4$, $u_2 = 2$ and $u_3 = 1$. This plot is made by numerically evaluating the first derivative of $\log n(p)$ with respect to $\log p$. We define the break point as the point at which the first derivative has the minimum value. Fig. 2.3(b) suggests that p_b becomes larger as L increases.This relationship is due to the increase in L when a particle starting from Shock2 must travel a long distance to reach Shock1.

Fig. 2.3(b) shows p_b as u_2 (circles) varies with parameters $L = 125$, $u_1 = 4$, and

$u_3 = 1$. When u_2 increases, p_b also increases, because a particle starting from Shock2 must overcome the fast convection of the background flow to reach Shock1.

The break point is not strongly affected by variations in u_1 and u_3 (not shown here) because u_1 and u_3 do not influence the particle transport between Shock1 and Shock2.

We also estimate the value of p_b by comparing the diffusion and convection in Region 2. Suppose a particle with momentum p, located at Shock2, starts a random walk at time $t = 0$ in a convecting flow with a speed u_2. The motion of the particle may then be given as a superposition of the random walk and convection,

$$\lambda(t) = \sqrt{6k_2 t} - u_2 t, \tag{2.14}$$

where λ is the travel distance along the x-direction measured from the location of Shock2 at $x = L$. Because k_2 is an increasing function of the particle momentum p, faster particles can travel longer distances compared with slower particles. Moreover, due to convection, there is a maximum distance a particle can travel, $\lambda_{max} = 3k_2/2u_2$. We estimate that the momentum at which $\lambda_{max} = L$ gives p_b. Namely, particles with momentum larger than p_b can travel from one shock to the other, potentially accelerating from both shocks. From this argument, we estimate

$$\frac{p_b}{m_0 u_3} = \sqrt{\frac{\delta}{1 - \delta(\frac{u_3}{c})^2}}, \tag{2.15}$$

where $\delta = 4(L/\tau u_3)(u_2/u_3)$ and c is the speed of light. In Fig. 2.3 we plot (2.15) as the solid line for L (a) and the dotted line for u_2 (b). This model well explains the functional dependence of p_b on L and u_2. This dependence of p_b on L becomes different between simulation and theoretical results for large L because we implicitly assume that the distribution function can spread out over the distance λ_{max}, which a particle can reach when we consider the time stationary solution (4).

The spatial diffusion coefficient approaches $\tau c^2/6$ for highly relativistic particles. In this case, λ_{max} is written as $(c/4u_2)\tau c$. Therefore, considering the time stationary solution,

the condition $L << (c/4u_2)\tau c$ should be applied.

2.5 Summary

In summary, we examined the DSA process in a system including two shocks. We assume that an acceleration time scale in a shock is much less than the approaching time scale of the two shocks. These two shocks can be treated as stationary under this assumption. Although we have to consider finite acceleration time for a more realist case, which means two shocks moving at different speeds, we believe that it does not change the result significantly.

Test particle simulations are performed, and a double power-law type spectrum is obtained. A simple model based on the diffusion convection equation explains the result well. In the model, it is important to include the momentum dependence on the spatial diffusion coefficient, unlike the DSA model with a single shock.

We discussed the dependence of the break point, p_b, on other shock parameters, and showed that the value of p_b can be estimated by balancing the convection and diffusion in a region between the two shocks. Our results indicate that an acceleration in two shocks is more efficient than a single shock, which is consistent with previous results.

The DSA in a two shock system is similar to the DSA from cosmic ray mediated shocks, in that the background flow velocity difference used to accelerate particles, depends on particle energy, which forms the double power-law spectrum. Similarly, spectral hardening has been observed at solar flare termination shocks [Li et al., 2013, Kong et al., 2013]. In these previous studies, the finite thickness of the termination shock was considered, and it was concluded that spectral hardening occurs because high energy electrons can see the full width, while low energy particles accelerate for only part of the shock width.

Figures

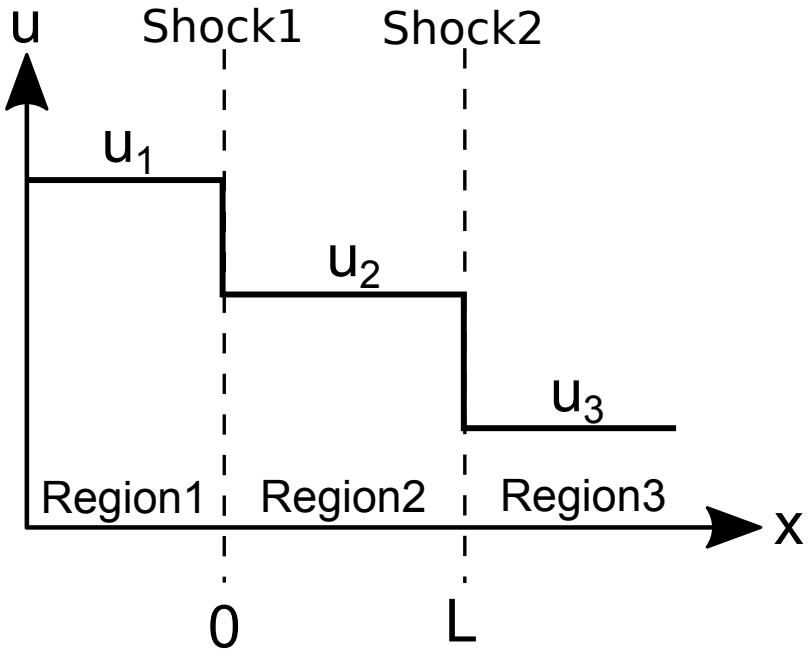


Figure 2.1: Schematic showing shock positions, regions, and flow speeds.

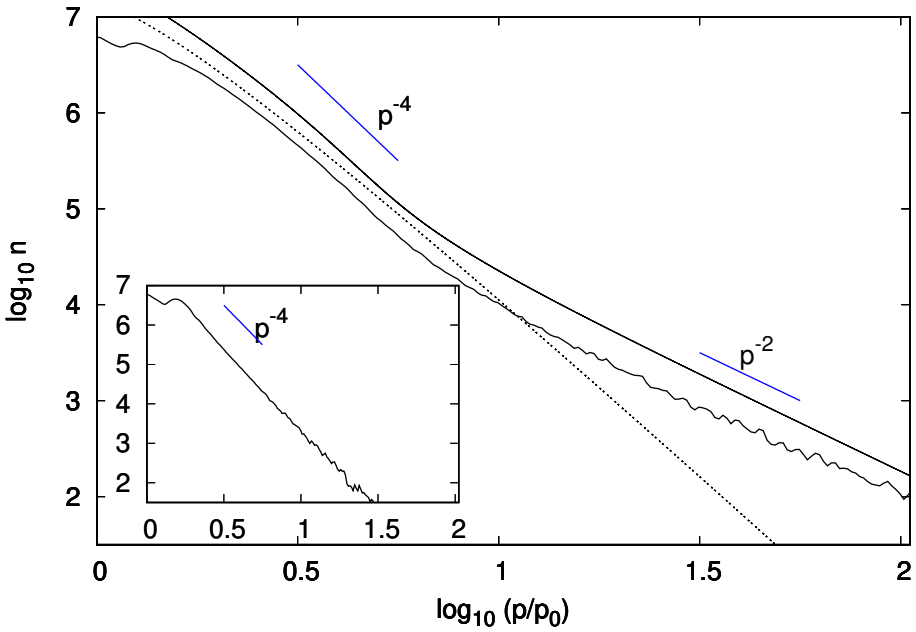


Figure 2.2: Large panel: Comparison of density distribution obtained from the test particle simulation for two shocks (thick solid line), theoretical model based on the diffusion convection equation with constant diffusion coefficient (dotted line), and the same model that takes into account the dependence of the diffusion coefficient on the cosmic ray energy (thin solid line). The two blue lines with indices -4 and -2 are indicated for reference. Test particles are injected at both "Shock1" and "Shock2". Small panel: density distribution obtained by the test particle simulation for one single shock.

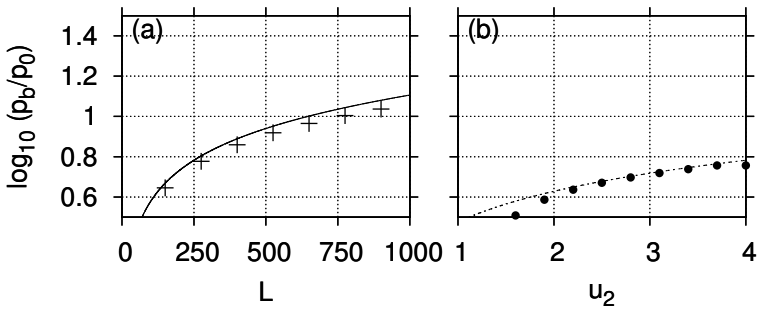


Figure 2.3: The breaking point p_b as a function of L (crosses) and u_2 (circles), numerically evaluated using the first derivative of $\log n(p)$ with respect to $\log p$. Solid lines are the equation (2.15).

CHAPTER 3
1D FULL PIC SIMULATION

3.1 Methodology

In full PIC simulation, electrons and ions are treated as super-particles moving in the simulation box, while charge density, current density, and electromagnetic fields are only defined on spatial grids. The charge density and the current density are calculated from the positions and the velocities of the super-particles. Then, the electromagnetic fields are obtained by solving Maxwell equations. Updated electromagnetic fields are need to calculate motions of super-particles. This process is repeated many times until the end of the simulation. More detailed information is described in Appendix.

For a single shock simulation, the so-called injection method is often used to produce a shock wave. In 1D simulation upstream plasma is continuously injected from one boundary. The injected plasma is reflected at the other boundary which is considered as a rigid wall. The reflected plasma and the incoming plasma interact with each other and a shock wave is created. This shock wave propagates toward the injection boundary. Because the downstream plasma is at rest, the simulation frame is the downstream-rest frame.

Two colliding shocks are produced in the following way. Initially, we fill a homogeneous magnetized plasma at rest having a Maxwellian distribution function for both electrons and ions in a simulation system. Two boundaries at the both end of the simulation box are rigid walls at which particles and waves are specularly reflected. By moving the walls inward with constant speeds, two shocks are formed through the interaction between the background and the reflected plasmas. Hereafter, we refer the shock propagating from right (left) to left (right) as "Shock 1 (Shock 2)". Shock 1 and Shock 2 gradually approach with each other and collide head-on. In this configuration, the simulation frame is the upstream

rest frame before that the two shocks collide. Because the speeds of the two walls are the same in magnitude here, the two shocks are essentially symmetric.

The background (or initial upstream) magnetic field is given as $\mathbf{B_0} = B_0(\cos\theta_{Bn}, 0, \sin\theta_{Bn})$, where B_0 is the strength and θ_{Bn} is the shock angle defined as the angle between the magnetic field and the x-axis (shock normal). The simulation parameters used are listed in Table 3.1. Here, M_A is the Mach number defined by v_{sh}/v_A where v_{sh} and v_A are the shock speed and the Alfvèn speed and m_i/m_e is the ratio of ion mass to electron mass. The parameter ppc means the number of particles in a cell. For all runs, $\beta_{i,e} = 0.5$, the ratio of electron plasma to cyclotron frequencies $\omega_{pe}/\omega_{ce} = 10$, the time resolution is $\Delta t = 0.05\omega_{pe}^{-1}$ and the size of a spatial grid $\Delta x = 0.05(c/\omega_{pe}) = \lambda_D$. Here, $\beta_{i,e} = 8\pi n_0 k_B T_{i,e}/B_0^2$, $\omega_{pe} = \sqrt{4\pi n_0 e^2/m_e}$ and $\omega_{ce} = eB_0/m_e c$, where e is the elementary charge, c is the speed of light, n_0 is the background ion and electron density, $T_{i,e}$ is the ion and electron temperature and k_B is the Boltzmann constant, and λ_D is the Debye length, respectively.

Table 3.1: Simulation parameters

Run #	M_A	θ_{Bn}	m_i/m_e	ppc
Run A	7.6	90°	25	100
Run B	13.6	60°	100	320
Run C	13.2	30°	100	320

3.2 Run A: Perpendicular Shock Waves

Here we discuss the collision of two symmetrical perpendicular shocks. We reproduce two perpendicular shocks with the same parameters of Cargill et al. [1986]. We confirm similar shock structures and ion acceleration process to the results obtained from hybrid simulations by Cargill et al. [1986]. The evolution of the shock waves corresponds well with the predictions from MHD equations.

3.2.1 Single Shock

First, let us discuss the structure of a single perpendicular shock. A remarkable feature of a super-critical perpendicular shocks is ion reflection. Here, we give an example of a single shock wave whose Mach number is 7.6, ion and electron beta are both 0.5, and shock angle is 90°, respectively. These parameters are the same with the hybrid simulation done in Cargill et al. [1986]. In this simulation, the ion to electron mass ratio is 25. This shock wave is created by the injection method in the downstream rest frame. Fig. 3.3 shows the time-space evolution of the magnetic field, B_z. The shock speed is estimated with $-0.152c$. Since the upstream Alfvén speed is $0.02c$, the Mach number is 7.6.

Fig. 3.2 plots density, pressure, electric fields E_y and E_z and magnetic fields B_y and B_z from the top to the bottom. The density is normalized to its upstream value, n_0, the pressure to upstream magnetic pressure, $B_0^2/8\pi$, and the electromagnetic fields to the upstream magnetic field, B_0, respectively. It is noted that because this is a 1D simulation, B_x is constant and 0 in this case. From the Rankine-Hugoniot relation, the downstream values of density, pressure and B_z are 2.8, 8.6, and 2.8, respectively. These values are indicated as dashed red lines in the figure. We can see that the shock front is located at around $1820c/\omega_{pe}$. The downstream values well coincide with the predictions from the Rankine-Hugoniot relation except for the transition region.

Fig. 3.1 shows electron (the left panels) and ion (the right panels) phase space density for the x, y, and z component of the velocity from the top to the bottom at certain time. From the top, vertical axis denotes v_x, v_y, and v_z, respectively. The motion in the z-direction of electrons and ions are decoupled from the other direction because of the exact perpendicular geometry. We can see the foot, ramp, and overshoot region around $1800c/\omega_{pe}$. These are due to the ions reflected at the shock ramp by the shock potential [Hada et al., 2003]. The viscosity provided by the reflected ions leads to sufficient dissipation of the flow energy of the incoming plasma.

As we have seen, ion reflection plays an important role for a super-critical perpendic-

ular shock wave. The transition layer is confined within roughly an ion gyro-radius and there is no noticeable feature upstream. Therefore, when we consider a collision of two perpendicular shock waves, it is expected that the interaction time is about only one ion gyro-period at the collision.

3.2.2 Shock-Shock Interaction

We discuss what happens when two identical shocks collide. Fig. 3.5 shows the profile of the magnetic field B_z (a) before, (b) at, and (c) after the collision, respectively. Before the collision, we can see that two shocks propagate inward. At the collision, the magnetic field is piled up at the collision site ($\sim 11B_0$)). It is roughly the sum of the overshoot magnetic field of the two original shocks. After the collision, the two shocks propagate outward with a constant speed. These two shock waves propagate in turbulent magnetic fields.

The values after the collision are consistent with the predictions from MHD. Fig. 3.6 shows the time-space evolution of the magnetic field B_z. It is clear that two shocks collide and separate after the collision. While the shock speed before the collision is about $7.6v_A$, its speed after the collision is about $5.3v_A$. Fig. 3.7 indicates the profile of the density and pressure after the collision. Using the discussion of Kato [1959], we can obtain the values downstream after the collision. It is noted that the discussion could be only applied for a perpendicular shock collision. They are described as $r = 1.95$, $B_{z2} = 5.47B_0$, $\beta = 10.8$, and the shock speed $v_{s2} = 5.17v_A$ as indicated dashed lines. These lines are well-fitted with simulation results.

Next, we explain a particle acceleration due to the collision of the two shocks. Fig. 3.4 shows the phase space density of electrons and ions (a) before, (b) at, and (c) after the collision. Before the collision, the upstream plasma is not modified and the two shock waves are completely separated. At the collision, some particles are accelerated at the collision site. After the collision, two shock waves propagate in a turbulent and heated plasma. Fig. 3.8 expresses the energy spectrum of electrons and ions at the corresponding

three times. We integrate particles in the range $1000 < x/(c/\omega_{pe}) < 2000$. Some ions and electrons are accelerated and finally the maximum energy of ions reaches up to 12 times larger than the bulk energy before the collision.

The ion acceleration occurs with multi-steps. Fig. 3.9 shows in the left panel the time-space evolution of the magnetic field B_z and the trajectory of an well-accelerated ion. The right panel is the time evolution of the ion energy. From these panels, we can understand that the ion acceleration takes place light before and after the collision. Fig. 3.10 depicts how the ion is accelerated. The red, black, and blue lines are the trajectory of the ion, magnetic field B_z, and motional electric field E_y. At the first time (a), the ion is reflected at the shock front due to the shock potential. It then gyrates and passes through the downstream of the other shock and gain energy from the motional electric field in the panel (b). Moreover, it come back to the downstream of the first encountered shock and attains energy again (c). As we saw, the ion acceleration is taken place with multi-steps.

On the other hand, most of all electrons are just heated after the collision glancing the panel (c) in Fig. 3.8. There would be, however, a possibility that some of electrons are accelerated. Fig. 3.11 shows the time-space evolution of the magnetic field B_z and the trajectory of a representative electron. The right panel is the time evolution of the electron. We can see two kinds of acceleration for this electron. The first results from the first adiabatic invariance ($\mu \equiv v_\perp^2/2B_z$ where $v_\perp$ is the velocity perpendicular to the magnetic field). When the magnetic field is amplified, the electron energy also increases. The second comes from turbulence produced after the collision ($t > 1400/\omega_{pe}$). In this case, in spite of that the magnetic field stays constant, the electron energy gradually increases. Since these turbulence might have almost the same electron Larmor radius of this electron, the electron is accelerated through the wave-particle interaction [Achterberg, 1979, Lynn et al., 2013, Ostrowski and Siemieniec-Ozibło, 1997]. It is worth to note that electrons are not accelerated like ions described above because electrons do not have Larmor radius as large as ions due to the mass ratio.

Figures

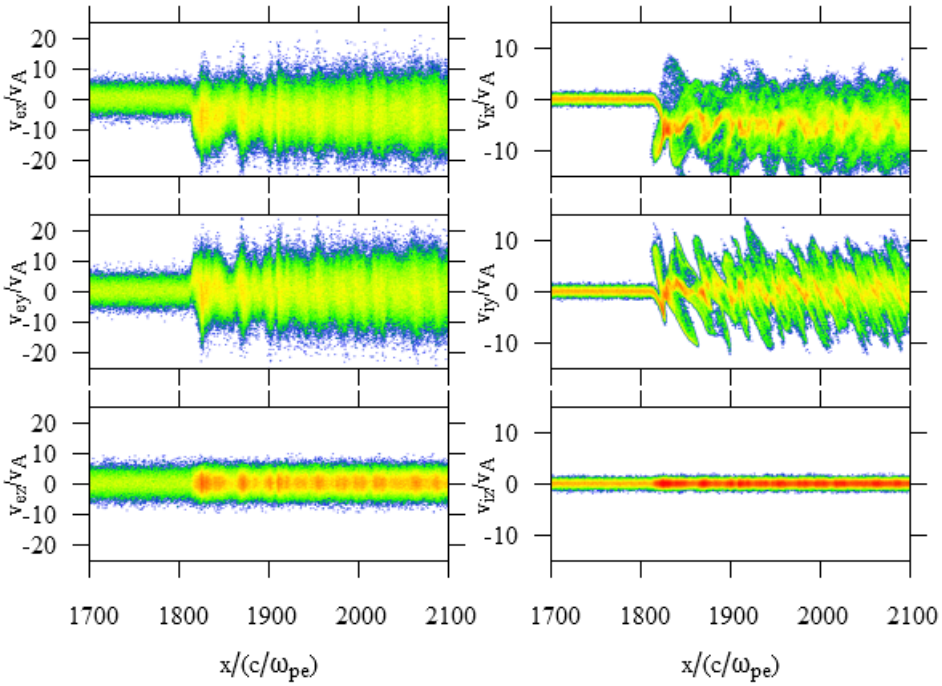


Figure 3.1: Left panels: electron phase space density of v_x, v_y, and v_z from the top to the bottom. Right panels: ion phase space density of v_x, v_y, and v_z from the top to the bottom.

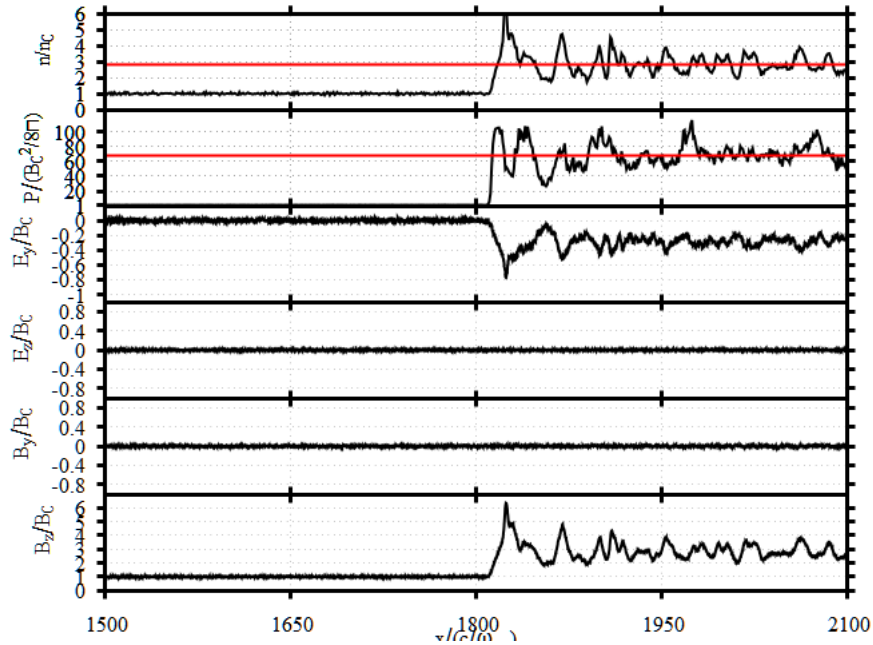


Figure 3.2: The plasma density, plasma beta, electric field E_y, E_z, magnetic field B_y, and B_z from the top to the bottom.

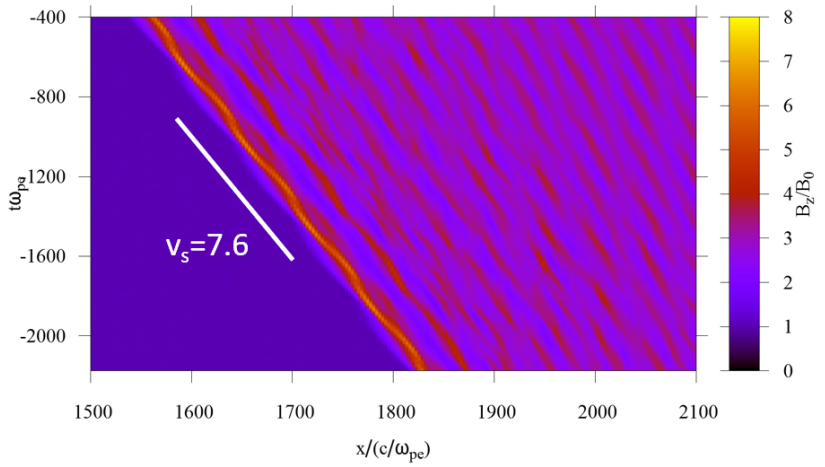


Figure 3.3: The time-space evolution of the magnetic field B_z.

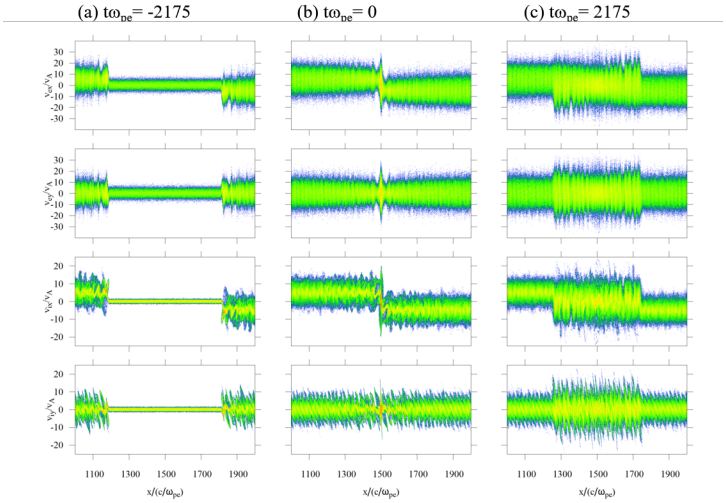


Figure 3.4: Electron and ion phase space density of v_x and v_y for three times ($t\omega_{pe} = -2175, t\omega_{pe} = 0$ and $t\omega_{pe} = 2175$).

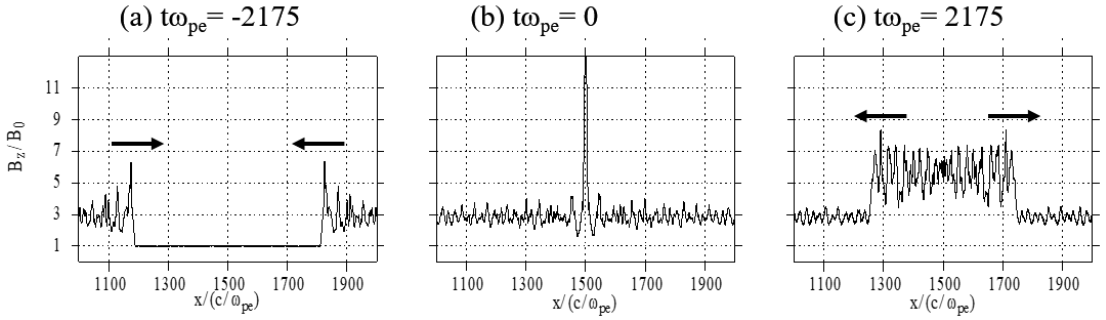


Figure 3.5: The profile of the magnetic field B_z fro three times ($t\omega_{pe} = -2175, t\omega_{pe} = 0$ and $t\omega_{pe} = 2175$).

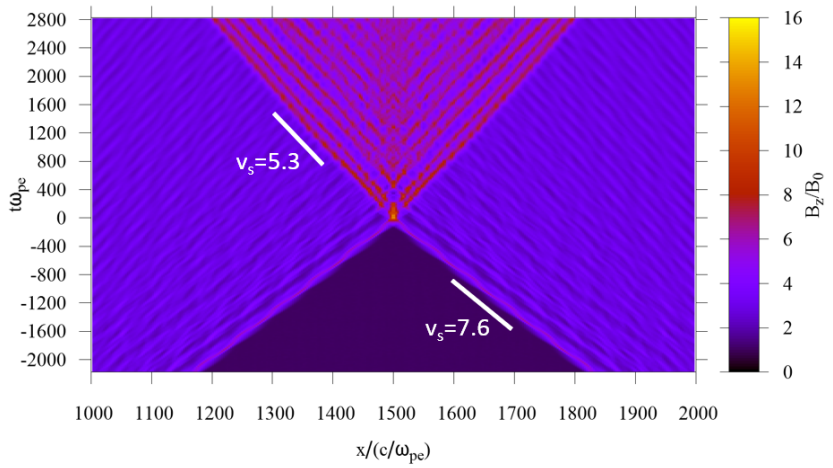


Figure 3.6: The time-space evolution of the magnetic field B_z.

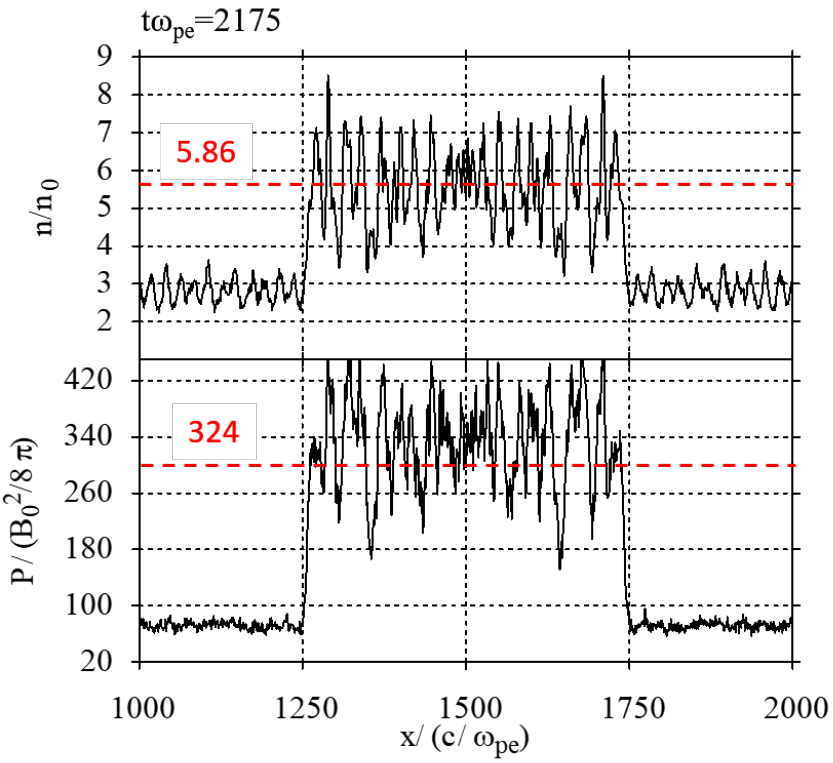


Figure 3.7: The profile of the plasma and pressure at $t\omega_{pe} = 2175$.

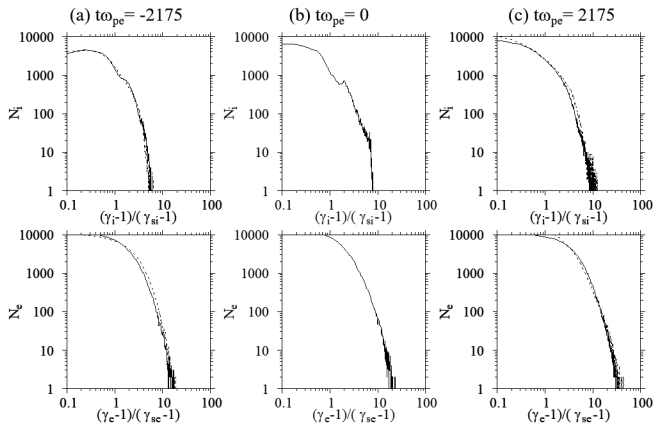


Figure 3.8: Top panels: ion energy spectrum for three times ($t\omega_{pe} = -2175, t\omega_{pe} = 0$ and $t\omega_{pe} = 2175$). Bottom panels: electron energy spectrum for three times ($t\omega_{pe} = -2175, t\omega_{pe} = 0$ and $t\omega_{pe} = 2175$).

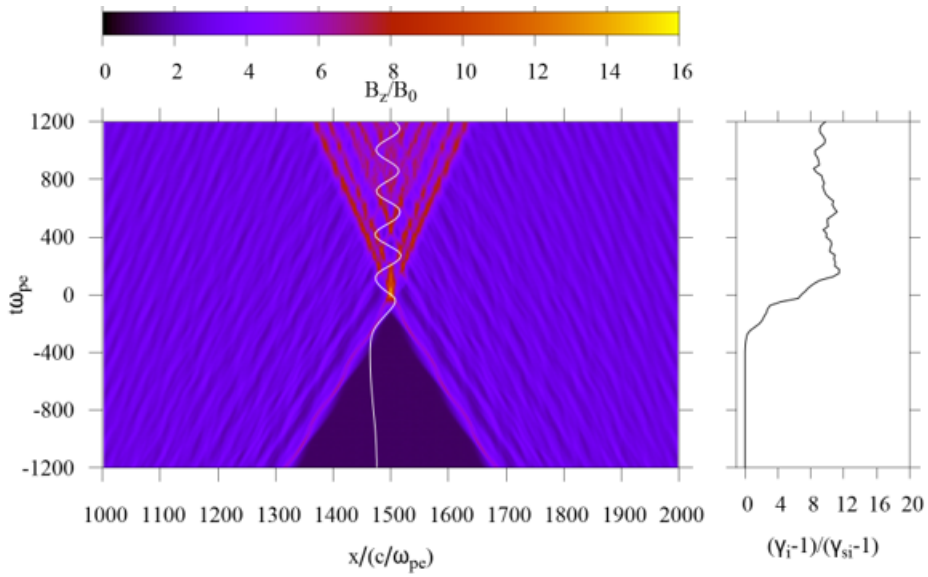


Figure 3.9: Left panel: An ion trajectory on the time-space evolution of the magnetic field B_z. Right panel: Time evolution of the ion energy.

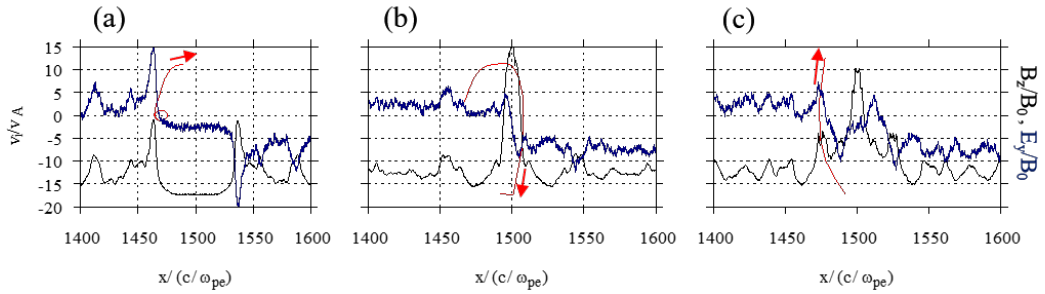


Figure 3.10: Schematic view of the ion acceleration.

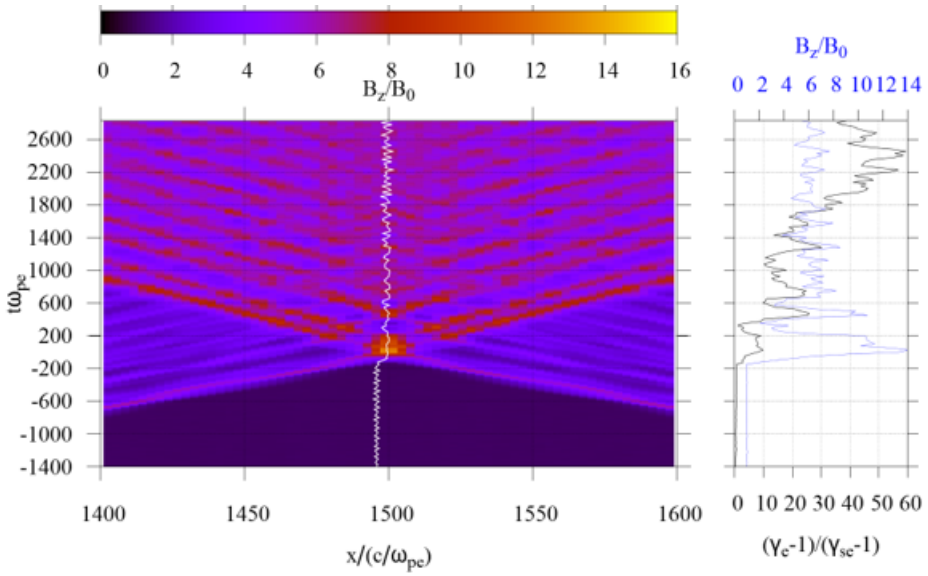


Figure 3.11: Left panel: An electron trajectory on the time-space evolution of the magnetic field B_z. Right panel: Time evolution of the ion energy and B_z experienced

3.3 Run B: Quasi-perpendicular Shock Waves

Part of this section is published as: Electromagnetic Structure and Electron Acceleration in ShockShock Interaction
Masaru Nakanotani, Shuichi Matsukyo, Tohru Hada, and Christian X. Mazelle, *The Astrophysical Journal*, Volume 846, Number 2, September 2017, doi: 10.3847/1538-4357/aa8363.

Here we mainly discuss an efficient electron acceleration mechanism in a quasi perpendicular shock-shock interaction using 1D full PIC simulation. Electrons are accelerated between the two shocks approaching with each other due to SDA. Those energetic electrons excite large amplitude waves between the shock waves via the electron firehose instability. The large amplitude waves scatter pitch angles of accelerated electrons. Scattered electrons become to be reaccelerated and reflected at the shock waves. This process leads to more and more energetic electrons.

3.3.1 Single Shock

When the magnetic field has a finite component parallel to the shock normal but less than the component perpendicular to the shock normal, electron motions are drastically changed. Here, we give an example of a single quasi-perpendicular shock wave whose Mach number is 13.6, ion and electron beta is 0.5 respectively, and shock angle is 90°. The shock wave is supercritical Kennel This shock wave is created by the injection method in the downstream rest frame. Fig. 3.14 shows the time-space evolution of the magnetic field, B_z. The shock speed is estimated with $-0.136c$. Since the upstream Alfvén speed is $0.01c$, the Mach number is 13.6.

The downstream values are consistent with a prediction from the Rankine-Hugoniot relation. From the relation the compression ratio, magnetic field B_z, and beta downstream

are 3.86, 3.88, and 14, respectively. Fig. 3.13 plots the density, pressure, electric fields and magnetic fields from the top to the bottom. The density and electromagnetic fields are normalized by the plasma density upstream and background magnetic field B_0, respectively. It is noted that because this is a 1D simulation, B_x is constant and $B_0 \cos\theta_{Bn}$ in this case. These values are plotted as dashed red lines in the figure. We can see that the shock front is located at around $2700c/\omega_{pe}$. The values downstream are almost the same with predictions from MHD approximation, especially for the density. Large amplitude fluctuations in the density profile are discussed as the characteristics of supercritical shocks Quest.

The shock wave appears to have several features, reflected electrons and waves excited. Fig. 3.12 shows electron (the left panels) and ion (the right panels) phase space density for the x, y, and z component of the velocity from the top to the bottom at certain time. This is consisted with the MHD equations While an ion motion is not different with ones in the case of $\theta_{Bn} = 90°$, some electrons are reflected and escaped upstream from the shock front. The reflection works as well an acceleration for electrons. This acceleration is called the drift shock acceleration. This can be interpreted as a mirror reflection in the de Hoffmann-Teller frame.Electrons drift along the y axis due to the gradient B drift and gain energy by the motional electric field. Some waves are excited around the shock front upstream. These waves are excited due to reflected electrons and cause a pitch-angle scattering for those electrons Matsukiyo et al. [2011], Guo et al. [2014].

As we have seen, electrons can be reflected at the shock and escape upstream. Therefore, we expect that those escaped electrons interact with the other shock after propagating upstream. It could be a favorable situation for an electron acceleration.

3.3.2 Shock-Shock Interaction

The color map in Fig. 3.15 shows the space-time evolution of the $z-$component of the magnetic field. We define the time at the collision of the two shocks as $t\omega_{ci} = 0$, where $\omega_{ci} = eB_0/m_i c$.

Before the collision ($t\omega_{ci} < 0$), Alfvén Mach number of the two shocks is $M_A = 13.6$ and magnetosonic Mach number is $M_{ms} = 10.4$ so that the two shocks are supercritical [Kennel, 1987]. Snapshots in three phases (before, at, and after the collision) are plotted in Fig. 3.16. The panels (a)-(c) show the profile of potential and magnetic field strength. In the panels (d)-(f), the color scale denotes the phase space density of electrons and the black line shows the density profile of electron. In the panels (g)-(i), the color scale indicates show the phase space density of ions and the temperature of electrons and ions are denoted by the red and the black lines, respectively.

The profiles of the two shocks roughly satisfy the Rankine-Hugoniot (RH) relation. From the density profile of electron (the black line) in Fig. 3.16(d), the downstream density averaged in $6000 \leq x/(c/\omega_{pe}) \leq 8100$ and $11900 \leq x/(c/\omega_{pe}) \leq 14000$ is indicated with the orange line which coincides with the value $3.9n_0$ estimated from the RH relation using $\Gamma = 5/3$ as polytrope index. The detailed downstream density profile denotes large amplitude fluctuations which are the characteristics of supercritical shocks [Quest, 1986]. We can see that there are energetic electrons between the two shocks (initial upstream thermal velocity is $v_{the} \sim 5v_A$) in the phase space of electron in Fig. 3.16(d). The detailed acceleration mechanism of these electrons is discussed in the next section. On the other hand, we confirm that there are no energetic ions between the two shocks in Fig. 3.16(g). As the result, effective upstream temperature of electron (the red line) is much higher than that of ions (the black line)

When the two shocks collide ($t\omega_{ci} = 0$), a strong peak of density can be seen (Fig. 3.16(e)). The maximum density is about $10n_0$ which can be interpreted as the sum of the overshoots of the original two shocks. The width of the peak is about $35c/\omega_{pe} = 3.5c/\omega_{pi}$ where $\omega_{pi} = \sqrt{4\pi n_0 e^2/m_i}$. This value is almost the same as that obtained by the previous hybrid simulation with $M_A = 8, \beta = 1$, and $\theta_{Bn} = 90^\circ$ [Cargill et al., 1986], although the direct comparison is difficult because of differences in parameters. Fig. 3.16(b) shows the electrostatic potential with red line at $t\omega_{ci} = 0$ normalized to $m_i u_{sh}^2/2$, where u_{sh} is

the shock speed in the upstream rest frame before the collision. The electrostatic potential steepens at the time of the collision the same as the density.

After the collision ($t\omega_{ci} > 0$), the two shocks propagate outward as seen in Fig. 3.15. The speeds of the shocks are more or less constant corresponding to $M_A = 10.5$ and $M_{ms} = 2.3$ indicating that the two shocks are still supercritical. The black line in Fig. 3.16(c) shows the profile of magnetic field strength, it is clear that magnetic fields are highly turbulent. The compression ratio of these shocks is about 2.2 which coincides with the value estimated from the RH relation assuming the polytropic index $\Gamma = 2$ in stead of $5/3$. This is because that after the collision, the shock angle becomes more perpendicular ($\theta_{Bn} \sim 82^\circ$) so that the degrees of freedom of the system may be close to 2 [Hoshino et al., 1992, Gallant et al., 1992]. The local increase (decrease) of the effective electron (ion) temperature downstream in $9600 < x/(c/\omega_{pe}) < 10400$ is seen in Fig. 3.16(i), while the sum (the blue line) remains roughly constant. The temperatures are defined as $k_B T_j = \sum_i^N m_j(|\vec{v}_{ji} - \vec{u}_j|^2)/3N$. The subscript j indicates the particle species (ion and electron), the term i indicates the i th particle, the parameter N is the number of particles. The vector $\vec{u}_j$ is an averaged velocity. The high electron temperature is the result of rapid electron acceleration just before the collision, which will be discussed in the following section. The electrons accelerated rapidly just before the collision are tied to the local magnetic fields which are also amplified at the same time in the shock-shock collision and aligned almost perpendicular to x. The local increase of electron temperature is the remnant of these.

Ions are accelerated through multiple interactions with the two shocks when their relative distance becomes shorter than the Larmor radii of the corresponding ions as discussed by Cargill et al. [1986]. Fig. 3.17 shows the trajectory of an accelerated ion (a, d) and the time evolution of the energy (b) and $E_y v_{iy}$ (c) with the black lines. The first acceleration occurs when the ion is reflected for the first time by the Shock 2 around $t\omega_{ci} \sim -1$ (the shaded region (i) in Fig. 3.17). Next, the reflected ion penetrates the Shock 1 and is ac-

celerated by the downstream motional electric field during $-0.25 \leq t\omega_{ci} \leq 0$ (the shaded region (ii) in Fig. 3.17). During this second acceleration, the two shocks collide. Due to its gyro motion, the ion crosses two separating shocks and enters the upstream of the left-ward propagating shock. During its stay in the upstream region (the shaded region (iii) in Fig. 3.17), the ion feels motional electric field upstream and is further accelerated. Here, one should note that the roles of upstream and downstream have changed after the collision. Therefore, the simulation frame has changed to the downstream rest frame. The total energy gain calculated in the simulation frame is about $10m_i v_{sh}^2/2$ where v_{sh} is the speed of the shocks before the collision.

We have seen that there are energetic electrons between the two shocks before colliding (see Fig. 3.16(d)). We find a non-thermal population which is absent initially. Fig. 3.18 shows the energy spectrum of electrons upstream at $t\omega_{ci} = -15$ integrated from $8200c/\omega_{pe}$ to $11800c/\omega_{pe}$ (the black line). Comparing with the initial Maxwell distribution (the dashed line), a power-law tail is produced from 0.1 up to 1 in $\gamma - 1$ where γ is the Lorentz factor. The power-law index is about 1.4.

These non-thermal electrons are accelerated by being repeatedly reflected at the two shocks. In Fig. 3.15, a high energy electron trajectory on the space-time evolution of B_z is described as the black line, the middle panel is the time evolution of its energy. We find that the electron is accelerated when it interacts with the shocks until $t\omega_{ci} < 0$. We confirm that the magnetic force at the particle position is much larger than the electrostatic force (the rightmost panel in Fig. 3.15). It means that the reflection are mainly due to the magnetic mirror and the electrostatic potential is not important. At each reflections, the acceleration occurs through the shock drift acceleration [Leroy and Mangeney, 1984, Wu, 1984, Matsukiyo et al., 2011, Park et al., 2013, Mann et al., 2009]. According to Park et al. [2013] and Mann et al. [2009], energy increase of each reflection on the upstream rest frame is estimated as

$$\gamma_r = \gamma_i \left[1 + \frac{2u_{sh}^{HT}(u_{sh}^{HT} + v_{i||})}{c^2 - (u_{sh}^{HT})^2} \right], \tag{3.1}$$

where γ_r and γ_i are the Lorentz factor after and before a reflection, respectively, $u_{sh}^{HT} = u_{sh}/\cos\theta_{Bn} > 0$ and $v_{i||}$ is parallel velocity before reflection. The speed u_{sh} and u_{sh}^{HT} are the shock speed in the simulation frame and in the de Hoffmann-Teller frame. For the electron show in Fig. 3.15, the increments of the first two reflections are estimated as 1.85 and 1.65, respectively. Eq. (3.1) gives $\gamma_r/\gamma_i = 1.69$ and 1.63 for the first two reflections by using the parallel velocity just before the reflection, $v_{i||} = 0.9c$ and $0.8c$, respectively. The values are in good agreement with the simulation result.

At the collision ($t\omega_{ci} \sim 0$), pre-accelerated electrons are further accelerated rapidly through the process different from the shock drift acceleration. Figs. 3(d)-(f) also show a trajectory of such an electron with the red lines. At $t\omega_{ci} = -3$, the electron has been already pre-accelerated up to the Lorentz factor of $\gamma_e \sim 20$. Its gyro radius is $\rho_e \sim 125c/\omega_{pe}$ (indicated by the horizontal arrow) and its gyro period is $T_{e,gyro}\omega_{ci} \sim 1$ (indicated by the vertical arrow), respectively. After $t\omega_{ci} > -1.5$, the electron gains energy in a multi-step manner when it glances off a downstream region of a shock. The acceleration time in each step, indicated by the gray bars, is clearly shorter than its gyro period. In each interaction with a shock the electron is reflected after experiencing partial gyro motion in a downstream region. The direction of the partial gyro motion is always anti-parallel to the motional electric field, presenting in the red and blue regions in Fig.3(d), so that $-E_y v_{ey} > 0$ as shown in Fig.3(f). This is actually what happens to the ion indicated by the black lines in Figs.3(a)-(c) and to the ions discussed by Cargill et al. [1986].

Fig. 3.19 (a) shows the space-time evolution of the y component of the magnetic field. The large amplitude waves (LAWs) are excited between the two shocks before the collision. The amplitude of these waves have spatial changes only. These changes appear nearly sinusoidal. In other words, these waves are non-propagating waves. They have a typical wavenumber of $k_w \sim 0.11\omega_{pe}/c$ and amplitude of $B_w \sim 0.5B_0$.

The excitation mechanism is the electron firehose instability due to an electron temperature anisotropy [Li and Habbal, 2000]. However, there is no anisotropy in the ion

temperature because ions are not escaped upstream in this particular case. The top panel of Fig. 3.20 shows the time evolution of magnetic fluctuations. The LAWs are visible in δB_y^2 (the solid line) from the time $t\omega_{ci} \sim -25$, the amplitude growth rate is about $0.18\omega_{ci}^{-1}$ at that time. The middle panel of Fig. 3.20 shows the time evolution of the parallel (black line) and perpendicular (dashed line) electron beta ($\beta_{e||}, \beta_{e\perp}$) averaged in the region between the two shocks. While both $\beta_{e||}$ and $\beta_{e\perp}$ grow in time, $\beta_{e||}$ is higher that $\beta_{e\perp}$ due to the reflected electrons which gain energy mostly parallel to the magnetic field through SDA[Matsukiyo et al., 2011] . The bottom panel of Fig. 3.20 shows the time evolution of the anisotropy factor defined as $A \equiv 1 - T_{e\perp}/T_{e\|} - S/\beta_{e\|}^{\alpha}$. According to Gary and Nishimura [2003], the firehose instability sets in when $A > 0$ for $S = 1.29$ and $\alpha = 0.97$. The values S and α have been used here. When the LAWs start to grow, A is sufficiently large and after that A is decreased.

It is known that in the oblique firehose instability with $\theta > 30^{\circ}$, where θ is the angle between $\mathbf{k}$ and $\mathbf{B_0}$, the waves become non-propagating and the fluctuating magnetic field excited is parallel to $\mathbf{k} \times \mathbf{B_0}$ [Li and Habbal, 2000]. Due to the dimensionality of the simulation $\mathbf{k}$ directs the x direction. Therefore only B_y is fluctuating, which is consistent with the above properties.

Before the excitation of the firehose instability, $-42.5 \leq t\omega_{ci} \leq -25$, the magnetic field fluctuations δB_y and δB_z gradually increase due to a resonant instability. In Fig. 3.19 (b), one can identify the waves propagating with the phase speed of $\sim 2v_A$ (guided by the white dashed line) and wavelength of $\sim 20c/\omega_{pe}$. Evaluating $\zeta_n = (\omega - k_{\|}v_{\|} - n\omega_{ce})/\omega_{ce}$ for $n = 0, \pm 1, \pm 2$, we obtain $\zeta_0 \approx -0.91, \zeta_1 \approx -1.9, \zeta_{-1} \approx -0.089, \zeta_2 \approx -2.9$, and $\zeta_{-2} \approx 1.1$, respectively. This implies that the waves get excited via electron anomalous cyclotron resonance with $n = -1$. The waves are right hand polarized. We estimate the growth rate of the instability from Fig.3.20 as $\sim 0.027\omega_{ci}$ which is in good agreement with the linear growth rate obtained by the kinetic dispersion relation.

The LAWs play a crucial role in the electron acceleration before the collision. Fig. 3.21

schematically shows how some electrons are reflected and accelerated at the two shocks in the upstream plasma frame. Let us consider the electrons which initially distributed inside the semi-circle labeled by 'u' (the shaded region). Suppose that the electrons first interact with the Shock 1. The two oblique solid lines denote the loss-cone of the Shock 1. Therefore, only the electrons outside the loss-cone bounded by the orange lines are reflected at the Shock 1. The reflected electrons are mapped to the blue region labeled by 's_{1r}'. The electrons are symmetrically reflected for the speed $-v_{sh}/\cos\theta_{Bn}$ as long as a shock speed and the speed of electrons [Park et al., 2013]. As one can see, the electrons have smaller pitch angles after reflected. These electrons may not be able to be further reflected when they encounter the Shock 2 because they are inside the loss cone, indicated by the two dashed lines, of the Shock 2. However, if the LAWs efficiently scatter these electrons in pitch angle, they may spread in the shaded area bounded by the two blue lines. After the scattering, the Shock 2 may reflect the electrons outside the loss-cone (the red-shaded region).

To investigate the actual motion of electrons interacting with the LAWs, we use a test particle simulation in which we give the fields imitating the LAWs and the back ground magnetic field. In the test particle simulation, the back reaction of the particle dynamics is ignored, we solved a particle motion only in the given fields below,

$$\mathbf{B}/B_0 = \mathbf{b_0} + \mathbf{b_w}, \vec{E} = 0, \tag{3.2}$$

$$\mathbf{b_0} = (\cos\theta_{Bn}, 0, \sin\theta_{Bn}), \tag{3.3}$$

$$\mathbf{b_w} = (0, \kappa\sin kx, 0). \tag{3.4}$$

We solve the equations of motion of 4000 particles with the time step $\Delta t = 0.05\omega_{pe}^{-1}$ for $5\omega_{ci}^{-1}$ using the Buneman-Boris method. The LAWs are almost monochromatic waves so that approximated by $\mathbf{b_w}$ in eq. (3.4). As the initial condition, particles have various speeds

$(0 < v < 0.99c)$ and a constant pitch angle $\pi/6$. Furthermore, we define $\theta_{Bn} = 60°, \kappa = 0.5, k = 0.11(\omega_{pe}/c)$ from the simulation.

We find that energetic electrons are efficiently scattered in pitch angle between 0 to $\pi/2$. Fig. 3.22 (a) shows the particle distribution in the parallel and perpendicular velocity space at the end of the test particle simulation for $\kappa = 0.5$. The red and black points indicate particles in the phase space at the initial and the end of the simulation, respectively. Because there is no electric field in the test particle simulation, a particle moves along a circle whose radius remains constant with its initial speed in the phase space.

Such efficient scattering occurs through the cyclotron resonance. Now the resonance condition is given as $k_{||}v_{||R} = n\omega_{ce}/\gamma_e$, where $k_{||} = k\cos\theta_{Bn}$, $v_{||R}$ is the particle speed parallel to $\mathbf{B}$, $\gamma_e = [1 - (v_{||R}^2 + v_{\perp R}^2)/c^2]^{-1/2}$ ($v_{\perp R}$ is the particle speed perpendicular to $\mathbf{B}_0$), and n is the harmonic number integer. We confirmed that efficient scattering occurs only for the particles satisfying the above resonance condition when the wave amplitude is small enough. Fig. 3.22 (b) shows the particle distribution in the parallel and perpendicular velocity space at the end of the test particle simulation for $\kappa = 0.01$. The other parameters are same with Fig. 3.22 (a). One can clearly see that two groups of particles are efficiently scattered in pitch angle. The particles with $v \sim 0.9c$ satisfy the resonance condition with $n = 1$ (the fundamental resonance), while the particles with $v \sim 0.97c$ satisfy the condition with $n = 2$ (the second harmonic resonance). Now $\kappa = 0.5$ is rather large. Hence, a number of particles with wider velocity region can resonate with the LAWs and be scattered as in Fig. 3.22 (a) and (b). Since ions do not resonate with the LAWs (the resonance speed for ions, $v_{||R} \sim 0.02c$, is larger than the thermal speed of ions, $v_{thi} = 0.005c$), they are not affected by those waves.

Fig. 3.22 (c) and (d) denote electron phase space density obtained from the PIC simulation at $t\omega_{ci} = -35$ and -15, respectively. Before that the LAWs are excited, the reflected electrons are distributed in relatively limited region in the phase space (Fig. 3.22 (c)). In contrast, after that the LAWs are excited, the reflected electrons are distributed in wider

region in phase space including large pitch angles (Fig. 3.22 (d)). This indicates that the electrons scattered by the LAWs and gaining large pitch angles can be easily reflected when they encounter the other shock. It should be also noted that some electrons have negative $v_{||}$. They have been scattered back by the LAWs toward the shock they first encountered. An example of such a trajectory is seen in the PIC simulation(the red line in Fig. 3.17). This is the process discussed by Matsukiyo et al. [2011] and Guo et al. [2014].

For the specific parameters investigated here, only electrons are accelerated through the above mechanism. In spite of that some ions are specularly reflected at the same shocks, they return to the original shock due to their gyro motion and do not stream back toward upstream. This is due to that the shock angle is too large [Gosling and Robson, 1985]. For smaller shock angles, it was reported that back streaming ions are produced and some of them are accelerated through the similar process to for electrons [Cargill, 1991b].

In the current simulation, any further electron and ion acceleration is not confirmed after $t\omega_{ci} = 1$. This may be due to the limited simulation time. After the collision, the upstream regions of the two shocks are highly turbulent. This is the preferred situation for the DSA process (e.g., Guo and Giacalone [2015]). The shocks after the collision have rather small magnetosonic Mach numbers, as already mentioned in section 3, and they are high beta quasi-perpendicular shocks. It is pointed out that the shocks of this type can efficiently accelerate electrons through the relativistic shock drift acceleration mechanism [Matsukiyo et al., 2011]

We observe the speed of the two shocks are clearly modified later in the simulation ($t\omega_{ci} \geq -10$). One possible reason for this is that the propagation for the shocks has been free from the influence due to the two spatial boundaries after $t\omega_{ci} \sim -10$. Another possibility is nonlinear modification of the shock speed due to the effect of the pre-accelerated electrons already before the shocks collide. In Fig. 3.15, the blue line is tangent to the shock front during the time $-65 \leq t\omega_{ci} \leq -45$. Here, $t\omega_{ci} = -45$ corresponds to the time at which the reflected electrons first reach the other shocks. The slope of the blue

line indicates the initial shock speed which is $13.6V_A$. One can see that the gap between the blue line and the shock front position becomes clear in the later time ($t\omega_{ci} > -10$). The shock speed decreases from initial $13.6V_A$ to $12.9V_A$ just before the collision. This is interpreted as the modification of the shock [Drury and Voelk, 1981] probably because of the large electron pressure provided by the reflected high energy electrons (Fig. 3.16). The modification is too small to apparently change the compression ratio. We expect that it becomes clearer if a sufficiently large scale simulation is carried out.

Figures

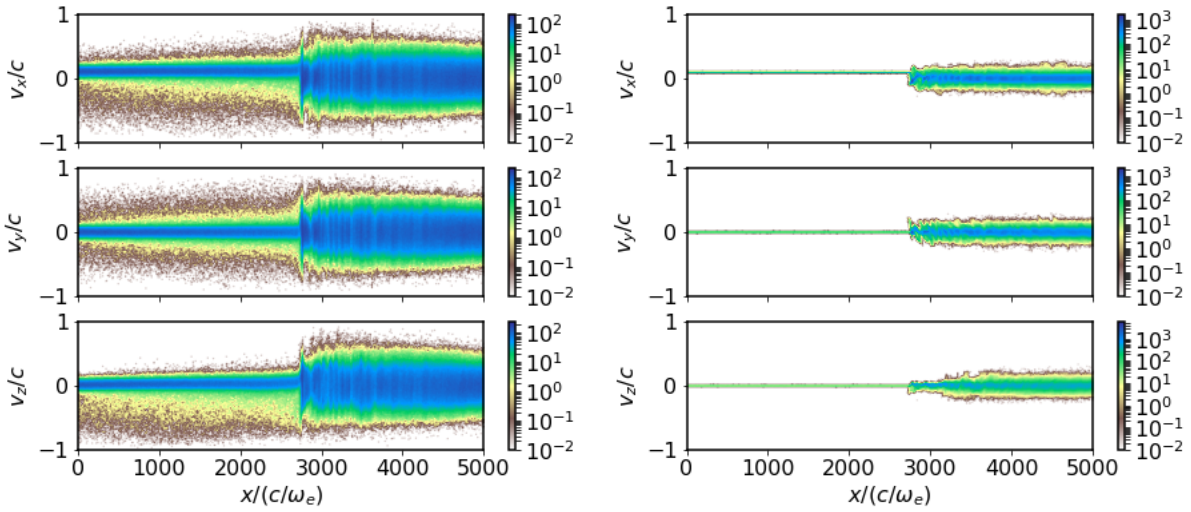


Figure 3.12: Left panels: electron phase space density of v_x, v_y, and v_z from the top to the bottom. Right panels: ion phase space density of v_x, v_y, and v_z from the top to the bottom.

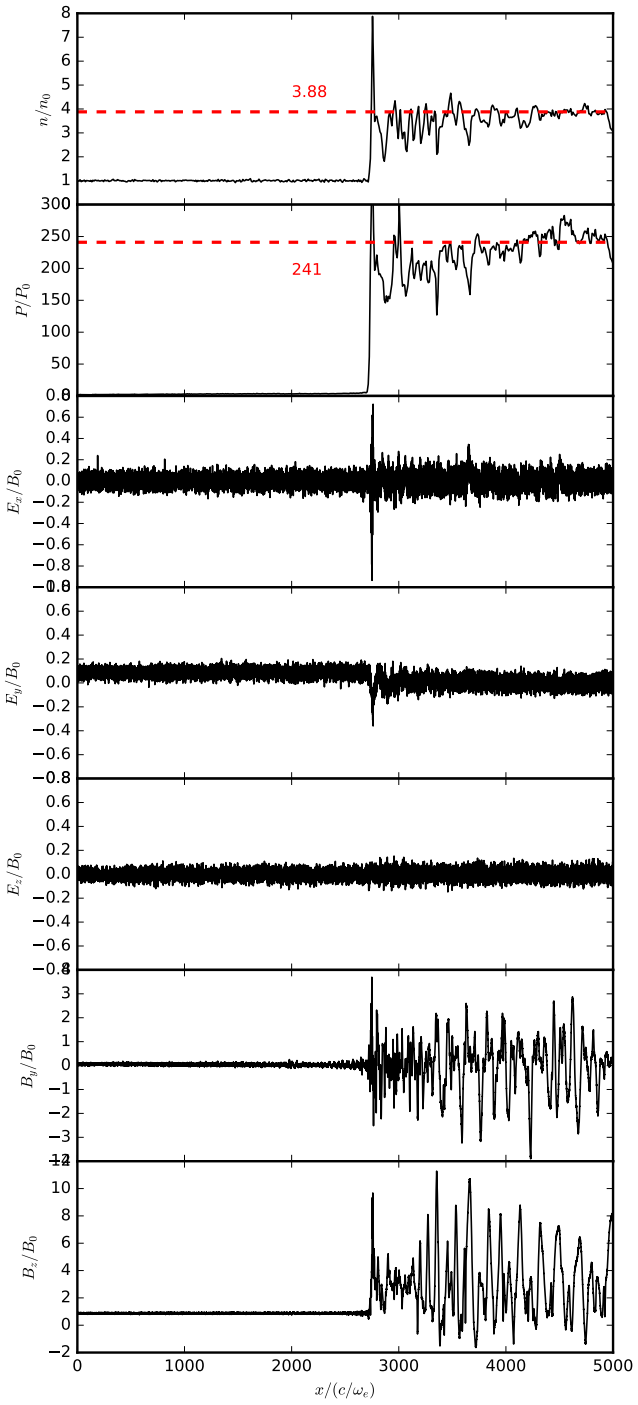


Figure 3.13: The plasma density, plasma beta, electric field E_x, E_y and E_z, magnetic field B_y, and B_z from the top to the bottom.

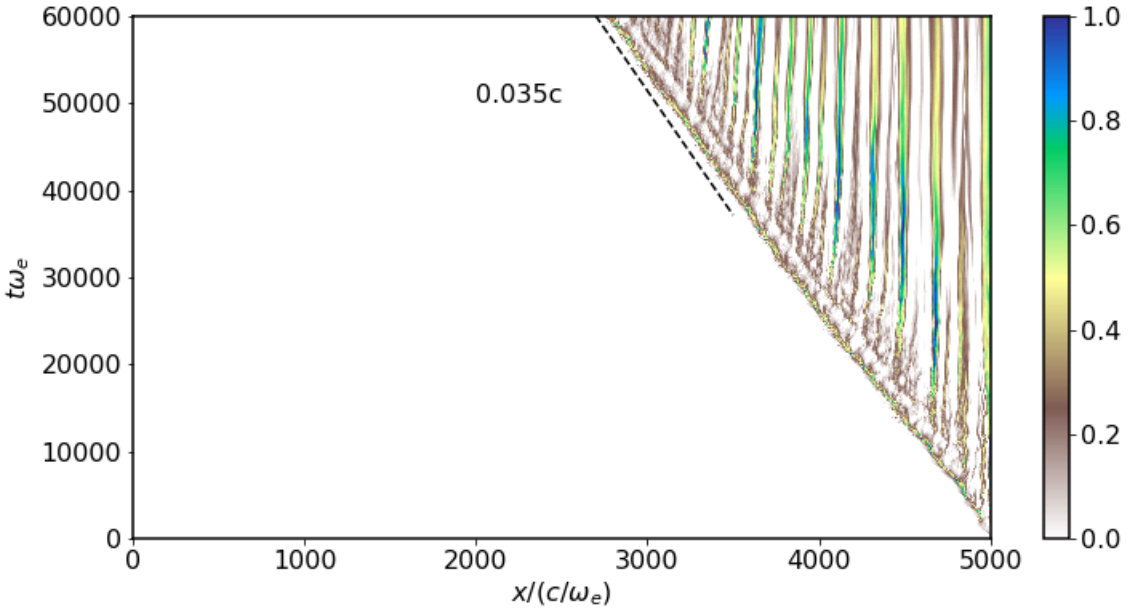


Figure 3.14: The time-space evolution of the magnetic field B_z.

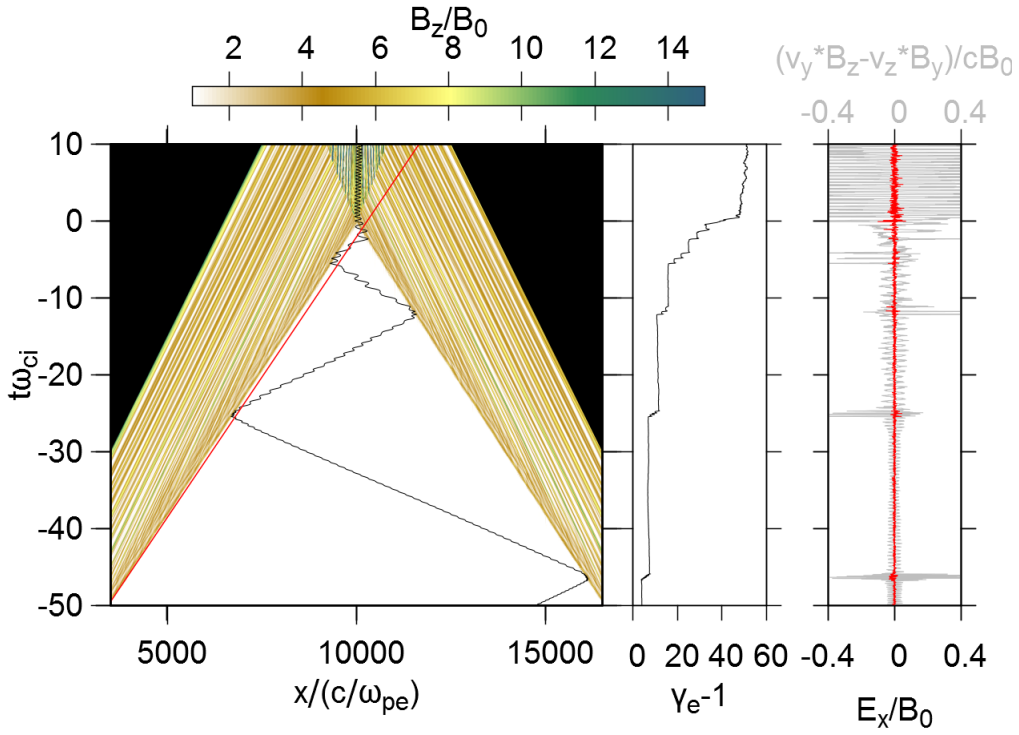


Figure 3.15: Space-time evolution of the $z-$ component of magnetic field. The black color shows out of the walls, and the white region is the upstream of the two shocks. An energetic electron trajectory is superimposed. The slope of red line corresponds to the velocity of 0.136c. The time evolution of the energy (middle panel) and the electrostatic (red line) and magnetic (gray line) force experienced by the electron (right panel).

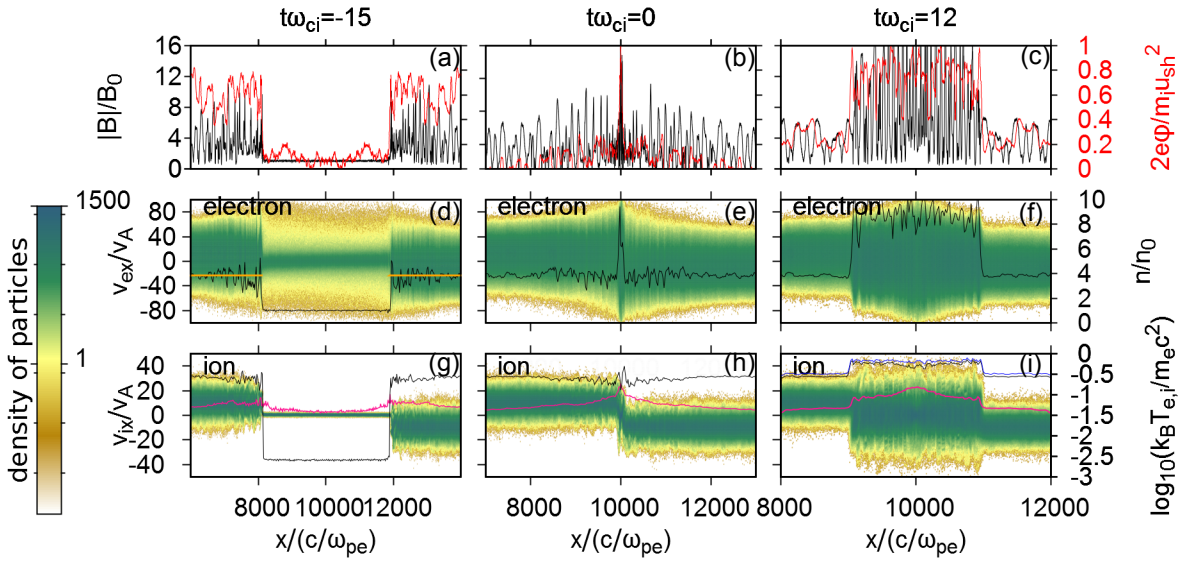


Figure 3.16: The profile of potential and magnetic field strength (a-c), phase space density of electrons (d-f) and ions (g-i) before, at and after the collision from left to right. The black lines in the middle panels show the plasma density at the corresponding time. The black and red lines in the bottom panels show the ion and electron temperature, respectively, at the corresponding time. The blue line shows the sum of the electron and ion temperature. The orange lines correspond to 3.9.

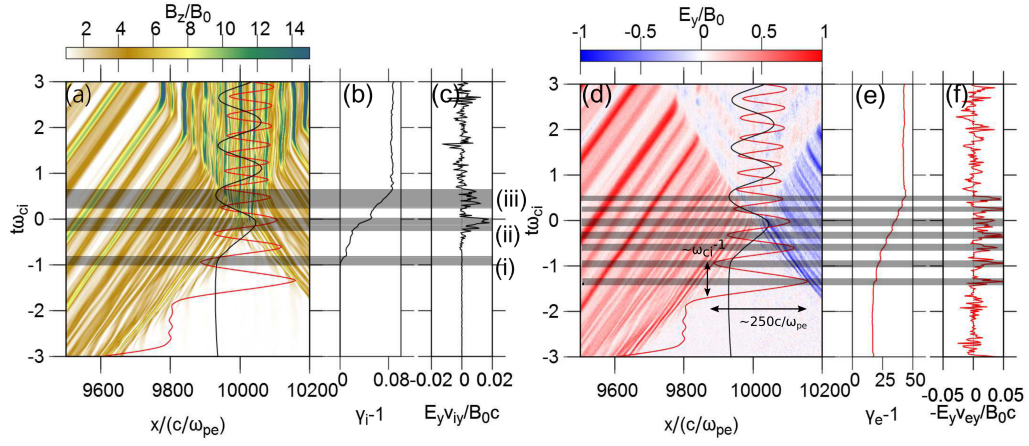


Figure 3.17: An accelerated ion trajectory (a, d) and time evolution of the energy (b) and $E_y v_{iy}$ (c) as displayed in black. An energetic electron trajectory (a, d) and time evolution of the energy (e) and $-E_y v_{ey}$ (f) around the colliding as displayed in red. Here γ_e and γ_i are the Lorentz factors of the electron and the ion. The color map is the space-time evolution of B_z (a) and E_y (d).

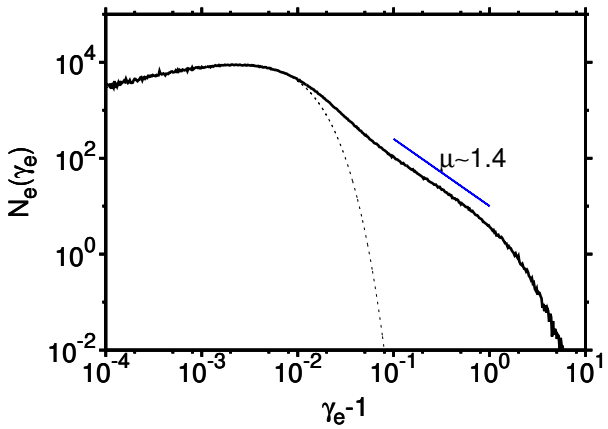


Figure 3.18: The solid line shows upstream electron energy distribution function at $t\omega_{ci} = -15$. Blue line with the index $\mu = 1.4$ is indicated as a reference. The dashed line shows the Maxwell distribution with the initial upstream condition.

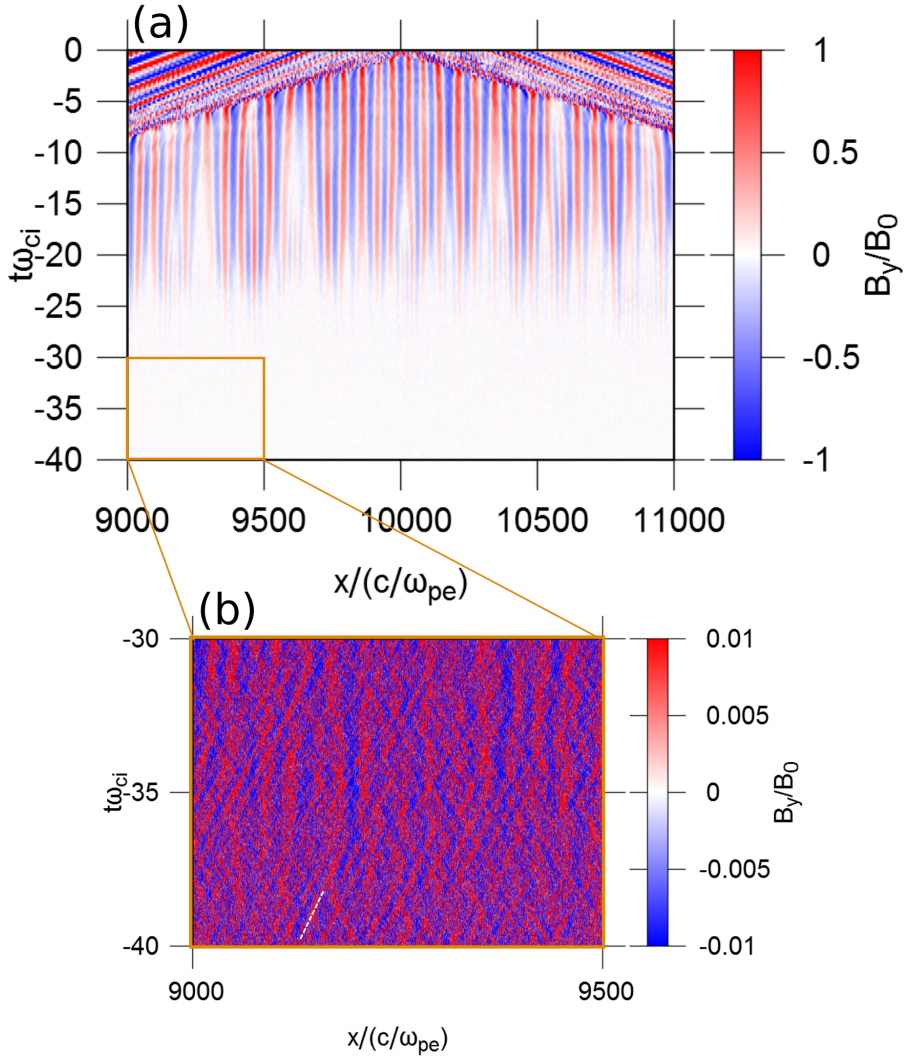


Figure 3.19: (a) Space-time evolution of the $y-$ component of the magnetic field and (b) the enlarged view with a different scale of By. White dashed line corresponding the speed of 0.02c is indicated as a reference.

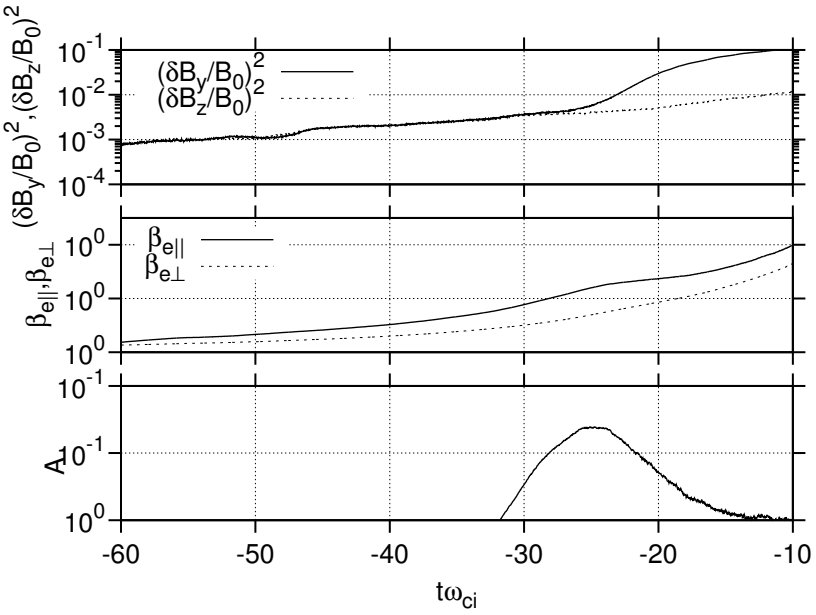


Figure 3.20: Time evolution of the increment of the $y-$ (solid) and $z-$ (dashed) component of the magnetic field fluctuations (top panel), the parallel (solid) and perpendicular (dashed) electron plasma beta (middle panel) and the criteria of the fire hose instability (bottom panel).

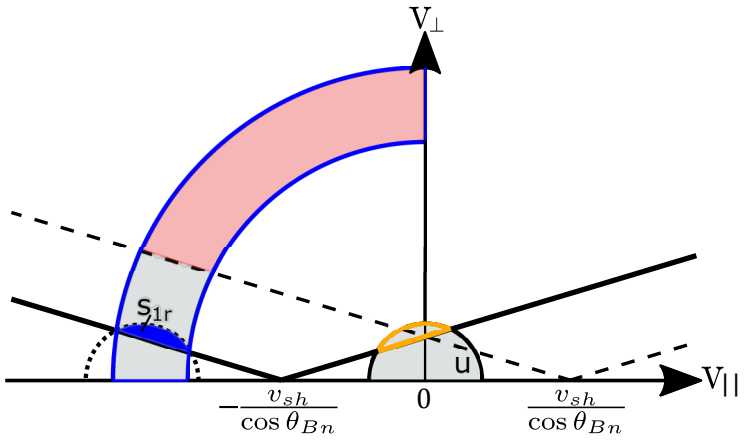


Figure 3.21: Schematic condition of the SDA in $v_{||} - v_\perp$ space on the upstream rest frame.

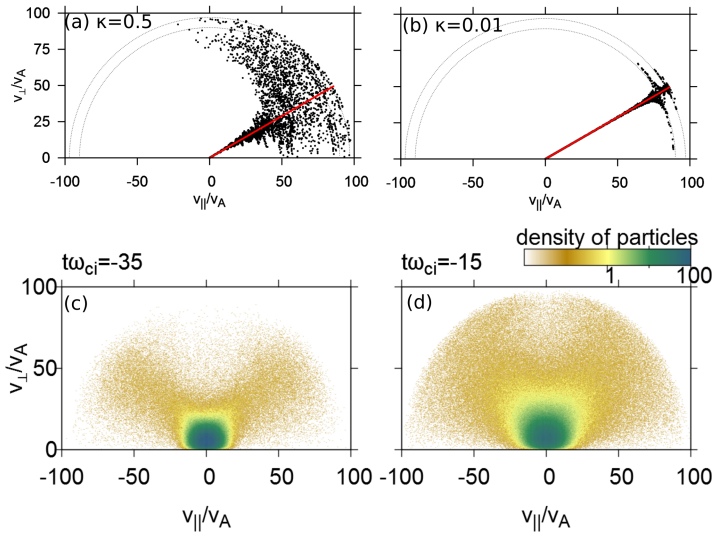


Figure 3.22: (a) and (b) are phase space of parallel and perpendicular velocity from the test particle simulation. Red and black points indicate the initial and final position of the particles for $\kappa = 0.5$ (a) and $\kappa = 0.01$ (b). The dashed curve corresponds with the speed of $0.9c$ and $0.97c$. Electron phase space density for parallel and perpendicular velocities between the two shocks from the PIC simulation at $t\omega_{ci} = -35$ before the LAWs are excited (c) and $t\omega_{ci} = -15$ after the excitation (d).

3.4 Run C: Quasi-Parallel Shock Waves

Here we discuss a shock-shock interaction for two quasi-parallel shock waves using 1D full PIC simulation. In this case, ions are reflected and escape upstream. Reflected ions reach to the other shock wave and reaccelerated at the shock wave via the scatter-free acceleration. When distance between the two shocks is about an ion Larmor radius, ions are highly accelerated and the ion pressure becomes larger than the pressure downstream. Finally, accelerated ions could modify the shock structures against an MHD prediction.

3.4.1 Single Shock

When the parallel component of the magnetic field is larger than the perpendicular component, shock dynamics is qualitatively modified. In this case, ions can also escape from the shock wave. This ion beam excite several waves as a free energy source. Here, we give an example of a single shock structure whose Mach number is 13.2, ion and electron beta is 0.5 respectively, and shock angle is 30°. This shock wave is created by the injection method in the downstream rest frame. Fig. 3.23 shows the time-space evolution of the magnetic field, B_z. The shock speed is estimated with $-0.132c$. Since the upstream Alfvén speed is $0.01c$, the Mach number is 13.2.

The downstream values are consistent with a prediction from the Rankine-Hugoniot relation, especially relation for the density. From the relation, the compression ratio, magnetic field B_z, and pressure downstream are estimated as 3.9, 3.95, and 214, respectively. Fig. 3.24 plots the density, beta, electric fields and magnetic fields from the top to the bottom. The density and electromagnetic fields are normalized by the plasma density upstream and background magnetic field B_0, respectively. It is noted that because this is a 1D simulation, B_x is constant and $B_0 \cos\theta_{Bn}$ in this case. These values are plotted as dashed red lines in the figure. We can see that the shock front is located at around $3500c/\omega_{pe}$. The pressure in the fore shock region becomes large. It is thought that a reflected ion beam from

the shock has an effective large temperature.

The shock wave appears to have several features, reflected ions and waves upstream. Fig. 3.25 shows electron (the left panels) and ion (the right panels) phase space density for the x, y, and z component of the velocity from the top to the bottom at certain time. As in the case of $\theta_{Bn} = 30^\circ$, electrons are reflected and accelerated at the shock front (SDA). It is, however, not so efficient because SDA is parameterized by $1/\cos\theta_{Bn}$. A more prominent feature is an ion beam. Some of ions are specularly reflected at the shock front due to the shock potential which is created by the charge separation between ions and electrons Gosling et al. [1982]. These ions can be a free energy and excite waves upstream Tsubouchi and Lembège [2004], Kato [2015], Scholer [1993], Scholer et al. [2003]. These waves are also observed in-situ observation in the foreshock region of the bow shock Giacalone et al. [1993], Lucek et al. [2002], Behlke et al. [2003]. We expect that when two quasi-parallel shocks approach with each other, two ion beams can interact with the other shock wave and are accelerated. We can see waves excited by the ion beam in the foreshock region (the sixth and seventh panels in Fig. 3.24).

As we have seen, ions play an important role for the shock structure. Considering a shock-shock interaction for two quasi-parallel shock waves, it is natural to expect that reflected ions could interact with the shock waves multiple times and it would lead to enegetic ions during the shock-shock interaction.

3.4.2 Shock-shock interaction

We discuss what happens when two identical quasi-parallel shock waves approach. Fig. 3.26 shows electron phase-space density and the magnetic field B_y, ion phase-space density and the density profile, and ion energy-space density and the ion pressure from the top to the bottom for three times, respectively. When the two shocks are far away ($t\omega_{pe} = -38$), we can confirm two symmetric beams propagating oppositely. Also, some of electrons are also reflected from the shock front due to the SDA. As the two shocks get closer, the ion

beams are no longer to keep them as a beam ($t\omega_{pe} = -16$). They look trapped at the shock front and accelerated. In the middle-bottom panel, those trapped ions have large energy up to $\gamma_i - 1 \sim 0.2 m_i c^2$. We can see that there are two density spikes upstream ($x/(c/\omega_{pi} \sim 975, 1025$). At the time $t\omega_{pe} = 0$, the shock fronts are around $x/(c/\omega_{pi}) = 1000$. It is clear that ions are highly accelerated to the limit of $\gamma_i - 1 \sim 0.4 m_i c^2$. Fig. 3.27 shows the time-space evolution of the plasma density and the right panel is the scale-up of encircled region by an orange line in the left panel. While the two shocks propagate with a constant speed, in the enlarged view, the two shocks appear to be deflected when the two shocks get close within an ion gyro radius. It is seemed that energetic ions which have a larger pressure than the downstream pressure reflect the shock waves. That is what we discuss afterward.

Some representative accelerated ions are also plotted in the Fig. 3.27. The associated right panel is the time evolution of those corresponding ion energy. We can see these ions are sometimes reflected and sometimes trapped at the shock front. When they interact at the shock front, they gain energy. This acceleration mechanism is interpreted as a scatter-free ion acceleration process Scholer [1990], Sugiyama and Terasawa [1999], Kato [2015]. When the two shock get closer within one ion Larmor radius, these ions gyrate around the two shock fronts several times and gain energy from the motional electric field which is finite in the downstream of the shocks.

Fig. 3.28 shows ion energy spectra at three times ($t\omega_{ci} = -38, -17, 0$). We integrate ions upstream of the shock. When the two shock are separated with each other ($t\omega_{ci} = -38, -17$), we can see that there are the ion background core and reflected ions ranging $\gamma_i - 1 = 0.0.1 m_i c^2 \sim 0.2 m_i c^2$. At the time $t\omega_{ci} = 0$, non-thermal ions clearly exist from $0.01 m_i c^2$ to $1 m_i c^2$. Some ions are accelerated to nearly the relativistic regime.

Fig. 3.29 shows the time-space evolution of the density (the left-side) and the ion pressure (the right-side) corresponding to the encircled region in the Fig. 3.27. We can see that when the two shocks are well-separated at the time $t\omega_{ci} \sim 76$, the ion pressure upstream

is larger than the downstream pressure enhanced by a shock compression. This increment upstream caused by ions. The right panel shows the ion and electron pressure at the time $t\omega_{ci} \sim 76$. While electron pressure upstream is smaller than the pressure downstream, the ion pressure upstream is much larger than the electron pressure and the ion pressure downstream. This large ion pressure upstream comes from accelerated ions. Fig. 3.30 shows cumulative energy spectra for the ion pressure (red) and the ion density (blue). This lines mean a ratio of the number of ions or the ion pressure satisfying a condition which is above a certain energy. From this figure, we can understand that while the ration of the number of ions above the energy 0.02 is about 10%, 95% of the ion pressure is supported ions above the energy 0.02.

We perform MHD simulations to investigate the effect of ions accecerated during the approaching of the two shocks. The method we use here is described in Kawai [2013].

At the first, we show simulation results without energetic ions to compare the results with the case with energetic ions. The initial condition is separated in two states at the center of the simulation box. The left and right side conditions are

$$(\rho_L, v_{xL}, v_{yL}, v_{zL}, P_L, B_{xL}, B_{yL}, B_{zL}) = (3.92, 9.82, 0.0, -0.0988, 124.5, 0.866, 0.0, 1.985)\,, \tag{3.5}$$

$$(\rho_R, v_{xR}, v_{yR}, v_{zR}, P_R, B_{xR}, B_{yR}, B_{zR}) = (3.92, -9.82, 0.0, 0.0988, 249, 0.866, 0.0, 1.985)\,. \tag{3.6}$$

Here, the density, velocity, pressure and magnetic fields are normalized by ρ_0, v_A, $\rho_0 v_A^2$ and B_0 where ρ_0 is the upstream density before the collision, v_A is Alfèn velocity, B_0 is the upstream background magnetic field before the collision, respectively. The values are determined from the Rankine-Hugoniot relation for the conditions of $M_A = 13$, $\beta = 1$ and $\theta_{Bn} = 60^circ$. Fig. 3.31 shows the time-space evolution of the density. Due to the periodic boundary condition, rarefaction waves propagate from the boundaries. From the center of the simulation box, two shock waves propagate outward with the shock speed of $6v_A$. Here,

it is in the downstream-rest frame.

Second, we add a high pressure region between the two shocks. The condition of the region is

$$(\rho_M, v_{xM}, v_{yM}, v_{zM}, P_M, B_{xM}, B_{yM}, B_{zM}) = (1.0, 0.0, 0.0, 0.0, 1.47, 0.866, 0.0, 0.5)\,. \tag{3.7}$$

The pressure is 2 times larger than the downstream pressure. The regions is broaden over 200 grids. The downstream regions and the high pressure region are linearly connected over 100 grids. Fig. 3.32 shows the time-space evolution of the density (left-side) and the pressure (right-side). Rarefaction waves still propagate from the boundaries. After $t/T_0 \sim 0.035$, two shock waves propagate with the velocity of $6v_A$. The speed of the shocks consists with the case without energetic ions. We can see a dented region of the density at the center of the simulation box. Because of the high pressure region, new shock waves are created at the boundaries between the downstream region and the high pressure region. It is seen that the inner propagating shock waves interact with each other and stop at $x/L_0 \sim 1.8$ in the left hand side.

As we discussed, accelerated ions could modified structures of the shock-shock interaction comparing with the case without energetic ions. It is important to consider the effect of energetic ions for understanding the shock-shock interaction. When there are energetic particles between the two shock waves, they push the shock waves back. The speed of the shock waves after the interaction does not change comparing the case without energetic ions. A hollow region between the two shocks emerges.

Figures

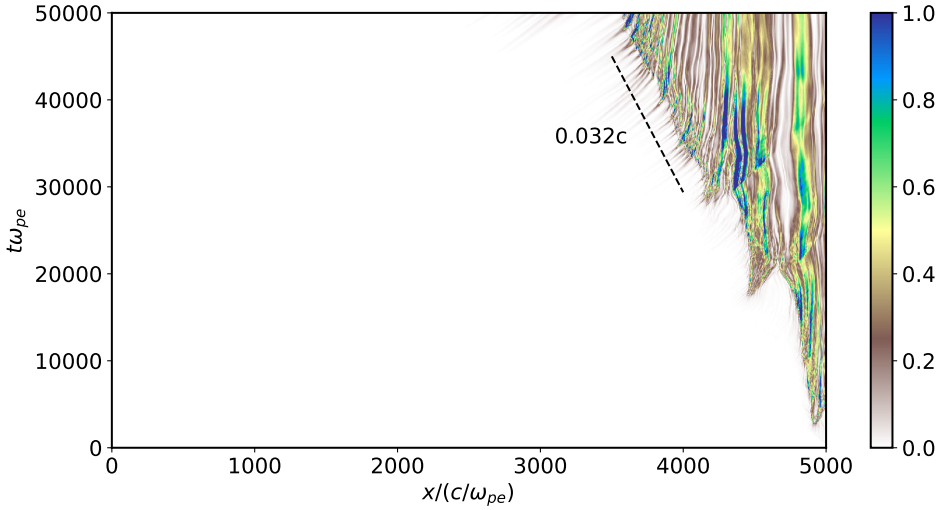


Figure 3.23: The time-space evolution of the magnitude of the magnetic fields

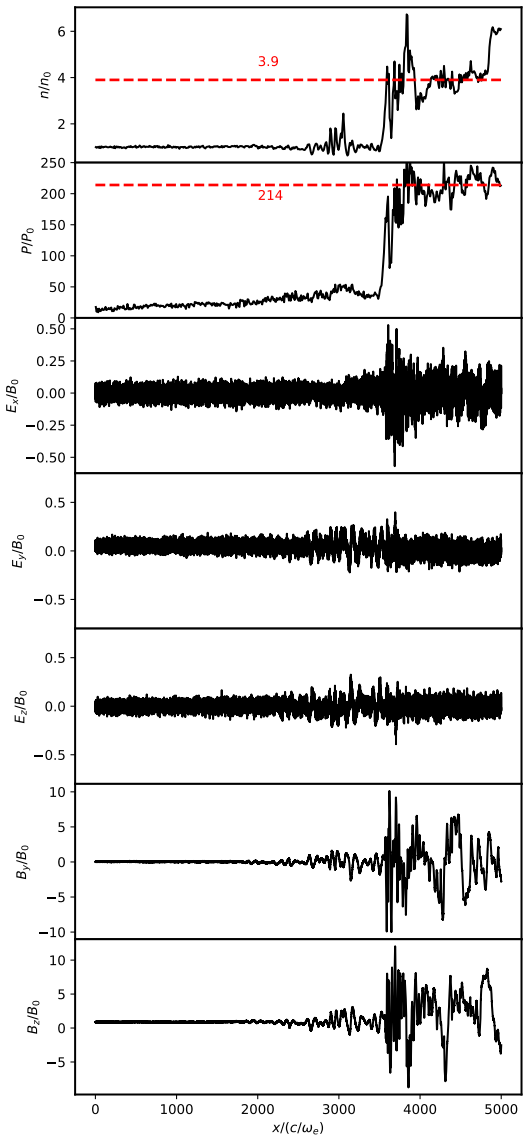


Figure 3.24: Profiles of the density, pressure, electric fields, and magnetic fields.

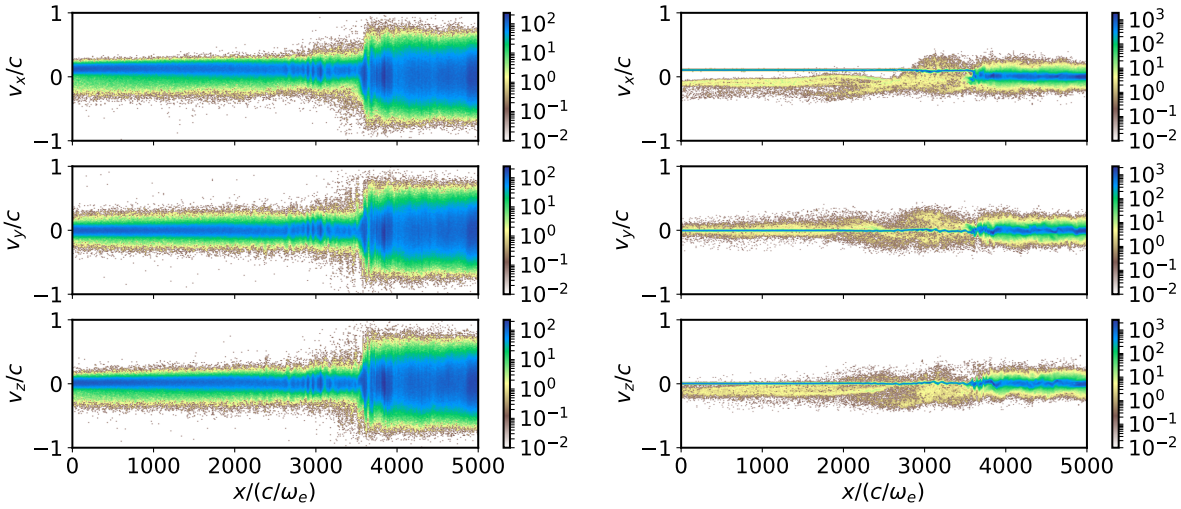


Figure 3.25: Left panels: electron phase space density of v_x, v_y, and v_z from the top to the bottom. Right panels: ion phase space density of v_x, v_y, and v_z from the top to the bottom.

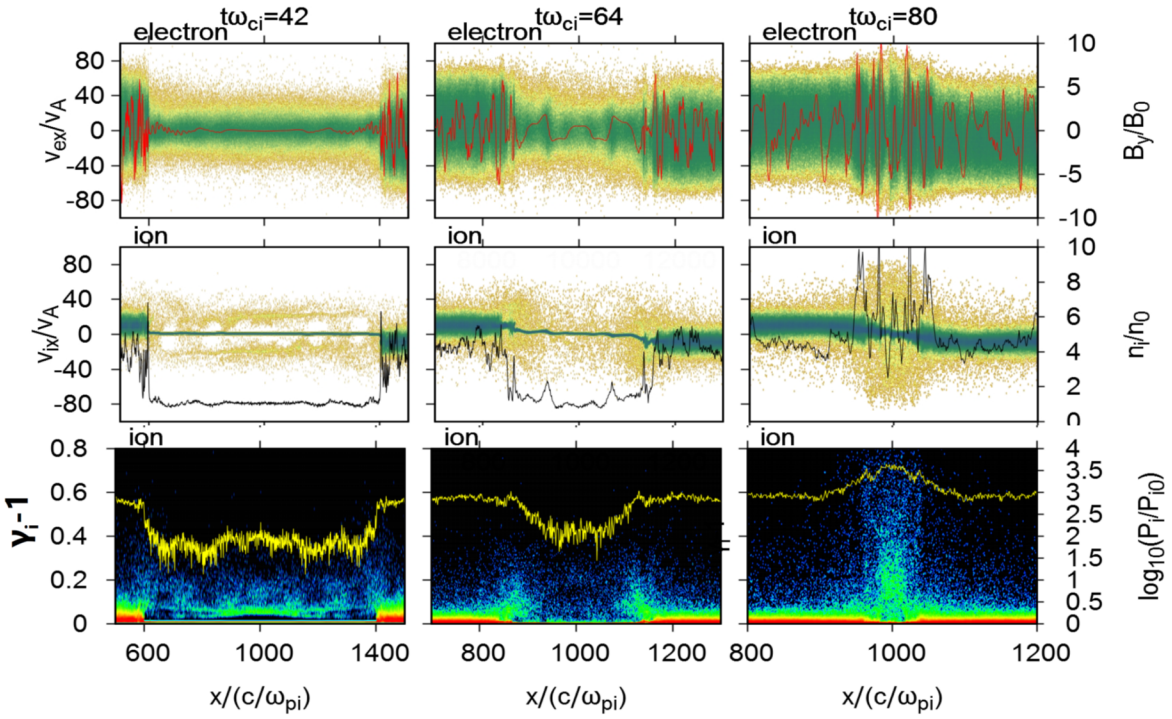


Figure 3.26: Top panels: the electron phase space density of v_x and the magnetic field B_y. Middle panels: the ion phase space density of v_x and the plasma density. Bottom panels: the ion phase density of ion energy and the ion pressure.

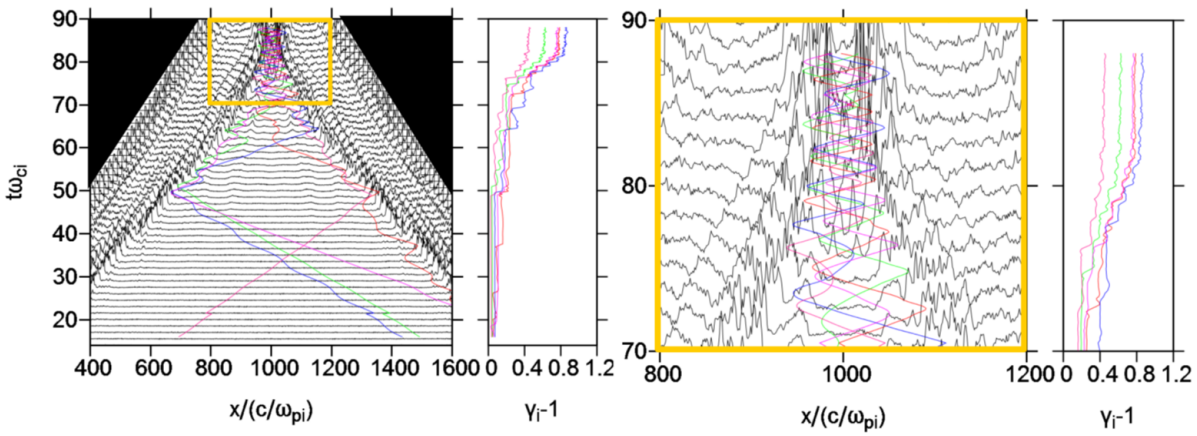


Figure 3.27: Ion trajectories on the space-time evolution of the plasma density and the time evolution of the ion energy. Orange box shows the enlarged view.

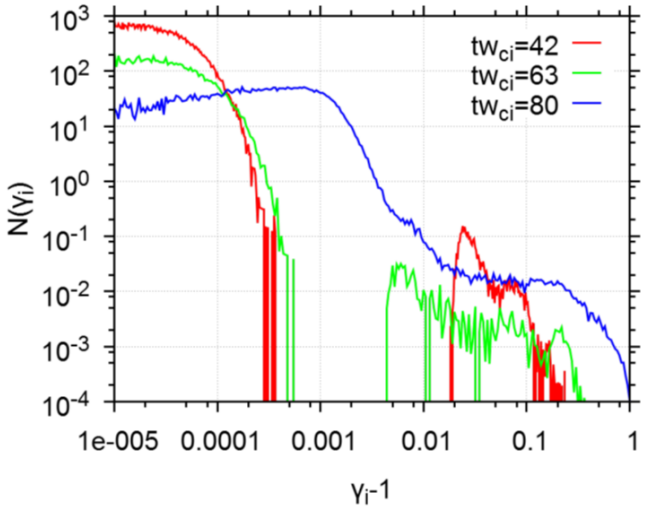


Figure 3.28: Ion energy spectrum between the two shocks for three times ($t\omega_{ci} = 42, t\omega_{ci} = 63$ and $t\omega_{ci} = 80$).

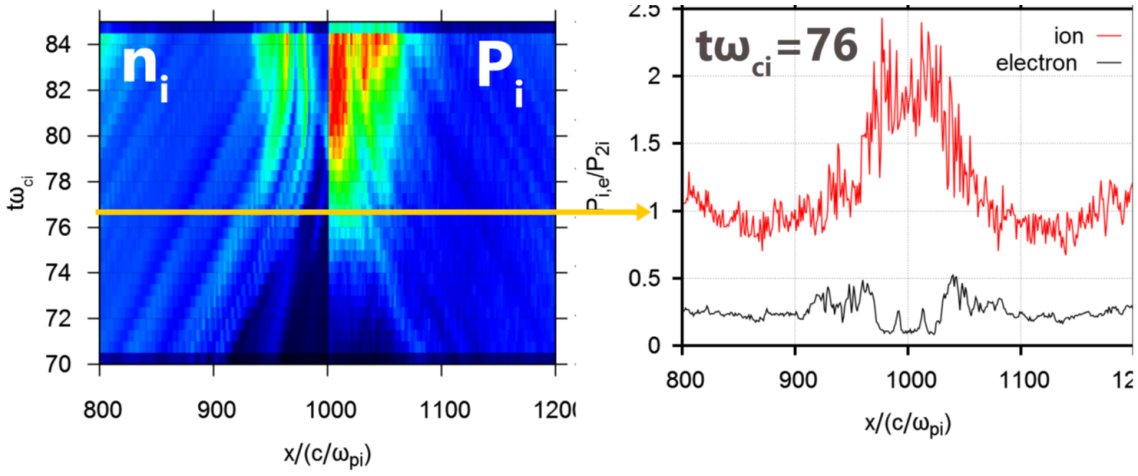


Figure 3.29: Left panel: the time-space evolution of the ion density (left side) and the ion pressure (right side). Right panel: the profile of the ion and electron pressure at $t\omega_{ci} = 76$.

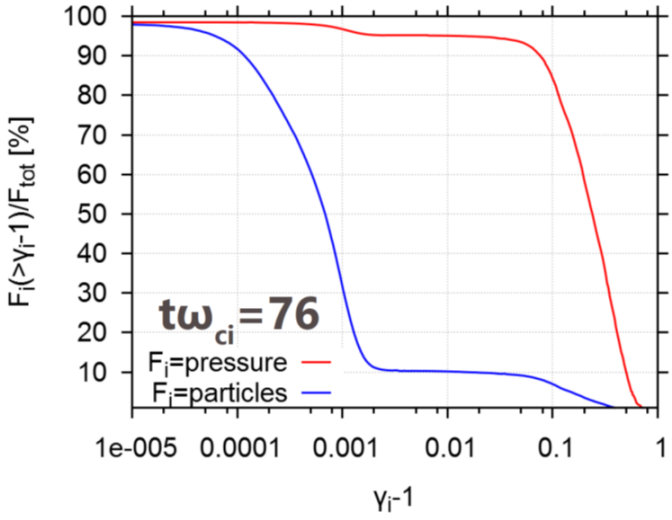


Figure 3.30: Cumulative spectra for the number of ions and the ion pressure.

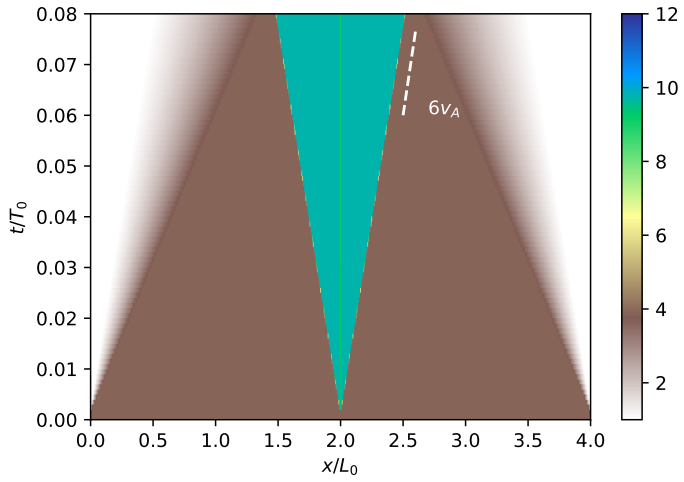


Figure 3.31: Time-space evolution of the density in the case without energetic ions. The density is normalized by the upstream density before the collision.

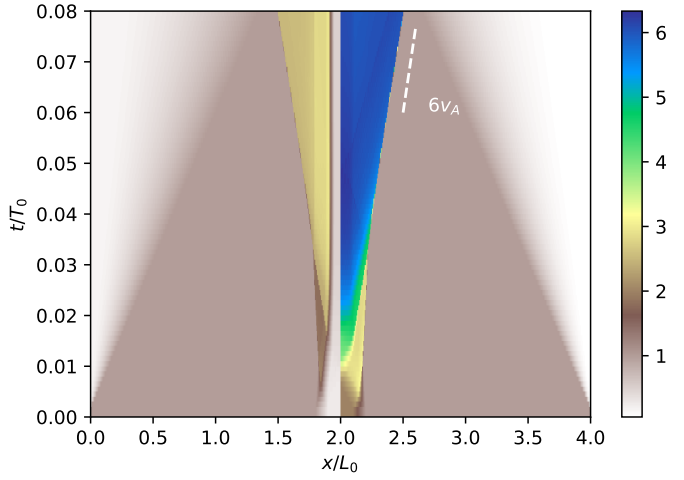


Figure 3.32: Time-space evolution of the density (left-side) and the pressure (right-side) in the case with energetic ions. The density and pressure are normalized by ρ_L and P_L.

CHAPTER 4
IN-SITU OBSERVATION

We show an observational example of a shock-shock interaction by investigating data from spacecraft orbiting around the Earth. In this event, an interplanetary shock wave passed through Earth's magnetosphere. Especially, we focus on electron acceleration through the shock-shock interaction which has not been found ever before. The key point is that when the two shock waves approach with each other, electron flux increased and the electron pitch angle distribution formed a bi-directional distribution. This indicates that electrons are accelerated between the two shocks like Fermi-type acceleration. We suggest that the electron acceleration is much more effective than a single shock acceleration.

4.1 introduction

Electron acceleration at a collisionless shock wave in the Heliosphere has been intensively investigate using in-situ data from spacecraft, we have understood several things about electron acceleration. Electrons can be accelerated up to 100 keV by the Earth's bow shock [Anderson et al., 1979]. These electrons are produced due to the shock drift acceleration especially when the shock angle is nearly perpendicular. Although DSA for electrons would work for an IP shock [Shimada et al., 1999], there is no direct evidence DSA at the Earth's bow shock. The reason would be that the bow shock is in a low-Mach number regime. A relation between the Mach number and energetic electrons are investigated by Oka et al. [2006]. Nearly relativistic electrons are observed at a high Mach number shock [Masters et al., 2013].

Although we have in-situ evidences for electron acceleration at a shock wave, it does not mean that electrons are always accelerated. It is rather that a shock wave in the heliosphere which does not have high Mach number is not an efficient electron accelerator. At the

Earth's bow shock, the DSA has not been observed and the maximum electron energy reaches only up to several tens of keV. From a statistical study, roughly 80% cases have no electron acceleration ($38 \sim 53$ keV) for 168 IP shock crossings at ACE [Lario et al., 2003]. Also, in-situ observation has not found nearly relativistic electrons around an IP shock and the Earth's bow shock. We can say that the Earth's bow shock and an IP shock itself does not always produce energetic electrons.

It has been verified that ion acceleration through a shock-shock interaction is effective. The first observation of a shock-shock interaction and the associated ion acceleration between an IP shock and the Earth's shock is investigate in the paper [Scholer and Ipavich, 1983]. They observed a peak-like enhancement of ion flux ranging $30 \sim 157$ keV from ISEE-1 which was close to the bow shock when the IP shock crossed ISEE-1. They, however, did not observe the same enhancement at ISEE-3 when the IP shock crossing. They concluded that the enhancement was due to re-acceleration by the bow shock. Hietala et al. [2011] finds another shock-shock interaction ion acceleration between an IP shock and the bow shock. In this report, Wind spacecraft observed gradual increasing ion flux when the IP shock approached to the bow shock. According to their interpretation, these ions were accelerated by multiple reflections between the two shock fronts. This is interpreted as the Fermi acceleration [Fermi, 1949].

This question is naturally raised, "are electrons also accelerated through a shock-shock interaction?" If it is so, it would be important for our understanding to energetic electrons in the Heliosphere. As we mentioned, an IP shock and Earth's bow shock itself are not necessarily an efficient accelerator for electrons. If a shock-shock interaction produces high energetic electrons much more efficient than a single shock, it supports an electron acceleration through a shock-shock interaction in astrophysical objects. Therefore, to answer this question would be critical to understand energetic electrons in space.

Our answer for this question is yes.

4.2 Overview of the Event

The data, from three spacecraft: ACE, Wind, and CLUSTER, were obtained on January 20 and 21, 2005. At the time ACE and Wind were positioned near the Lagrangian point L1, and CLUSTER were in front of the Earth's bow shock. In the morning of January 20, 2005, a solar flare (class X7.1) was observed by GOES, RHESSI, SOHO, TRACE and other satellites [Arkhangelskaja et al., 2005]. An IP shock associated with the CME of the solar flare propagated toward the Earth. Fig. 4.1 shows that the time profile of the magnitude of the magnetic field by Wind, ACE, and CLUSTER from the top to the bottom. The IP shock was observed from Wind, ACE, to CLUSTER in order around 16:00:00 UT on January 21. It is noted that CLUSTER passed the Earth's bow shock after 05:00:00 UT. The inter-spacecraft distance of CLUSTER had been with in a few ion-skin depth.

The upstream plasma parameters are calculated from the data of ACE. We averaged density, temperature, and the strength of the magnetic field from the data of SWEPAM from15:30:00 to 16:30:00 UT. The averaged density, temperature, and strength of the magnetic field are $4.258\mathrm{cm}^{-3}$, $10.12\mathrm{eV}$, and $4.962\mathrm{nT}$, respectively. From these data, we can construct the beta and Alfvén speed as 0.7047 and $52.87\mathrm{km/s}$ The averaged plasma speed is about $600\mathrm{km/s}$.

The shock parameters can be also obtained. The speed of the IP shock is calculated by the four spacecraft timing method using four spacecraft of CLUSTER [Russell et al., 1983]. We get the shock speed as $910\mathrm{km/s}$. The shock normal is also produced by the method and it is $(\mathrm{n_x}, \mathrm{n_y}, \mathrm{n_z}) \sim (-0.95, -0.29, -0.082)$ in the GSE coordinate. Using the same method, the speed of the bow shock is obtained as $73\mathrm{km/s}$. The Mach number of the IP shock and the bow shock are about 6 and 13, respectively. The Mach number of the IP shock is almost corresponded with the previous study [Du et al., 2008]. We use the Farris model to describe the bow shock [Farris and Russell, 1994].

4.3 Electron acceleration

Next we discuss electron flux taken from ACE, Wind, and CLUSTER. Each spacecraft has instruments to measure electron flux. We use EPAM for ACE, 3DP for Wind, and RAPID for CLUSTER.

ACE and Wind observed spike-type electron flux. Fig. 4.3 shows electron flux for four channels from 38 to 175 keV. Fig. 4.4 also shows electron flux for six channels from 27 to 516 keV observed by Wind. For ACE, before the IP shock crossing, the electron flux is gradually decreasing and we can see an rapid enhancement at the shock crossing. It is interpreted as the result of SDA. For Wind, the electron flux is gradually increasing from three hour ago before the shock crossing in the lowest channel. For other channels (40 to 181 keV) is gradually decreasing and an flux enhancement is not clear at the shock crossing. It is thought that the higher channels are contaminated by energetic ions.

On the other hand, the electron flux of CLUSTER is clearly different with the ones from ACE and Wind. Fig. 4.5 shows electron flux for six channels from 39 to 244 keV. While the electron flux is decreasing until 12:00:00 UT, it is gradually increasing after that time for all channels. Especially, one hour ago before the shock crossing, the slope of the electron flux becomes larger. After the shock crossing, the flux rapidly decreases. It is worth note that when the bow shock crosses CLUSTER, the electron flux do not change. Fig. 4.6 shows the pitch angle distribution of the electron flux which is integrated over all of the channels. It indicates a bi-directional pith angle distribution.

4.4 How are electrons accelerated?

We discuss the origin of the electron flux observed at CLUSTER. There are four possible sources for the electron flux. One of them is from the inside of the magnetosphere. The second is that the IP shock only accelerated electrons. The third is that the Earth's bow shock only accelerated electrons. The last one is that both the IP shock and the Earth's bow

shock accelerated electrons collaboratively.

The first idea could be removed from candidates. It is said that if an AE index is much more than 200 nT, geomagnetic activity is high and a substorm would occur. Energetic electrons produced by the substorm can leak to the foreshock and a spacecraft observe such electrons [Krimigis et al., 1978, Sarris et al., 1987]. In our event, the AE index is about 200 nT. Therefore, energetic electrons could be produced. It is, however, usually that leaked electrons create anisotropic pitch angle distribution. Our case is not in that case. Therefore we exclude this candidate as the origin of energetic electrons in our event.

The second idea is questionable as the origin of the electron flux. At the first, we can not explain why ACE and Wind did not observed such gradually increasing electron flux in the channels of hundreds of keV. Because IP shocks are almost planar, accelerated particles can be observed anywhere upstream [Ho et al., 2005] At the second point, there is no effective waves to scatter electrons. The root mean square (RMS) of the magnetic field is calculated from ACE,

$$\eta^{1/2} = \delta B/B_0 \sim 0.056. \tag{4.1}$$

Assuming the Bohm diffusion for electrons whose energy is 37 keV, we can find the diffusion coefficient and the diffusion length,

$$D = \eta \frac{v}{3} \frac{m_e v}{eB} \sim 2.72 \times 10^9 \ \left[\mathrm{km^2/s}\right], \tag{4.2}$$

$$\lambda = \frac{D}{u_1} \sim 7000 \ [\mathrm{R_E}], \tag{4.3}$$

where u_1 is the upstream plasma flow speed. On the other hand, we can obtain the diffusion length from Fig. 4.5 by assuming that the DSA produces the electron flux. It is about $\lambda_{data} \sim 630[\mathrm{R_E}]$. There is a big difference between the theory and the data. At the last point, a pitch angle distribution would be isotropic from the DSA theory. The data appears to be bi-directional. In conclusion, the IP shock itself did not produce energetic electrons.

The third one is also cast doubt. At the first point, CLUSTER spacecraft did not observe

such gradual increasing electron flux when crossing the bow shock around 05:00:00 UT (the IP shock was far away from the Earth). At the second point, if we assume that the DSA at the bow shock provided such energetic electrons, the bow shock must have approached because CLUSTER spacecraft went away from the bow shock. The bow shock, however, does not look to move. Fig. 4.7 indicates the shock standoff distance calculated from the equation,

$$R = \frac{C}{P_{ram}^{1/6}} \left(1 + \frac{1.1}{r}\right), \tag{4.4}$$

where C is the constant whose value is 11.8, P_{ram} is the ram pressure, and r is the compression ratio, respectively [Meziane et al., 2015]. From the figure, the shock standoff distance does not change to explain the observed shape of the flux. At the last point, according to the paper [Amano and Hoshino, 2010], the condition of the electron injection to the DSA is described as follows,

$$M_A > \frac{\cos\theta_{Bn}}{2}\sqrt{\frac{m_i}{m_e}\beta_e}. \tag{4.5}$$

Using the parameters in our event, M_A must exceed 18. However, the Mach number of the bow shock is less than this condition. Finally, we exclude this possibility that the bow shock accelerated electrons.

The last one is reasonable to explain the electron flux. If we assume that electrons are accelerated between the two shocks by multiple reflection at the shock front, a pitch angle distribution forms a bi-directional distribution. We can also why ACE and Wind did not observe such gradual increase electron flux. The reason why is that ACE and Wind are difficult to magnetically connect to the bow shock. It is guessed that electrons are run along the magnetic field. Therefore, since ACE and Wind are far away from the bow shock, a solid angle to be connected to the bow shock becomes small. On the other hand, because CLUSTER locate close to the bow shock, it is easy to be connected to the bow shock. We conclude that both the IP shock and the bow shock accelerated electrons collaboratively.

4.5 Comparison with the simulation results

In this section, we show that the pitch-angle distribution and the time-profile of electron flux observed in this event correspond to the simulation results.

Here, we use the simulation result of quasi-perpendicular case ($\theta_{Bn} = 60^{\circ}$). In this case, electrons are accelerated between the two shocks through multiple reflections at the shock waves. Therefore, this is an appropriate case to compare with the observational results. We measure electron flux and a pitch-angle distribution at the same point in the simulation space. It reflects that the speed of spacecraft are much less than the speed of an IP shock.

The top panel of Fig. shows the time evolution of a pitch-angle distribution obtained from the simulation performed in Chap. 2.3. We measured the pitch-angle distribution at the centre of the simulation space. It is clear that before the two shocks are far away, the electron flux forms a bi-directional distribution. As the two shocks approach, the bi-directional distribution becomes isotropic. It corresponds to the observational result in Fig. 4.6.

The bottom panel of Fig. **??** shows the time evolution of electron flux obtained from the same simulation. The important point from the figure is that an exponential-type flux has been produced. That is also seen in the observational result in Fig. 4.5 before the shock passage. Although an exponential-type flux can be seen from the DSA theory, we confirm that an exponential-type flux can produced in shock-shock interaction. Comparing with the simulation results, the electron acceleration of this 21-01-2005 event is understand due to shock-shock interaction.

Figures

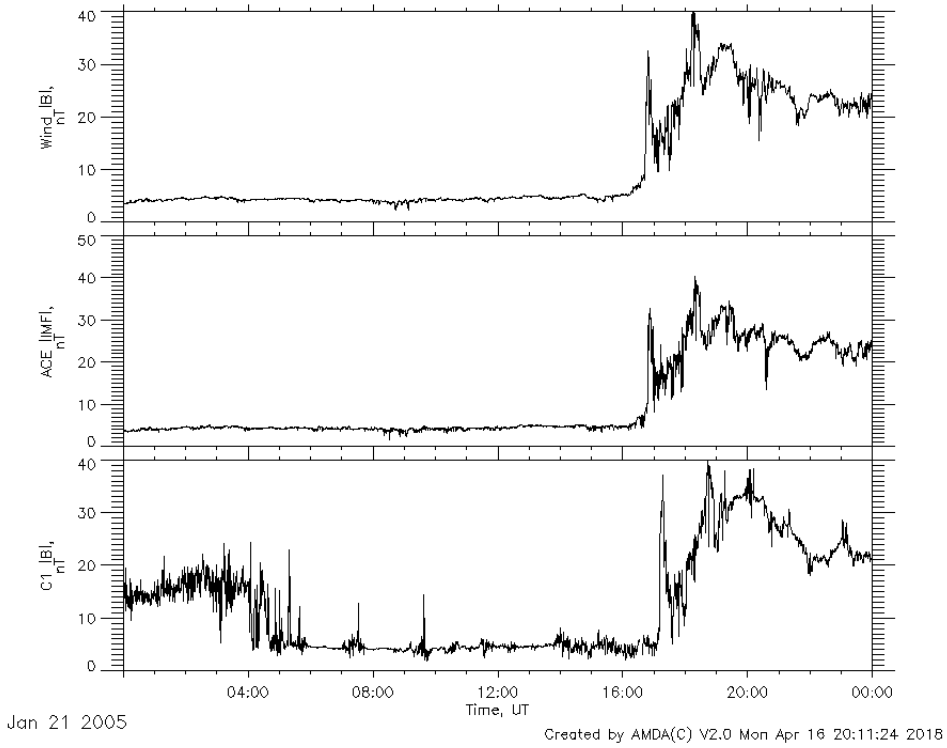


Figure 4.1: Time profile of magnitude of the magnetic field measured on Wind, ACE, and CLUSTER 1 from the top to the bottom. This plot is created by AMDA

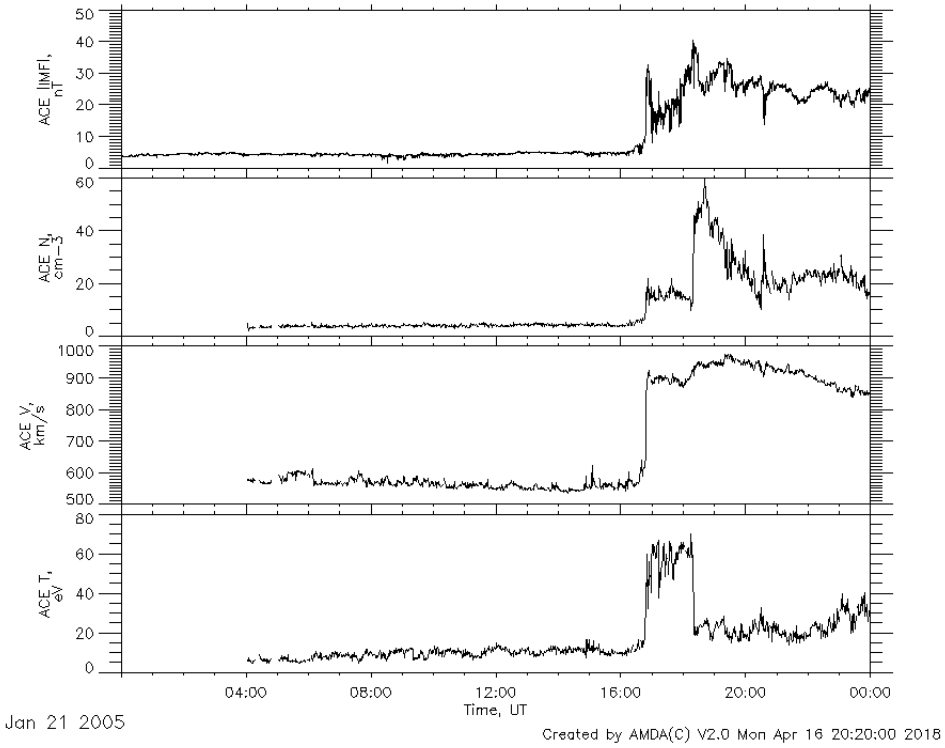


Figure 4.2: Time profile of magnitude of the magnetic field, density, bulk velocity, and radial component of the temperature. This plot is created by AMDA

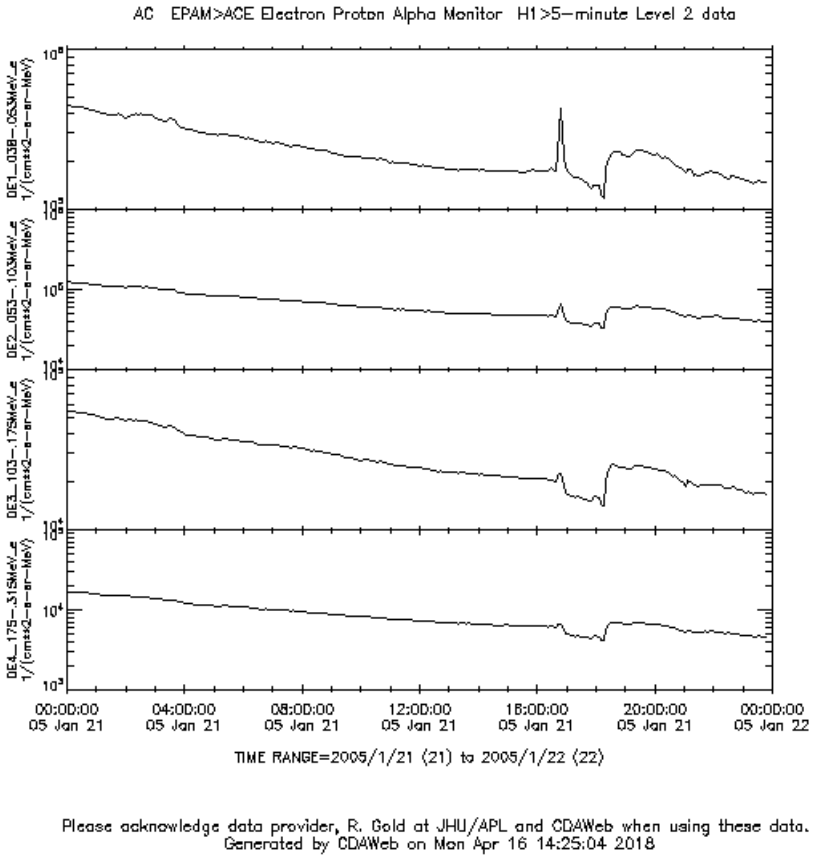


Figure 4.3: Electron flux measured on EPAM of ACE averaged in 5 minutes. This plot is created by CDAWeb.

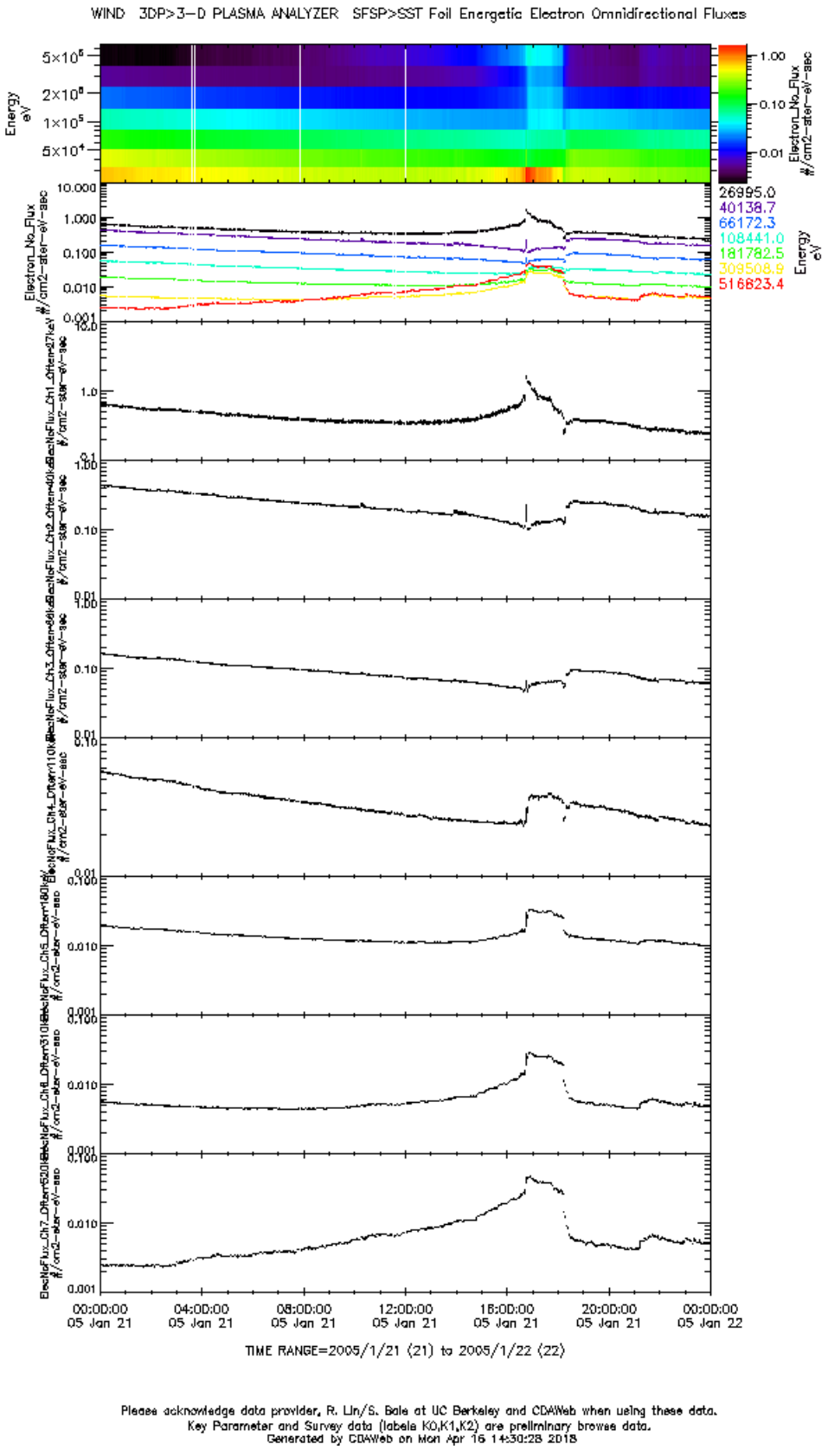


Figure 4.4: Electron number flux 27 keV to 520 keV as a function of energy in 7 channels. Top panel: spectrogram. Second: as stacked plot. Third to ninth panels: time-varying energies in 7 channels. This plot is created by CDAWeb.

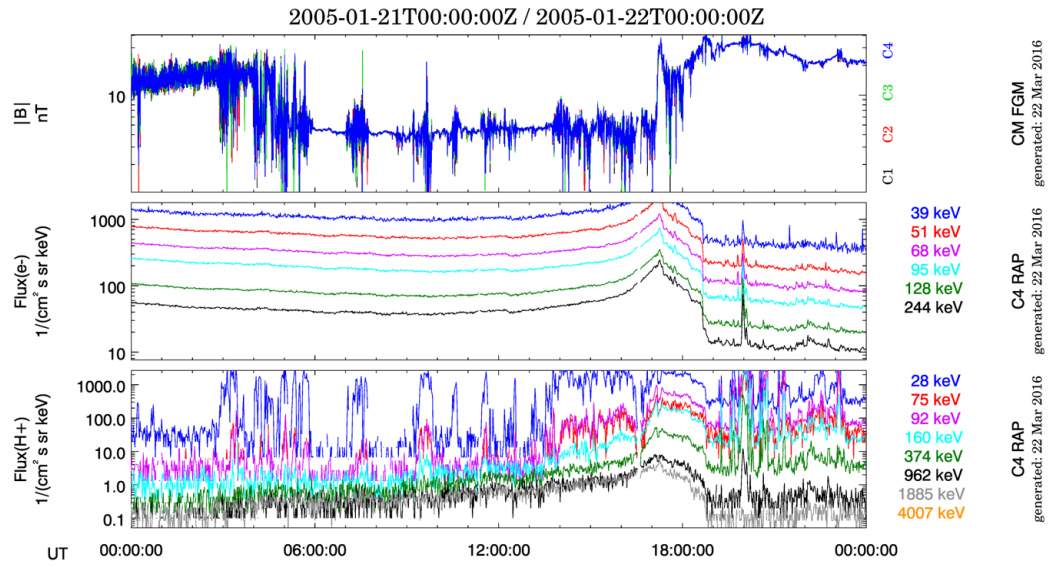


Figure 4.5: Top panel: the magnitude of the magnetic field. Middle panel: electron flux for six channels from $39 \sim 244$ keV. Bottom panel: ion flux for eight channels from $28 \sim 4007$ keV. This plot is created by CSA.

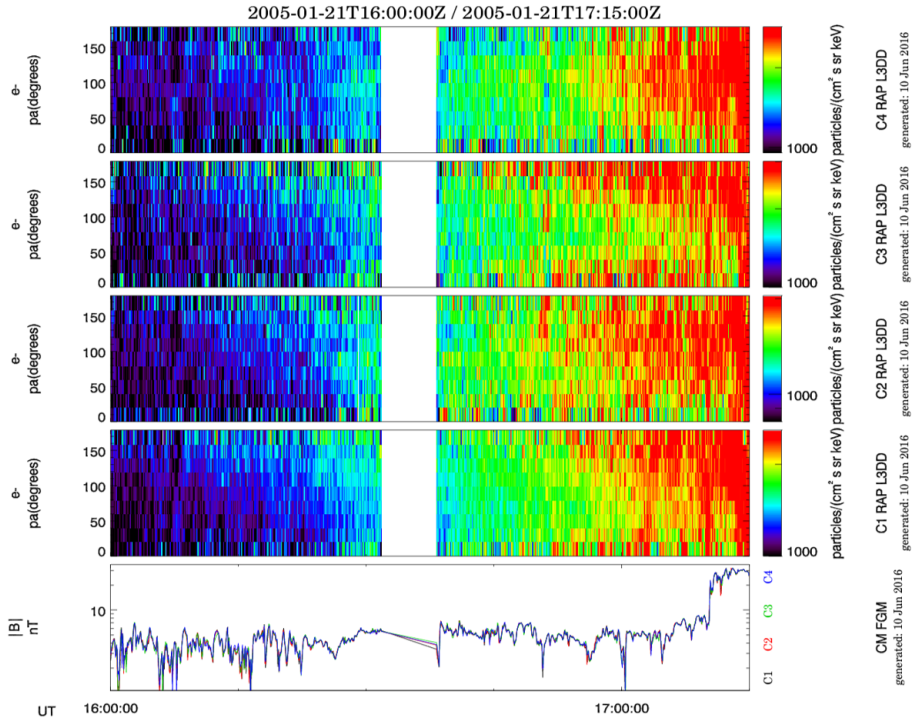


Figure 4.6: Pitch angle distribution of electrons. This plot is created by CSA.

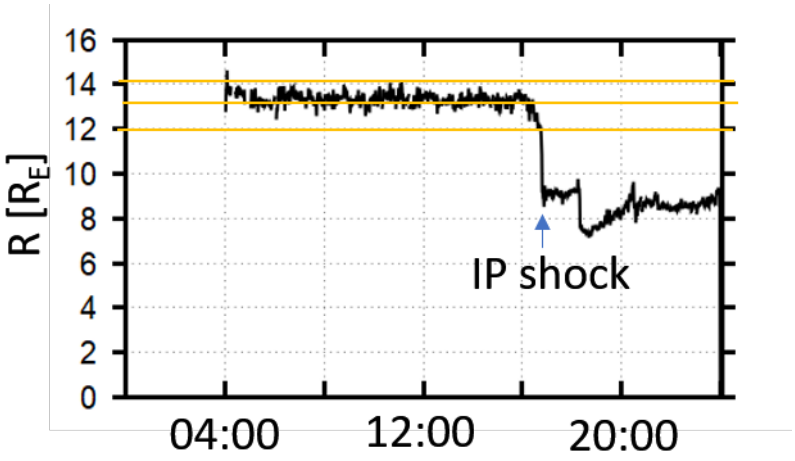


Figure 4.7: Standoff distance calculated from the solar wind ram pressure.

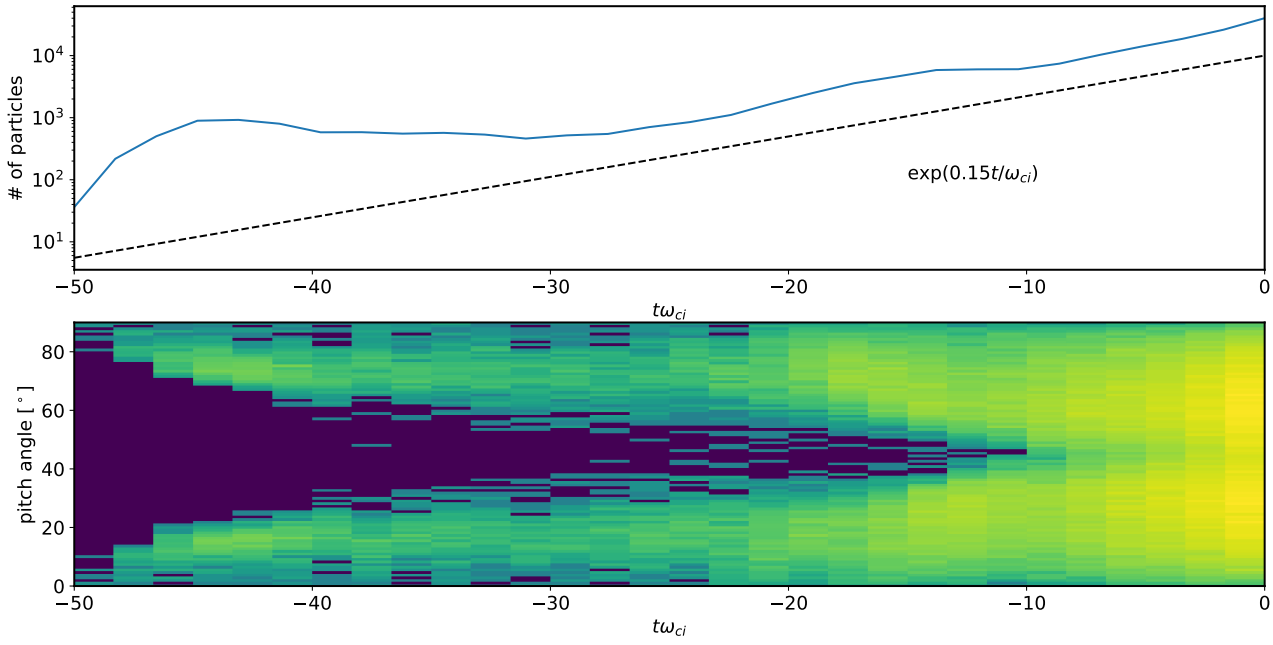


Figure 4.8: Top panel: the time evolution of the number of electrons at the center of the simulation box. Bottom panel: the time evolution of the electron pitch angle distribution at the center of the simulation box.

CHAPTER 5
CONCLUSIONS AND OUTLOOK

In this thesis we have mainly addressed a particle acceleration of shock-shock interaction. Several situations predicted for shock-shock interaction are considered in this thesis. The methods has been the usage of a test-particle simulation, a full PIC simulation, and in-situ measurements. There has been three main topics to verify that shock-shock interaction can produce particles more energetic than particles accelerated by single shock.

The first topic revealed that stationary two shocks system has a potential to produce energetic particles over the limitation of the strongest single shock. We use a test particle simulation in which there are two hydrodynamic shock waves and particles move randomly around the shock waves. The random motion of particles assumes large-angle scattering by isotropic turbulence. The simulation produces double power-law energy spectrum which has the index corresponding to the single shock in a low energy range and the one corresponding to the ratio between Region 1 and Region 3 in a high energy range. The higher energy tail indicates that particles accelerated by the single shock become to have a large diffusion length extending over the distance of the two shock waves and they are accelerated between Region 1 and Region 3. We also utilize the diffusion convection equation and directory solve the equation by including two shock waves. Including the velocity dependence of the spatial diffusion coefficient, we can reproduce the double power-law spectrum. This supports the result of the test particle simulation. We pointed that the diffusion coefficient has to be treated with a velocity dependence when considering a particle acceleration in shock-shock interaction.

In the second topic we investigated shock-shock interaction using a 1D full PIC simulation. Since full PIC simulations contain electron and ion scale dynamics, we can treat shock-shock interaction self-consistently. For a perpendicular case, the parameters of two

symmetric shock waves are $M_A = 8$ and $\beta_{i,e} = 0.5$. Since these shock waves are supercritical, the magnetic fields dynamically change at the collision. Some ions are accelerated at the collision. They are firstly reflected at the shock front due to the shock potential and then gyrate and pass through the downstream of the two shock waves. They gain energy about $10(m_i v_{sh}^2/2)$ in average. Here, m_i and $v_s h$ are the ion mass and the shock speed before the collision. Electrons are not accelerated like ions. They adiabatically gain energy at the collision site and are accelerated by the second Fermi acceleration after the collision. The parameters of the shock waves after the collision corresponds with the MHD prediction.

For a quasi-perpendicular case, electrons are especially accelerated. The two shock waves are $M_A = 13$ and $\beta = 0.5$. In this case, electrons are reflected from the shock front due to the SDA. Because the SDA are controlled by $1/\cos\theta_{Bn}$, electrons can gain large energy when the shock angle is close to 90°. These electrons reach the other shock and are possibly reflected again. In the PIC simulation, reflected electrons create the temperature anisotropy ($T_{e||} > T_{e\perp}$). This anisotropy excite waves called the firehose instability. The amplitude of the waves are about $0.5B_0$ where B_0 is the background magnetic field. We verify that accelerated electrons are scattered in the phase space due to the excited waves using a test particle simulation. This pitch-angle scattering leads a strong electron acceleration. If there are no large amplitude waves, multiply reflected electrons are tend to get inside the loss-cone of the shock waves because of the feature of the SDA. However, pitch-angle scattered electrons could get outside the loss-cone of the shock waves. Therefore there is no limit for the electron acceleration in principle. We find that these processes work for producing more and more energetic electrons in a shock-shock interaction system by means of a self-consistent manner.

For a quasi-parallel case, ions play an important role for shock-shock interaction. The shock waves are $M_A = 11$ and $\beta = 0.5$. Unlike the quasi-perpendicular shock case, ions can be escaped from the shock waves. These ions reach the other shock wave and are accelerated by the scatter-free ion acceleration Sugiyama and Terasawa [1999]. Accelerated

ions are trapped around the shock fronts before the collision. When the distance of the two shock waves are within one ion gyro radius, these ions gyrate between the two shock waves and gain energy by a way interpreted as the cyclotron acceleration which is used for a particle accelerator. Interestingly, these further accelerated ions have pressure larger than the pressure of the downstream. This causes the deceleration of the shock waves. We insist that it would be necessary to take into account the ion kinetic effects in the shock-shock interaction of two quasi-parallel shock waves. Actually, electrons are reflected due to the SDA. However, they gain less energy than the case of quasi-perpendicular shock.

The last point is an in-situ measurement of shock-shock interaction. We investigate an event occurred in 21-22, January 2005. An IP shock propagated toward to the Earth's bow shock. Several spacecraft (ACE, Wind, and CLUSTER) observed located between the two shocks and observe the IP shock passage. From the 4-spacecraft timing method by CLUSTER, the speed of the IP shock is about 900 km/s and of the Earth's bow shock is about 70 km/s. Measuring solar wind parameters from ACE, we determined the Mach number of the IP shock and the Earth's bow shock as 7 and 10, respectively. Surveying electron flux for each spacecraft, ACE and Wind observed almost the same electron flux feature. Before the passage of the IP shock, the electron flux was gradually decreasing and suddenly increased at the passage. This can be interpreted as the result of the SDA. On the other hand, CLUSTER observed gradually increasing electron flux from one hour and half ago for all channels ($39 \sim 244$ keV). This is because while ACE and Wind are not connected to both the IP shock and the Earth's bow shock, CLUSTER are easily connected to both. Electrons traveled between the two shocks and gained energy by Fermi acceleration. A bi-directional pitch angle distribution supports this idea. We note that the IP shock and the Earth's bow shock each itself did not have a potential to accelerate nearly relativistic electrons. However, when two shock waves locate in close region, these two shocks could accelerate electrons up to nearly relativistic regime.

To investigate shock-shock interaction between an IP shock and the termination shock,

we can add pick-up ions in the full PIC simulation. The interaction has been observed by Voyager-1 [Gurnett et al., 2013]. It is believed that pick-up ions controlled the structure of the termination shock [Matsukiyo and Scholer, 2014]. Because they have large gyro radius, when the two shocks approach, pick-up ions are favorably accelerated comparing with background ions. These accelerated pick-ions may modify the shock structurer right before and after the collision.

While we investigate shock-shock interaction whose geometry is always parallel for the two shock fronts, it happens that two shock waves have a certain angle between the shock fronts. As we have seen, particles are efficiently accelerated when the two shocks collide. Therefore, in a case that the intersection always exists, particles are constantly accelerated at the intersection. This situation takes place in, for example, a CME-CIR interaction.

To perform a global simulation including an IP shock is also an interesting topic. Global simulations containing kinetic effects would be a forefront topic in the plasm physics. An interaction between an IP shock and a magnetosphere like the Earth's magnetosphere is not only interested for the point of view from shock-shock interaction but also for geo-magnetic activity. Since we have known that kinetic effects (energetic ions) could modify shock structures, it is expected that shock waves are altered and change geo-magnetic activity from an MHD prediction.

Finally, we advocate to investigate shock-shock interaction using a laser experiment. Recently, collisionless shock waves produced in a laser-experiment has been extensively researched. For electrostatic shocks, shock-shock interaction has been investigated Morita et al. [2013]. Shock-shock interaction of magnetized shocks has not yet been investigated and is highly interested. If there are two shock waves and particle acceleration discussed above takes place, a strong emission could go off. Because it is not different to detect a strong emission, a laser experiment gives us plentiful information. We can also access to the overall structure which cannot be addressed by in-situ observation.

Appendices

APPENDIX A

FULL PARTICLE-IN-CELL SIMULATION

Here, we introduce a general idea about full PIC simulation and a method for the experiment of a two-shocks collision.

Full PIC simulation is the first principle calculation of collisionless plasma. The simulation is equivalent to solve the velocity distribution function of ions and electrons in the Vlasov-Maxwell system. Due to fully account the particle velocity distributions, the simulation is able to capture the electron and ion kinetic effects self-consistently. It is also that non-thermal particles are solved correctly.

Another method to solve the Vlasov-Maxwell system numerically is Vlasov simulations. This method makes the level of numerical noises level. However, it requires huge memory size. On the other hand, full PIC simulation treats ions and electrons as super-particle which can be regarded as a represented particle in a space-velocity distribution function. The super particles are moved by the equation of motion which is written as

$$m\frac{\mathrm{d}\mathbf{u}}{\mathrm{d}t} = q\left(\mathbf{E} + \frac{\mathbf{u}}{c\gamma} \times \mathbf{B}\right), \tag{A.1}$$

where m is the rest mass, q is the charge, $\mathbf{u}$ is the four-velocity, γ is the Lorentz factor defined by $\gamma = \sqrt{1 + u^2/c^2}$. Here c is the speed of light. Although there are several methods to numerically solve the equation of motion, we adopt the Bunemann-Boris method in our simulation [Boris, 1970], which accurately conserves particle energy. In the method, the equation of motion is rewritten in a discrete from

$$\frac{\mathbf{u}^{n+1/2} - \mathbf{u}^{n-1/2}}{\Delta t} = \frac{q}{m}\left(\mathbf{E}^n + \frac{\mathbf{u}^n}{c\gamma^n} \times \mathbf{B}^n\right). \tag{A.2}$$

Defining $\mathbf{u}^-$ and $\mathbf{u}^+$ as follows,

$$\mathbf{u}^- = \mathbf{u}^{n-1/2} + \frac{q}{m}\frac{\Delta t}{2}\mathbf{E}^n, \tag{A.3}$$

$$\mathbf{u}^+ = \mathbf{u}^{n+1/2} - \frac{q}{m}\frac{\Delta t}{2}\mathbf{E}^n. \tag{A.4}$$

The equation A.2 is rewritten,

$$\frac{\mathbf{u}^+ - \mathbf{u}^-}{\Delta t} = \frac{q}{2\gamma^n mc}\left(\mathbf{u}^+ + \mathbf{u}^-\right) \times \mathbf{B}^n. \tag{A.5}$$

The equation means a rotation by $\mathbf{B}$. The equation (A.2) is proceeded by three steps, first: $\mathbf{E}$ acceleration for a half time step $\Delta t/2$, second: a rotation by $\mathbf{B}$, third: $\mathbf{E}$ acceleration for a half time step $\Delta t/2$. The first step is expressed as

$$\mathbf{u}^- = \mathbf{u}^{n-1/2} + \frac{q}{m}\mathbf{E}^n\frac{\Delta t}{2}. \tag{A.6}$$

The second step is the rotation, which denotes

$$\mathbf{u}^* = \mathbf{u}^- + \mathbf{u}^- \times \mathbf{T}, \tag{A.7}$$

$$\mathbf{u}^+ = \mathbf{u}^- + \mathbf{u}^* \times \mathbf{S}, \tag{A.8}$$

where

$$\mathbf{T} = \frac{q\mathbf{B}^n}{m\gamma^- c}\frac{\Delta t}{2}, \tag{A.9}$$

$$\mathbf{S} = \frac{2\mathbf{T}}{1+T^2}. \tag{A.10}$$

The last step is

$$\mathbf{u}^{n+1/2} = \mathbf{u}^+ + \frac{q}{m}\mathbf{E}^n\frac{\Delta t}{2}. \tag{A.11}$$

The update of a particle position is calculated as follows

$$\mathbf{x}^{n+1} = \mathbf{x}^n + \frac{\mathbf{u}^{n+1/2}}{\gamma^{1+1/2}}\Delta t. \tag{A.12}$$

Next, we consider how to solve Maxwell equations. Here, we assume the electromagnetic fields are only dependent on the x-axis. From the solenoidal condition in Maxwell equations, B_x is constant. The x-component of the electric fields is separated from other component and is given by the Poisson equation and Faraday's law. The remaining equations are written as

$$\frac{1}{c}\frac{\partial E_y}{\partial t} = -\frac{4\pi}{c}j_y - \frac{\partial B_z}{\partial x}, \tag{A.13}$$
$$\frac{1}{c}\frac{\partial B_z}{\partial t} = -\frac{\partial E_y}{\partial x}, \tag{A.14}$$
$$\frac{1}{c}\frac{\partial E_z}{\partial t} = -\frac{4\pi}{c}j_z + \frac{\partial B_y}{\partial x}, \tag{A.15}$$
$$\frac{1}{c}\frac{\partial B_y}{\partial t} = \frac{\partial E_z}{\partial x}. \tag{A.16}$$

Defining $F^{\pm} \equiv E_y \pm B_z$ and $G^{\pm} \equiv E_z \pm B_y$, The equations above are summarized as

$$\frac{1}{c}\left(\frac{\partial}{\partial t} \pm \frac{\partial}{\partial x}\right) F^{\pm} = -\frac{4\pi}{c}J_y, \tag{A.17}$$
$$\frac{1}{c}\left(\frac{\partial}{\partial t} \mp \frac{\partial}{\partial x}\right) G^{\pm} = -\frac{4\pi}{c}J_z. \tag{A.18}$$

These discrete forms to advance $F^{\pm}$ and $G^{\pm}$ are written as

$$\frac{(F^+)_i^{n+1} - (F^+)_i^n}{c\Delta t} + \frac{(F^+)_i^n - (F^+)_{i-1}^n}{\Delta x} = -\frac{4\pi}{c}\left(J_y\right)_{i-1/2}^{n+1/2}, \tag{A.19}$$
$$\frac{(F^-)_i^{n+1} - (F^-)_i^n}{c\Delta t} - \frac{(F^-)_{i+1}^n - (F^-)_i^n}{\Delta x} = -\frac{4\pi}{c}\left(J_y\right)_{i+1/2}^{n+1/2}, \tag{A.20}$$
$$\frac{(G^+)_i^{n+1} - (G^+)_i^n}{c\Delta t} - \frac{(G^+)_i^n - (G^+)_{i-1}^n}{\Delta x} = -\frac{4\pi}{c}\left(J_z\right)_{i-1/2}^{n+1/2}, \tag{A.21}$$
$$\frac{(G^-)_i^{n+1} - (G^-)_i^n}{c\Delta t} + \frac{(G^-)_{i+1}^n - (G^-)_i^n}{\Delta x} = -\frac{4\pi}{c}\left(J_z\right)_{i+1/2}^{n+1/2}. \tag{A.22}$$

We progress $F^{\pm}$ and $G^{\pm}$ for a time step and they are converted into the electromagnetic fields,

$$E_y = \frac{1}{2}\left(F^+ + F^-\right), \tag{A.23}$$

$$B_z = \frac{1}{2}\left(F^+ - F^-\right), \tag{A.24}$$

$$E_z = \frac{1}{2}\left(G^+ + G^-\right), \tag{A.25}$$

$$B_y = \frac{1}{2}\left(G^+ - G^-\right). \tag{A.26}$$

The electrostatic field E_x is solved by the x-component of Faraday's law,

$$\frac{\partial E_x}{\partial t} = 4\pi j_x. \tag{A.27}$$

Because we calculate the charge density and the current density independently, the charge conservation law is not always satisfied. Therefore, we apply the Poisson's equation to correct errors.

Finally, we explain a method of the interpolation grids and particles. While physical parameters (density, current densities, and electromagnetic fields) are defined on grids, particles can freely move in the simulation space. Therefore we need an interpolation method to define density and current densities and to interpolate the electromagnetic fields on particles. In our simulation, we introduce a simple linear interpolation which is called the cloud-in-cell method. Although there is a higher order interpolation method, the computational costs increase. There would be a trade-off between an accuracy and costs.

BIBLIOGRAPHY

A. Achterberg. The energy spectrum of electrons accelerated by weak magnetohydrodynamic turbulence. AAP, 76:276–286, July 1979.

M. Ackermann, M. Ajello, A. Allafort, L. Baldini, J. Ballet, G. Barbiellini, M. G. Baring, D. Bastieri, K. Bechtol, R. Bellazzini, R. D. Blandford, E. D. Bloom, E. Bonamente, A. W. Borgland, E. Bottacini, T. J. Brandt, J. Bregeon, M. Brigida, P. Bruel, R. Buehler, G. Busetto, S. Buson, G. A. Caliandro, R. A. Cameron, P. A. Caraveo, J. M. Casandjian, C. Cecchi, Ö. Çelik, E. Charles, S. Chaty, R. C. G. Chaves, A. Chekhtman, C. C. Cheung, J. Chiang, G. Chiaro, A. N. Cillis, S. Ciprini, R. Claus, J. Cohen-Tanugi, L. R. Cominsky, J. Conrad, S. Corbel, S. Cutini, F. D'Ammando, A. de Angelis, F. de Palma, C. D. Dermer, E. do Couto e Silva, P. S. Drell, A. Drlica-Wagner, L. Falletti, C. Favuzzi, E. C. Ferrara, A. Franckowiak, Y. Fukazawa, S. Funk, P. Fusco, F. Gargano, S. Germani, N. Giglietto, P. Giommi, F. Giordano, M. Giroletti, T. Glanzman, G. Godfrey, I. A. Grenier, M.-H. Grondin, J. E. Grove, S. Guiriec, D. Hadasch, Y. Hanabata, A. K. Harding, M. Hayashida, K. Hayashi, E. Hays, J. W. Hewitt, A. B. Hill, R. E. Hughes, M. S. Jackson, T. Jogler, G. Jóhannesson, A. S. Johnson, T. Kamae, J. Kataoka, J. Katsuta, J. Knödlseder, M. Kuss, J. Lande, S. Larsson, L. Latronico, M. Lemoine-Goumard, F. Longo, F. Loparco, M. N. Lovellette, P. Lubrano, G. M. Madejski, F. Massaro, M. Mayer, M. N. Mazziotta, J. E. McEnery, J. Mehault, P. F. Michelson, R. P. Mignani, W. Mitthumsiri, T. Mizuno, A. A. Moiseev, M. E. Monzani, A. Morselli, I. V. Moskalenko, S. Murgia, T. Nakamori, R. Nemmen, E. Nuss, M. Ohno, T. Ohsugi, N. Omodei, M. Orienti, E. Orlando, J. F. Ormes, D. Paneque, J. S. Perkins, M. Pesce-Rollins, F. Piron, G. Pivato, S. Rainò, R. Rando, M. Razzano, S. Razzaque, A. Reimer, O. Reimer, S. Ritz, C. Romoli, M. Sánchez-Conde, A. Schulz, C. Sgrò, P. E. Simeon, E. J. Siskind, D. A. Smith, G. Spandre, P. Spinelli, F. W. Stecker, A. W. Strong, D. J. Suson, H. Tajima, H. Takahashi, T. Takahashi, T. Tanaka, J. G. Thayer, J. B. Thayer, D. J. Thompson, S. E. Thorsett, L. Tibaldo, O. Tibolla, M. Tinivella, E. Troja, Y. Uchiyama, T. L. Usher, J. Vandenbroucke, V. Vasileiou, G. Vianello, V. Vitale, A. P. Waite, M. Werner, B. L. Winer, K. S. Wood, M. Wood, R. Yamazaki, Z. Yang, and S. Zimmer. Detection of the characteristic pion-decay signature in supernova remnants. Science, 339(6121):807–811, 2013. ISSN 0036-8075. doi: 10.1126/science.1231160. URL http://science.sciencemag.org/content/339/6121/807.

T. Amano and M. Hoshino. Electron Shock Surfing Acceleration in Multidimensions: Two-Dimensional Particle-in-Cell Simulation of Collisionless Perpendicular Shock. ApJ, 690: 244–251, January 2009. doi: 10.1088/0004-637X/690/1/244.

Takanobu Amano and Masahiro Hoshino. A critical mach number for electron injection in collisionless shocks. Phys. Rev. Lett., 104:181102, May 2010. doi: 10.1103/PhysRevLett.104.181102. URL https://link.aps.org/doi/10.1103/PhysRevLett.104.181102.

KA Anderson, RP Lin, F Martel, CS Lin, GK Parks, and H Reme. Thin sheets of energetic electrons upstream from the earths bow shock. Geophysical Research Letters, 6(5):401–404, 1979.

I. V. Arkhangelskaja, A. I. Arkhangelskii, A. S. Glyanenko, Y. D. Kotov, and S. N. Kuznetsov. The Investigation of January 2005 Solar Flares Gamma-Emission by Avs-F Apparatus Data Onboard Coronas-F Satellite in 0.1-20 Mev Energy Band. In The Dynamic Sun: Challenges for Theory and Observations, volume 600 of ESA Special Publication, page 107.1, December 2005.

W. I. Axford, E. Leer, and G. Skadron. The acceleration of cosmic rays by shock waves. International Cosmic Ray Conference, 11:132–137, 1977.

L. Ball and D. B. Melrose. Shock Drift Acceleration of Electrons. PASA, 18:361–373, 2001. doi: 10.1071/AS01047.

André Balogh and Rudolf A Treumann. Physics of collisionless shocks: space plasma shock waves. Springer Science & Business Media, 2013.

Rico Behlke, Mats André, Stephan C Buchert, Andris Vaivads, Anders I Eriksson, Elizabeth A Lucek, and Andre Balogh. Multi-point electric field measurements of short large-amplitude magnetic structures (slams) at the earth's quasi-parallel bow shock. Geophysical research letters, 30(4), 2003.

A. R. Bell. The acceleration of cosmic rays in shock fronts. I. MNRAS, 182:147–156, January 1978. doi: 10.1093/mnras/182.2.147.

D. Biskamp and H. Welter. Structure of the Earth's bow shock. JGR, 77:6052, 1972. doi: 10.1029/JA077i031p06052.

R. Blandford, P. Simeon, and Y. Yuan. Cosmic Ray Origins: An Introduction. Nuclear Physics B Proceedings Supplements, 256:9–22, November 2014. doi: 10.1016/j.nuclphysbps.2014.10.002.

R. D. Blandford and J. P. Ostriker. Particle acceleration by astrophysical shocks. APJL, 221:L29–L32, April 1978. doi: 10.1086/182658.

Pasquale Blasi. The origin of galactic cosmic rays. The Astronomy and Astrophysics Review, 21(1):70, Nov 2013. ISSN 1432-0754. doi: 10.1007/s00159-013-0070-7. URL https://doi.org/10.1007/s00159-013-0070-7.

Jay P Boris. Relativistic plasma simulation-optimization of a hybrid code. In Proc. Fourth Conf. Num. Sim. Plasmas, Naval Res. Lab, Wash. DC, pages 3–67, 1970.

D. Burgess. Cyclic behavior at quasi-parallel collisionless shocks. GRL, 16:345–348, May 1989. doi: 10.1029/GL016i005p00345.

D. Burgess and M. Scholer. Shock front instability associated with reflected ions at the perpendicular shock. Physics of Plasmas, 14(1):012108–012108, January 2007. doi: 10.1063/1.2435317.

L. F. Burlaga and N. F. Ness. Compressible "Turbulence" Observed in the Heliosheath by Voyager 2. ApJ, 703:311–324, September 2009. doi: 10.1088/0004-637X/703/1/311.

A. M. Bykov, D. C. Ellison, P. E. Gladilin, and S. M. Osipov. Ultrahard spectra of PeV neutrinos from supernovae in compact star clusters. MNRAS, 453:113–121, October 2015. doi: 10.1093/mnras/stv1606.

P. J. Cargill. The formation of discontinuities as a result of shock collisions. JGR, 95: 20731–20741, December 1990. doi: 10.1029/JA095iA12p20731.

P. J. Cargill. Collisions between quasi-parallel shocks. Advances in Space Research, 11: 241–244, 1991a. doi: 10.1016/0273-1177(91)90040-Q.

P. J. Cargill. The interaction of collisionless shocks in astrophysical plasmas. ApJ, 376: 771–781, August 1991b. doi: 10.1086/170325.

P. J. Cargill, C. C. Goodrich, and K. Papadopoulos. Interaction of two collisionless shocks. Physical Review Letters, 56:1988–1991, May 1986. doi: 10.1103/PhysRevLett.56.1988.

G. F. Chew, M. L. Goldberger, and F. E. Low. The boltzmann equation an d the one-fluid hydromagnetic equations in the absence of particle collisions. Proceedings of the Royal Society of London A: Mathematical, Physical and Engineering Sciences, 236(1204): 112–118, 1956. ISSN 0080-4630. doi: 10.1098/rspa.1956.0116. URL http://rspa.royalsocietypublishing.org/content/236/1204/112.

R. Courant and K. O. Friedrichs. Supersonic flow and shock waves. 1948.

T.G. Cowling. Magnetohydrodynamics. Monographs on Astronomical Subjects. Hilger (Adam), 1976. ISBN 9780852743003. URL https://books.google.co.jp/books?id=6k1RAAAAMAAJ.

F. De Hoffmann and E. Teller. Magneto-hydrodynamic shocks. Phys. Rev., 80:692–703, Nov 1950. doi: 10.1103/PhysRev.80.692. URL https://link.aps.org/doi/10.1103/PhysRev.80.692.

L. O. '. Drury. Origin of cosmic rays. Astroparticle Physics, 39:52–60, December 2012. doi: 10.1016/j.astropartphys.2012.02.006.

L. O. Drury. An introduction to the theory of diffusive shock acceleration of energetic particles in tenuous plasmas. Reports on Progress in Physics, 46:973–1027, August 1983. doi: 10.1088/0034-4885/46/8/002.

L. O. Drury and S. A. E. G. Falle. On the Stability of Shocks Modified by Particle Acceleration. MNRAS, 223:353, November 1986. doi: 10.1093/mnras/223.2.353.

L. O. Drury and J. H. Voelk. Hydromagnetic shock structure in the presence of cosmic rays. apj, 248:344–351, 1981.

A. M. Du, B. T. Tsurutani, and W. Sun. Anomalous geomagnetic storm of 2122 january 2005: A storm main phase during northward imfs. Journal of Geophysical Research: Space Physics, 113(A10), 2008. doi: 10.1029/2008JA013284.

M. H. Farris and C. T. Russell. Determining the standoff distance of the bow shock: Mach number dependence and use of models. Journal of Geophysical Research: Space Physics, 99(A9):17681–17689, 1994. doi: 10.1029/94JA01020.

Enrico Fermi. On the origin of the cosmic radiation. Physical Review, 75(8):1169, 1949.

A.L. Fetter and J.D. Walecka. Theoretical Mechanics of Particles and Continua. McGraw-Hill: New York, 1980.

Y. A. Gallant, M. Hoshino, A. B. Langdon, J. Arons, and C. E. Max. Relativistic, perpendicular shocks in electron-positron plasmas. ApJ, 391:73–101, May 1992. doi: 10.1086/171326.

S. Peter Gary and Kazumi Nishimura. Resonant electron firehose instability: Particle-in-cell simulations. Physics of Plasmas, 10(9):3571–3576, 2003. doi: 10.1063/1.1590982. URL https://doi.org/10.1063/1.1590982.

J. Giacalone and D. Burgess. Interaction between inclined current sheets and the heliospheric termination shock. GRL, 37:L19104, October 2010. doi: 10.1029/2010GL044656.

J. Giacalone and J. R. Jokipii. Magnetic Field Amplification by Shocks in Turbulent Fluids. ApJL, 663:L41–L44, July 2007. doi: 10.1086/519994.

Joe Giacalone, Steven J Schwartz, and David Burgess. Observations of suprathermal ions in association with slams. Geophysical research letters, 20(2):149–152, 1993.

J. T. Gosling and A. E. Robson. Ion reflection, gyration, and dissipation at supercritical shocks. Washington DC American Geophysical Union Geophysical Monograph Series, 35:141–152, 1985. doi: 10.1029/GM035p0141.

J. T. Gosling and M. F. Thomsen. Specularly reflected ions, shock foot thicknesses, and shock velocity determinations in space. JGR, 90:9893–9896, October 1985. doi: 10.1029/JA090iA10p09893.

J. T. Gosling, J. R. Asbridge, S. J. Bame, G. Paschmann, and N. Sckopke. Observations of two distinct populations of bow shock ions in the upstream solar wind. GRL, 5:957–960, November 1978. doi: 10.1029/GL005i011p00957.

J. T. Gosling, M. F. Thomsen, S. J. Bame, W. C. Feldman, G. Paschmann, and N. Sckopke. Evidence for specularly reflected ions upstream from the quasiparallel bow shock. Geophysical Research Letters, 9(12):1333–1336, 1982. doi: 10.1029/GL009i012p01333.

K. Greisen. End to the Cosmic-Ray Spectrum? Physical Review Letters, 16:748–750, April 1966. doi: 10.1103/PhysRevLett.16.748.

F. Guo and J. Giacalone. The Acceleration of Electrons at Collisionless Shocks Moving Through a Turbulent Magnetic Field. ApJ, 802:97, April 2015. doi: 10.1088/0004-637X/802/2/97.

X. Guo, L. Sironi, and R. Narayan. Non-thermal Electron Acceleration in Low Mach Number Collisionless Shocks. II. Firehose-mediated Fermi Acceleration and its Dependence on Pre-shock Conditions. ApJ, 797:47, December 2014. doi: 10.1088/0004-637X/797/1/47.

DA Gurnett, WS Kurth, LF Burlaga, and NF Ness. In situ observations of interstellar plasma with voyager 1. Science, 341(6153):1489–1492, 2013.

T. Hada, M. Oonishi, B. LembèGe, and P. Savoini. Shock front nonstationarity of supercritical perpendicular shocks. Journal of Geophysical Research (Space Physics), 108:1233, June 2003. doi: 10.1029/2002JA009339.

W. F. Hanlon. The energy spectrum of ultra high energy cosmic rays measured by the High Resolution Fly's Eye observatory in stereoscopic mode. PhD thesis, The University of Utah, June 2008.

Yufei Hao, Xinliang Gao, Quanming Lu, Can Huang, Rongsheng Wang, and Shui Wang. Reformation of rippled quasi-parallel shocks: 2-d hybrid simulations. Journal of Geophysical Research: Space Physics, 2017.

Diego Harari. Ultra-high energy cosmic rays. Physics of the Dark Universe, 4:23 – 30, 2014. ISSN 2212-6864. doi: https://doi.org/10.1016/j.dark.2014.04.003. URL http://www.sciencedirect.com/science/article/pii/S2212686414000120. DARK TAUP2013.

P. Hellinger, P. Trávnícek, and H. Matsumoto. Reformation of perpendicular shocks: Hybrid simulations. GRL, 29:2234, December 2002. doi: 10.1029/2002GL015915.

H. Hietala, N. Agueda, K. AndréEová, R. Vainio, S. Nylund, E. K. J. Kilpua, and H. E. J. Koskinen. In situ observations of particle acceleration in shock-shock interaction. Journal of Geophysical Research (Space Physics), 116:A10105, October 2011. doi: 10.1029/2011JA016669.

A. M. Hillas. The Origin of Ultra-High-Energy Cosmic Rays. ARAA, 22:425–444, 1984. doi: 10.1146/annurev.aa.22.090184.002233.

G. C. Ho, D. Lario, R. B. Decker, M. I. Desai, Q. Hu, J. Kasper, and A.-F. Viñas. Multi-Spacecraft Observations of Interplanetary Shock Accelerated Particle Events. In B. Fleck, T. H. Zurbuchen, and H. Lacoste, editors, Solar Wind 11/SOHO 16, Connecting Sun and Heliosphere, volume 592 of ESA Special Publication, page 421, September 2005.

M Hoshino and N Shimada. Nonthermal electrons at high mach number shocks: Electron shock surfing acceleration. The Astrophysical Journal, 572(2):880, 2002.

M. Hoshino, J. Arons, Y. A. Gallant, and A. B. Langdon. Relativistic magnetosonic shock waves in synchrotron sources - Shock structure and nonthermal acceleration of positrons. ApJ, 390:454–479, May 1992. doi: 10.1086/171296.

Masahiro Hoshino. Nonthermal particle acceleration in shock front region:shock surfing accelerations. Progress of Theoretical Physics Supplement, 143:149–181, 2001.

Suoqing Ji, S Peng Oh, Mateusz Ruszkowski, and Maxim Markevitch. The efficiency of magnetic field amplification at shocks by turbulence. Monthly Notices of the Royal Astronomical Society, 463(4):3989–4003, 2016.

Tsunehiko N Kato. Particle acceleration and wave excitation in quasi-parallel high-mach-number collisionless shocks: Particle-in-cell simulation. The Astrophysical Journal, 802 (2):115, 2015.

Yusuke Kato. Interactions of hydromagnetic waves. Progress of Theoretical Physics, 21 (3):409–420, 1959.

Soshi Kawai. Divergence-free-preserving high-order schemes for magnetohydrodynamics: An artificial magnetic resistivity method. Journal of Computational Physics, 251:292–318, 2013.

C. F. Kennel, R. D. Blandford, and P. Coppi. MHD intermediate shock discontinuities. I - Rankine-Hugoniot conditions. Journal of Plasma Physics, 42:299–319, October 1989. doi: 10.1017/S0022377800014379.

Charles F. Kennel. Critical mach numbers in classical magnetohydrodynamics. Journal of Geophysical Research: Space Physics, 92(A12):13427–13437. doi: 10.1029/JA092iA12p13427.

Charles F Kennel. Critical mach numbers in classical magnetohydrodynamics. Journal of Geophysical Research: Space Physics, 92(A12):13427–13437, 1987.

S. Kobayashi, T. Piran, and R. Sari. Can Internal Shocks Produce the Variability in Gamma-Ray Bursts? ApJ, 490:92, November 1997. doi: 10.1086/512791.

X. Kong, G. Li, and Y. Chen. A Statistical Study of the Spectral Hardening of Continuum Emission in Solar Flares. apj, 774:140, 2013.

SM Krimigis, D Venkatesan, JC Barichello, and ET Sarris. Simultaneous measurements of energetic protons and electrons in the distant magnetosheath, magnetotail, and upstream in the solar wind. Geophysical Research Letters, 5(11):961–964, 1978.

G. F. Krymskii. A regular mechanism for the acceleration of charged particles on the front of a shock wave. Akademiia Nauk SSSR Doklady, 234:1306–1308, June 1977.

D. Lario, G. C. Ho, R. B. Decker, E. C. Roelof, M. I. Desai, and C. W. Smith. Ace observations of energetic particles associated with transient interplanetary shocks. AIP Conference Proceedings, 679(1):640–643, 2003. doi: 10.1063/1.1618676. URL https://aip.scitation.org/doi/abs/10.1063/1.1618676.

Martin A Lee, Vitali D Shapiro, and Roald Z Sagdeev. Pickup ion energization by shock surfing. Journal of Geophysical Research: Space Physics, 101(A3):4777–4789, 1996.

B. Lembège and J. M. Dawson. Plasma heating through a supercritical oblique collisionless shock. The Physics of Fluids, 30(4):1110–1114, 1987. doi: 10.1063/1.866309. URL https://aip.scitation.org/doi/abs/10.1063/1.866309.

B. Lembège and P. Savoini. Formation of reflected electron bursts by the nonstationarity and nonuniformity of a collisionless shock front. Journal of Geophysical Research (Space Physics), 107:1037, March 2002. doi: 10.1029/2001JA900128.

Bertrand Lembege and Philippe Savoini. Nonstationarity of a twodimensional quasiperpendicular supercritical collisionless shock by selfreformation. Physics of Fluids B: Plasma Physics, 4(11):3533–3548, 1992. doi: 10.1063/1.860361. URL https://doi.org/10.1063/1.860361.

MM Leroy and A Mangeney. A theory of energization of solar wind electrons by the earth's bow shock. In Annales Geophysicae, volume 2, pages 449–456, 1984.

G. Li, R. Moore, R. A. Mewaldt, L. Zhao, and A. W. Labrador. A Twin-CME Scenario for Ground Level Enhancement Events. SSR, 171:141–160, October 2012. doi: 10.1007/s11214-011-9823-7.

G. Li, X. Kong, G. Zank, and Y. Chen. On the spectral hardening at gsim300 kev in solar flares. apj, 769:22, 2013.

Xing Li and Shadia Rifai Habbal. Electron kinetic firehose instability. Journal of Geophysical Research: Space Physics, 105(A12):27377–27385, 2000.

EA Lucek, TS Horbury, MW Dunlop, PJ Cargill, SJ Schwartz, A Balogh, P Brown, C Carr, K-H Fornacon, and E Georgescu. Cluster magnetic field observations at a quasi-parallel bow shock. In Annales Geophysicae, volume 20, pages 1699–1710, 2002.

Jacob W Lynn, Eliot Quataert, Benjamin DG Chandran, and Ian J Parrish. The efficiency of second-order fermi acceleration by weakly compressible magnetohydrodynamic turbulence. The Astrophysical Journal, 777(2):128, 2013.

Y. E. Lyubarsky. The termination shock in a striped pulsar wind. MNRAS, 345:153–160, October 2003. doi: 10.1046/j.1365-8711.2003.06927.x.

G. Mann, A. Warmuth, and H. Aurass. Generation of highly energetic electrons at reconnection outflow shocks during solar flares. AAP, 494:669–675, February 2009. doi: 10.1051/0004-6361:200810099.

W Marshall. The structure of magneto-hydrodynamic shock waves. Proceedings of the Royal Society of London A: Mathematical, Physical and Engineering Sciences, 233 (1194):367–376, 1955. ISSN 0080-4630. doi: 10.1098/rspa.1955.0272. URL http://rspa.royalsocietypublishing.org/content/233/1194/367.

Adam Masters, Lukasz Stawarz, Masaki Fujimoto, STEVEN J Schwartz, Nick Sergis, MICHELLE F Thomsen, Alessandro Retino, Hiroshi Hasegawa, Bertalan Zieger, GETHYN R Lewis, et al. Electron acceleration to relativistic energies at a strong quasi-parallel shock wave. Nature Physics, 9(3):nphys2541, 2013.

S Matsukiyo and Y Matsumoto. Electron acceleration at a high beta and low mach number rippled shock. Journal of Physics: Conference Series, 642(1):012017, 2015. URL http://stacks.iop.org/1742-6596/642/i=1/a=012017.

S. Matsukiyo and M. Scholer. Modified two-stream instability in the foot of high Mach number quasi-perpendicular shocks. Journal of Geophysical Research (Space Physics), 108:1459, December 2003. doi: 10.1029/2003JA010080.

S. Matsukiyo and M. Scholer. On microinstabilities in the foot of high Mach number perpendicular shocks. Journal of Geophysical Research (Space Physics), 111:A06104, June 2006. doi: 10.1029/2005JA011409.

Shuichi Matsukiyo and Manfred Scholer. Simulations of pickup ion mediated quasi-perpendicular shocks: Implications for the heliospheric termination shock. Journal of Geophysical Research: Space Physics, 119(4):2388–2399, 2014.

Shuichi Matsukiyo, Yutaka Ohira, Ryo Yamazaki, and Takayuki Umeda. Relativistic electron shock drift acceleration in low mach number galaxy cluster shocks. The Astrophysical Journal, 742(1):47, 2011.

Y Matsumoto, T Amano, TN Kato, and M Hoshino. Stochastic electron acceleration during spontaneous turbulent reconnection in a strong shock wave. Science, 347(6225):974–978, 2015.

Yosuke Matsumoto, Takanobu Amano, and Masahiro Hoshino. Electron acceleration in a nonrelativistic shock with very high alfvén mach number. Physical review letters, 111 (21):215003, 2013.

Yosuke Matsumoto, Takanobu Amano, Tsunehiko N Kato, and Masahiro Hoshino. Electron surfing and drift accelerations in a weibel-dominated high-mach-number shock. Physical review letters, 119(10):105101, 2017.

C Mazelle, D Le Quéau, and K Meziane. Nonlinear wave-particle interaction upstream from the earth's bow shock. Nonlinear Processes in geophysics, 7(3/4):185–190, 2000.

C Mazelle, K Meziane, D LeQuéau, M Wilber, JP Eastwood, H Reme, JA Sauvaud, JM Bosqued, I Dandouras, M McCarthy, et al. Production of gyrating ions from nonlinear wave–particle interaction upstream from the earth's bow shock: A case study from cluster-cis. Planetary and Space Science, 51(12):785–795, 2003.

D. B. Melrose and M. H. Pope. Diffusive shock acceleration by multiple shocks. Proceedings of the Astronomical Society of Australia, 10:222, 1993.

K Meziane, AM Hamza, M Maksimovic, and TY Alrefay. The earth's bow shock velocity distribution function. Journal of Geophysical Research: Space Physics, 120(2):1229–1237, 2015.

Yosuke Mizuno, Martin Pohl, Jacek Niemiec, Bing Zhang, Ken-Ichi Nishikawa, and Philip E Hardee. Magnetic-field amplification by turbulence in a relativistic shock propagating through an inhomogeneous medium. The Astrophysical Journal, 726(2):62, 2010.

Yosuke Mizuno, Martin Pohl, Jacek Niemiec, Bing Zhang, Ken-Ichi Nishikawa, and Philip E Hardee. Magnetic field amplification and saturation in turbulence behind a relativistic shock. Monthly Notices of the Royal Astronomical Society, 439(4):3490–3503, 2014.

T Morita, Y Sakawa, Y Kuramitsu, S Dono, H Tanji, H Aoki, T Ide, K Nishio, CD Gregory, JN Waugh, et al. Interaction of high mach-number shocks in laser-produced plasmas. High Energy Density Physics, 9(1):187–191, 2013.

C. Mouhot and C. Villani. Landau damping. Journal of Mathematical Physics, 51(1): 015204, 2010. doi: 10.1063/1.3285283. URL https://doi.org/10.1063/1.3285283.

K. Nagata, M. Hoshino, C. H. Jaroschek, and H. Takabe. Interaction between Alternating Magnetic Fields and a Relativistic Collisionless Shock. ApJ, 680:627-638, June 2008. doi: 10.1086/587640.

T. Naito and F. Takahara. Monte carlo simulation of diffusive particle acceleration in shock waves with oblique magnetic fields. mnras, 275:1077–1092, 1995.

N. F. Ness, C. S. Scearce, and J. B. Seek. Initial Results of the Imp 1 Magnetic Field Experiment. JGR, 69:3531–3569, September 1964. doi: 10.1029/JZ069i017p03531.

M. Oka, T. Terasawa, Y. Seki, M. Fujimoto, Y. Kasaba, H. Kojima, I. Shinohara, H. Matsui, H. Matsumoto, Y. Saito, and T. Mukai. Whistler critical mach number and electron acceleration at the bow shock: Geotail observation. Geophysical Research Letters, 33 (24), 2006. doi: 10.1029/2006GL028156.

M Ostrowski and G Siemieniec-Ozibło. Diffusion in momentum space as a picture of second-order fermi acceleration. Astroparticle Physics, 6(3-4):271–277, 1997.

K. Papadopoulos. Electron heating in superhigh Mach number shocks. APSS, 144:535–547, May 1988. doi: 10.1007/BF00793203.

J. Park, C. Ren, J. C. Workman, and E. G. Blackman. Particle-in-cell Simulations of Particle Energization via Shock Drift Acceleration from Low Mach Number Quasi-perpendicular Shocks in Solar Flares. ApJ, 765:147, March 2013. doi: 10.1088/0004-637X/765/2/147.

G. Paschmann, N. Sckopke, I. Papamastorakis, J. R. Asbridge, S. J. Bame, and J. T. Gosling. Characteristics of reflected and diffuse ions upstream from the earth's bow shock. JGR, 86:4355–4364, June 1981. doi: 10.1029/JA086iA06p04355.

Kevin B. Quest. Simulations of high mach number perpendicular shocks with resistive electrons. Journal of Geophysical Research: Space Physics, 91(A8):8805–8815. doi: 10.1029/JA091iA08p08805.

Kevin B Quest. Simulations of high mach number perpendicular shocks with resistive electrons. Journal of Geophysical Research: Space Physics, 91(A8):8805–8815, 1986.

M. A. Riquelme and A. Spitkovsky. Electron Injection by Whistler Waves in Non-relativistic Shocks. ApJ, 733:63, May 2011. doi: 10.1088/0004-637X/733/1/63.

C. T. Russell, J. T. Gosling, R. D. Zwickl, and E. J. Smith. Multiple spacecraft observations of interplanetary shocks: Isee threedimensional plasma measurements. Journal of Geophysical Research: Space Physics, 88(A12):9941–9947, 1983. doi: 10.1029/JA088iA12p09941.

RZ Sagdeev. Cooperative phenomena and shock waves in collisionless plasmas. Rev plasma phys, 4:23, 1966.

E. T. Sarris, G. C. Anagnostopoulos, and S. M. Krimigis. Simultaneous measurements of energetic ion (50 kev) and electron (220 kev) activity upstream of earth's bow shock and inside the plasma sheet: Magnetospheric source for the november 3 and december 3, 1977 upstream events. Journal of Geophysical Research: Space Physics, 92(A11): 12083–12096, 1987. doi: 10.1029/JA092iA11p12083.

H. Schmitz, S. C. Chapman, and R. O. Dendy. Electron Preacceleration Mechanisms in the Foot Region of High Alfvénic Mach Number Shocks. ApJ, 579:327–336, November 2002. doi: 10.1086/341733.

M. Scholer and F. M. Ipavich. Energetic ions upstream of the earth's bow shock during an energetic storm particle event. JGR, 88:5715–5726, July 1983. doi: 10.1029/JA088iA07p05715.

M. Scholer and S. Matsukiyo. Nonstationarity of quasi-perpendicular shocks: a comparison of full particle simulations with different ion to electron mass ratio. Annales Geophysicae, 22:2345–2353, July 2004. doi: 10.5194/angeo-22-2345-2004.

Manfred Scholer. Diffuse ions at a quasiparallel collisionless shock: Simulations. Geophysical Research Letters, 17(11):1821–1824, 1990. doi: 10.1029/GL017i011p01821.

Manfred Scholer. Upstream waves, shocklets, short largeamplitude magnetic structures and the cyclic behavior of oblique quasiparallel collisionless shocks. Journal of Geophysical Research: Space Physics, 98(A1):47–57, 1993. doi: 10.1029/92JA01875.

Manfred Scholer, Harald Kucharek, and Iku Shinohara. Short large-amplitude magnetic structures and whistler wave precursors in a full-particle quasi-parallel shock simulation. Journal of Geophysical Research: Space Physics, 108(A7), 2003.

N. Shimada and M. Hoshino. Strong Electron Acceleration at High Mach Number Shock Waves: Simulation Study of Electron Dynamics. ApJL, 543:L67–L71, November 2000. doi: 10.1086/318161.

N. Shimada, T. Terasawa, M. Hoshino, T. Naito, H. Matsui, T. Koi, and K. Maezawa. Diffusive shock acceleration of electrons at an interplanetary shock observed on 21 feb 1994. In Jörg Büchner, Ian Axford, Eckart Marsch, and Vytenis Vasyliūnas, editors, Plasma Astrophysics And Space Physics, pages 481–488, Dordrecht, 1999. Springer Netherlands. ISBN 978-94-011-4203-8.

L. Sironi and A. Spitkovsky. Acceleration of Particles at the Termination Shock of a Relativistic Striped Wind. ApJ, 741:39, November 2011. doi: 10.1088/0004-637X/741/1/39.

J. Skilling. Cosmic ray streaming. i - effect of alfven waves on particles. mnras, 172: 557–566, 1975.

C. P. Sonett and I. J. Abrams. The Distant Geomagnetic Field, 3, Disorder and Shocks in the Magnetopause. JGR, 68:1233–1263, March 1963. doi: 10.1029/JZ068i005p01233.

BU Ö Sonnerup. Acceleration of particles reflected at a shock front. Journal of Geophysical Research, 74(5):1301–1304, 1969.

T. Sugiyama and T. Terasawa. A scatter-free ion acceleration process in the parallel shock. Advances in Space Research, 24:73–76, January 1999. doi: 10.1016/S0273-1177(99)00427-5.

Tooru Sugiyama, M Fujimoto, and T Mukai. Quick ion injection and acceleration at quasi-parallel shocks. Journal of Geophysical Research: Space Physics, 106(A10):21657–21673, 2001.

K. Takahashi, S. Yamada, and Yamada. Regular and non-regular solutions of the Riemann problem in ideal magnetohydrodynamics. Journal of Plasma Physics, 79:335–356, June 2013. doi: 10.1017/S0022377812001006.

K. Takahashi, S. Yamada, and Yamada. Exact Riemann solver for ideal magnetohydrodynamics that can handle all types of intermediate shocks and switch-on/off waves. Journal of Plasma Physics, 80:255–287, April 2014. doi: 10.1017/S0022377813001268.

Derek A Tidman and Nicholas A Krall. Shock waves in collisionless plasmas. American Journal of Physics, 40(7):1055–1055, 1972.

R. A. Treumann. Fundamentals of collisionless shocks for astrophysical application, 1. Non-relativistic shocks. AAPR, 17:409–535, December 2009. doi: 10.1007/s00159-009-0024-2.

R. A. Treumann and C. H. Jaroschek. Planetary Bow Shocks. ArXiv e-prints, August 2008.

K. Tsubouchi and B. Lembège. Full particle simulations of short largeamplitude magnetic structures (slams) in quasiparallel shocks. Journal of Geophysical Research: Space Physics, 109(A2), 2004. doi: 10.1029/2003JA010014.

Yasunobu Uchiyama, Felix A Aharonian, Takaaki Tanaka, Tadayuki Takahashi, and Yoshitomo Maeda. Extremely fast acceleration of cosmic rays in a supernova remnant. Nature, 449(7162):576, 2007.

A. A. Vlasov. On the kinetic theory of an assembly for particles with collective interaction. J. Phys. (USSR), 9:25–40, 1945.

H. Washimi, G. P. Zank, Q. Hu, T. Tanaka, K. Munakata, and H. Shinagawa. Realistic and time-varying outer heliospheric modelling. MNRAS, 416:1475–1485, September 2011. doi: 10.1111/j.1365-2966.2011.19144.x.

D. Winske. Hybrid simulation codes with application to shocks and upstream waves. SSR, 42:53–66, October 1985. doi: 10.1007/BF00218223.

D Winske and KB Quest. Magnetic field and density fluctuations at perpendicular supercritical collisionless shocks. Journal of Geophysical Research: Space Physics, 93(A9): 9681–9693, 1988.

C. S. Wu, D. Winske, Y. M. Zhou, S. T. Tsai, P. Rodriguez, M. Tanaka, K. Papadopoulos, K. Akimoto, C. S. Lin, M. M. Leroy, and C. C. Goodrich. Microinstabilities associated with a high Mach number, perpendicular bow shock. SSR, 37:63–109, January 1984. doi: 10.1007/BF00213958.

CS Wu. A fast fermi process: Energetic electrons accelerated by a nearly perpendicular bow shock. Journal of Geophysical Research: Space Physics, 89(A10):8857–8862, 1984.

G. P. Zank, Y. Zhou, W. H. Matthaeus, and W. K. M. Rice. The interaction of turbulence with shock waves: A basic model. Physics of Fluids, 14:3766–3774, November 2002. doi: 10.1063/1.1507772.

GP Zank, P Hunana, P Mostafavi, JA Le Roux, Gang Li, GM Webb, O Khabarova, A Cummings, E Stone, and R Decker. Diffusive shock acceleration and reconnection acceleration processes. The Astrophysical Journal, 814(2):137, 2015.

L. Zhao and G. Li. Particle acceleration at a pair of parallel shocks near the sun. Journal of Geophysical Research (Space Physics), 119:6106–6119, 2014.

VITA

- Name: Masaru Nakanotani
- Birthdate: 11 September 1989
- Birthplace: Fukui, Japan
- Parents: Hirhoshi Nakanotani and Terumi Nakanotani
- Education:
  - Takefu High School, Takefu city, Fukui, Japan, 2005-2008
  - Bachelor of Energy from Department of Energy Science and Engineering, Faculty of Engineering of Kyushu University, 2008-2012
  - Master of Science from Department of Earth System Science and Technology, Interdisciplinary Graduate School of Engineering Sciences of Kyushu University, 2012-2014
  - Promotionsstipendium: L'Institut de Recherche en Astrophysique et Planétologie (IRAP), Toulouse, France, 2015-2016
  - Philosophy of Doctor from Department of Earth System Science and Technology, Interdisciplinary Graduate School of Engineering Sciences of Kyushu University, 2014-